FLUID MODELING AND DESIGN OF GAS CHANNELS OF SOLAR NON-STOICHIOMETRIC REDOX REACTOR

A THESIS
SUBMITTED TO THE FACULTY OF
UNIVERSITY OF MINNESOTA
BY

ADITYA KEDLAYA

IN PARTIAL FULFILLMENT OF THE REQUIREMENTS
FOR THE DEGREE OF
MASTER OF SCIENCE IN MECHANICAL ENGINEERING

JANE H. DAVIDSON, ADVISOR

FEBRUARY 2015

© Aditya Kedlaya 2015

Acknowledgements

There are many people without whom I could not have completed this work. I list some of them here and I am ever grateful to them.

First of all, I would like to thank my advisor Jane Davidson for providing an opportunity to work in the field of solar energy research. I would keep in mind her advice on being organized and carrying out efficient communication. I admire her leadership skills and appreciate her constant support for students.

I would like to thank professors Wojciech Lipiński and Thomas Chase, who were part of this project, for their invaluable suggestions.

I would like to thank Roman Bader, post-doctoral associate, for his constant guidance and several suggestions on how to approach any problem.

I would like to thank all of my lab mates especially Justin Lapp, Dan Keene, Peter Krenzke, Rohini Bala Chandran, Stephen Sedler and Luke Venstrom who provided helpful suggestions throughout the course of the project.

I would like to thank my roommates Anand and Raghu. Without them, I would not have completed my masters. I would also like to thank all other friends - Pavani, Palak, Divyanshu, Vishal, Sreekanth, Rahul, Haritha, Sneha, Nishitha, Bala, Thaseem for making my stay here a wonderful experience. I would also like to thank my multi-faceted IITG gang of friends' dags.

Lastly, I would like to thank my parents for their unwavering belief in me.

Funding for the project was provided by the National Science Foundation.

Abstract

The present numerical study in FLUENT analyzes the fluid flow field within a solar powered reactor designed for syngas production. The thermochemical reactor is based on continuous cycling of cerium oxide (ceria) in a non-stoichiometric reduction/oxidation cycle. The reactor uses a hollow cylinder of porous ceria which rotates through a high-temperature zone, by exposure to concentrated sunlight and partially reduced in an inert atmosphere due to flow of the sweep gas (N_2), and then through a lower temperature zone where the reduced ceria is re-oxidized with a flow of CO_2 and/or H_2O, to produce CO and/or H_2. In terms of fluid flow modeling, the issue of crossover of species (leakage) within the reactor is critical for proper functioning of the reactor.

The first part of the work relates to the geometry and placement of the inlet/outlet gas channels for the reactor optimized to minimize crossover of the species. This is done by conducting a parametric study of geometric variables associated with the inlet/outlet geometry. A simplified 2D fluid flow reactor model which incorporates multi-species flow is used for this study. Further, 2D and 3D reactor models which capture the internal structure more accurately are used to refine the inlet/outlet design. The optimized reactor model is found to have an O_2 crossover of 2%-6% and oxidizer crossover of 8%-21% at different flow rates of the sweep gas and the oxidizer studied.

In the second part of the work, the reactor model is simulated under varying test conditions. Different working conditions include morphologies of the reactive material, rotational speed of the ceria ring and the recuperator, flow rates of sweep gas and the oxidizer, types of oxidizer (CO_2, H_2O). The 3D reactor model is also tested using one, two and three discrete inlet/outlet ports and compared with slot configuration.

Table of Contents

List of tables

List of figures

Nomenclature

A	area (m^2)
Br	Brinkman number
$\boldsymbol{C}$	crossover value (kg s^{-1}/kg s^{-1})
CL	curve length (m)
$\mathcal{D}_{i,j}$	binary diffusion coefficient (m^2 s^{-1})
D	diameter of the cavity (m)
$D_{i,j}$	diffusion coefficient (m^2 s^{-1})
d	diameter (m)
E	energy per volume (J m^{-3})
F_{DF}	Dupuit-Forchheimer co-efficient (m^{-1})
f	ratio of molar rate of N_2 to O_2
$\overline{HHV}$	high heating value (J mol^{-1})
g	gravity (m s^{-2})
H	height (m)
h	specific enthalpy (J kg^{-1})
$\overline{\mathbf{J}}$	diffusive flux (mol m^{-2} s^{-1})
K	permeability (m^2)
k	thermal conductivity (W m^{-1} K^{-1})
k_B	boltzmann constant; $1.38x10^{-23}$ J K^{-1}
L	length of the cavity (m)
M	molecular weight (kg mol^{-1})
m''	mass flux (kg m^{-2})
$\dot{m}$	mass flow rate (kg s^{-1})
n	moles (mol)
$\dot{n}$	molar throughput (mol s^{-1})
$\dot{Q}$	incident concentrated solar radiation (W)
PP	partial pressure (atm)
$\overline{\mathrm{PP}}$	average partial pressure (atm)
p	pressure (Pa)
R	radius (m)
S	source term (kg m^{-3} s^{-1})
SP	static pressure (Pa)
T	temperature (K)
U	speed (m s^{-1})

u	velocity component in x-direction (m s^{-1})
v	velocity component in y-direction (m s^{-1})
w	velocity component in z-direction (m s^{-1})
$\bar{\mathbf{v}}$	velocity vector (m s^{-1})
w	width of channels (mm)
X	mole fraction (mol/mol)
Y	mass fraction (kg/kg)
y	position in y direction (m)

Greek symbols

α	circumferential position of channels (deg)
δ	non-stoichiometric state of the ceria
ε	microscopic energy (J)
γ	porosity
η	efficiency
Ω	angular speed (rad s^{-1})
$\overline{\Omega}$	collision integral
ϕ	angular position (deg)
ϕ	zone width (deg)
ρ	density (kg m^{-3})
σ	collision diameter (A)
$\underline{\underline{\tau}}$	stress tensor (Pa)
θ	angular positions of channels (deg)
μ	dynamic viscosity (Pa s)

Subscripts

1-4	reactor inlets/outlets
A	cross-sectional area
atmosphere	atmospheric pressure
CeO_2	related to ceria
c	intermediate value
CO_2	carbon dioxide
CO	carbon monoxide
H	height averaged
H_2O	steam
i	initial

i, j	species indices
in	inner surface
inlet	inlet
f	final, fluid mixture
N	total number of species
N_2	nitrogen
O_2	oxygen
out	outer surface
outlet	outlet
p	porous
r	recuperator
red	related to reduction step or zone
oxd	related to oxidation step or zone
x, y	stoichiometric coefficients
fuel	fuel

Superscripts

'	rotating reference frame

1.0 Introduction

1.1 Motivation

Solar energy is an attractive alternative to fossil fuels. Thermo-chemical methods, using solar energy, can be used to produce fuels like hydrogen and syngas [1] [2]. In specific, concentrated solar radiation can be used as the heat source in the thermochemical method to drive the metal oxide to split water and CO_2 using two-step reduction-oxidation cycles [3, 4, 8].

The two-step metal oxide based reduction-oxidation cycle has an endothermic step followed by an exothermic step. These reactions are shown for water splitting.

Solar, endothermic step:

$$\frac{1}{\Delta\delta} M_x O_{y-\delta_{ox}} \rightarrow \frac{1}{\Delta\delta} M_x O_{y-\delta_{red}} + 0.5 O_2 \tag{1.1}$$

Non-solar, exothermic step:

$$\frac{1}{\Delta\delta} M_x O_{y-\delta_{red}} + H_2O \rightarrow \frac{1}{\Delta\delta} M_x O_{y-\delta_{oxd}} + H_2 \tag{1.2}$$

$$\frac{1}{\Delta\delta} M_x O_{y-\delta_{red}} + CO_2 \rightarrow \frac{1}{\Delta\delta} M_x O_{y-\delta_{oxd}} + CO \tag{1.3}$$

Net reaction:

$$H_2O \rightarrow H_2 + 0.5O_2$$
$$CO_2 \rightarrow CO + 0.5O_2 \tag{1.4}$$

In these reactions, δ_{red} and δ_{oxd} are the non-stoichiometry values after reduction and oxidation, and $\Delta\delta = \delta_{red} - \delta_{ox}$. The reduction reaction is highly endothermic, which in this case, is solar driven. The oxidation reaction is exothermic and is favored at lower temperature than the reduction reaction.

The reactive material (the metal-oxide) is not consumed and returns to its original state at the end of the cycle and the products (H_2/CO and O_2) are produced in separate stages, thus, avoiding recombination. In the current study, ceria is used as the reactive material since it has high melting point (2800 K) and maintains its solid state for non-stoichiometry as low as δ = 0.25 [11].

The reactor shown in the figure 1.1 is being built at University of Minnesota, based on the two-step process using ceria (CeO_2) as the reactive material [12, 13].

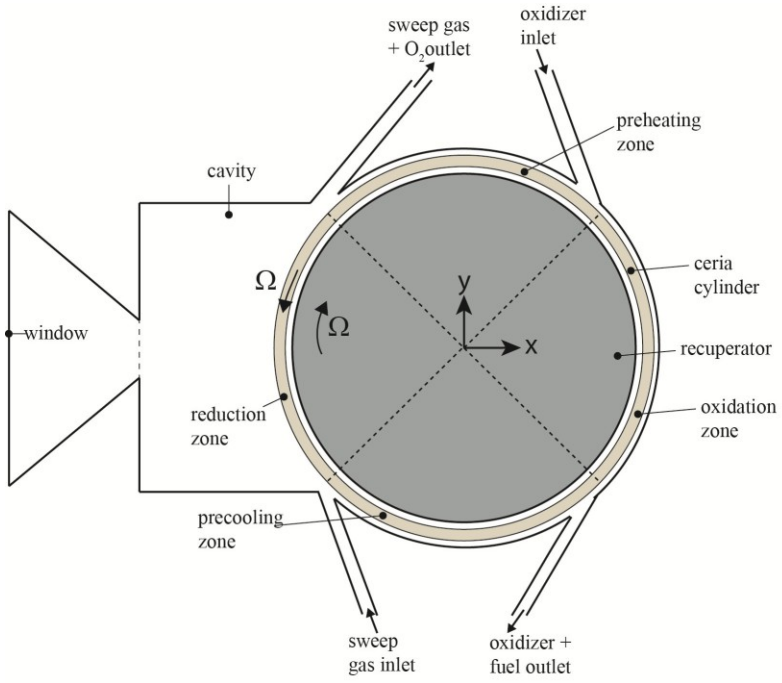

Figure 1.1 – Schematic of the proposed reactor

Working of the reactor is based on the alternate cycling of the porous ceria between two different temperatures and different gas atmospheres. The chemical composition of the ceria undergoes changes (eqn 1.1 & 1.2) during the thermal cycling and is coupled with the decomposition of the oxidizer to produce the fuel which is of interest to us. H_2/CO is released depending on the oxidizer type H_2O/CO_2.

The reactor consists of two concentric cylinders rotating in opposite directions as shown in figure 1.1. The outer cylinder is porous ceria. The inner cylinder is an inert ceramic material like alumina. The concentrated sunlight falls on one side of the reactor causing the ceria to reach highest temperature within the reactor where the ceria is reduced. The inert gas (N_2) sweeps away

the oxygen produced in this zone so as to maintain relatively low O_2 partial pressure necessary for reduction. On the other side, high concentration of oxidizer H_2O or CO_2 oxidizes the ceria to produce fuel. The concentric counter-rotating inert inner cylinder acts as a recuperator used to partially recycle the energy associated with the cyclic heating/cooling of the reactive material via radiative heat exchange. In the oxidation zone, the ceria cylinder is actively cooled (not shown) to a lower cycle temperature. The non-stoichiometry is a function of local temperature of ceria and the local O_2 partial pressure. The amount of O_2 and the fuel released is directly proportional to the change in non-stoichiometry $\Delta\delta = \delta_{red} - \delta_{ox}$.

To date, the highest solar-to-fuel conversion efficiencies reached with thermochemical water/CO_2 splitting is 1.7 % (averaged over one cycle) [14]. Parametric thermodynamic analysis of the reaction cycle carried out by Lapp [15] suggested that increased effectiveness of solid phase heat recovery combined with gas phase heat recovery could lead to thermal efficiency of more than 10%. Lapp [16] carried out a parametric study of geometric and material properties for the solar two-step redox reactor. The parametric study demonstrated that solid phase heat recovery of over 50% is possible and thus, overall thermal efficiency of 10% is not unreasonable.

This approach does not take into account the flow of the individual species. This gap in the analysis warrants a separate study involving the fluid flow within the reactor. The current study aims to shed some light into

crossover, flow through porous media, buoyancy effects as much as possible within its framework. This study is carried out in a reactor model using FLUENT based on the prototype reactor design [17, 18].

1.2 Crossover

In an ideal scenario, the inert N_2 gas should sweep over the entire reduction zone and carry away the entire O_2 released in that zone through the N_2/O_2 outlet. The reduced ceria maintains its non-zero non-stoichiometry (δ_{red}) in the pre-cooling zone until it is oxidized in the oxidation zone. The oxidizer CO_2 sweeps through the oxidization zone where some of it gets reduced and the CO_2/CO mixture leaves the reactor system through the CO outlet. Ideally, there would be no mixing of the gases on the two sides and they leave through their respective outlets. In this case, the amount of fuel produced can be calculated based on the amount of the O_2 released or equivalently by the change in non-stoichiometry from reduction zone to oxidation zone. The relation between rate of fuel production, rate of O_2 produced and change in non-stoichiometry is given in eqn 1.5.

$$\dot{n}_{O_2} = \frac{(\delta_{red} - \delta_{oxd})}{2} \cdot \dot{n}_{CeO_2} = \frac{\dot{n}_{fuel}}{2} \quad \text{(mol/s)} \tag{1.5}$$

The efficiency of the reactor system is defined as follows [15].

$$\eta = \frac{\dot{n}_{fuel} \cdot HHV_{fuel}}{\dot{Q}_{solar}} \tag{1.6}$$

The efficiency is defined based on the energy output of the fuel produced with respect to the concentrated solar energy input.

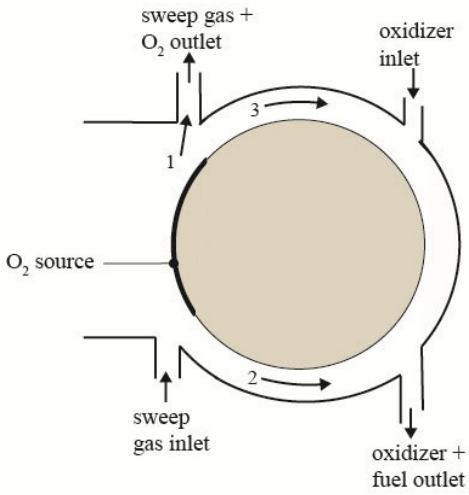

Figure 1.2: Crossover paths for O_2 in a 2D simplified reactor model

In reality, the species can flow throughout the reactor. Crossover is explained for a single species O_2 using a simplified diagram of the reactor shown in figure 1.2. The O_2 released from the reduction zone can exit the reactor in these three possible ways. The fraction of O_2 which takes the paths 2 or 3 and exits through the CO_2 outlet is termed as the crossover fraction of O_2. The paths 2, 3 are termed crossover paths for O_2. The leakage is quantified by the crossover fraction, defined in terms of mass flow rates of O_2 in eqn. 1.7.

$$\boldsymbol{C}_{O2} = \frac{\dot{m}_{O2}\big|_{CO_2\ outlet}}{\dot{m}_{O2}\big|_{O_2\ source}} \tag{1.7}$$

Crossover can be defined for all the species involved and a similar expression can be written for crossover fraction of other species.

O_2 flowing through the pre-cooling zone (path 2) can recombine (oxidize) with the reduced ceria either partially or completely, as shown (unbalanced).

$$CeO_{2-\delta_{red}} + O_2 \rightarrow CeO_{2-\delta_c} \qquad where,\ \delta_{oxd} \leq \delta_c < \delta_{red} \tag{1.8}$$

This oxidation reaction results in change in non-stoichiometry of ceria to an intermediate value of $\delta_c (< \delta_{red})$ instead of remaining constant at δ_{red} in the pre-cooling zone. The change in state of ceria represents missed opportunity for the oxidizer to produce fuel. Conservatively, the loss in fuel production due to O_2 crossover is given in eqn. 1.9.

$$\Delta\dot{n}_{loss} = (\delta_{red} - \delta_c) \cdot \dot{n}_{ceria} \tag{1.9}$$

Similarly, O_2 crossing over from pre-heating zone (path 3) can compete with CO_2 in the oxidation zone to participate in the oxidation reaction, resulting in similar loss of fuel output. The loss in fuel output directly results in reduced efficiency of the reactor. Thus, the main aim of this study is to observe the effect of crossover and its dependence on the geometry and the mass flow rates of incoming gas streams. The incorporation of the porous ceria ring and the

recuperator into the reactor model leads to more number of crossover paths, as shown in figure 1.3.

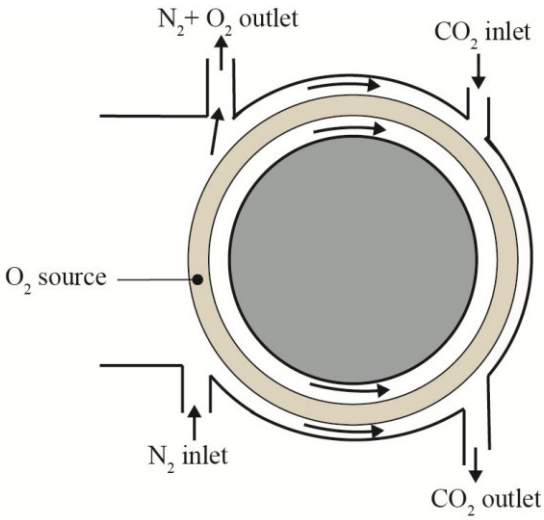

Figure 1.3: Crossover paths for O_2 in a 2D reactor model with ceria ring

The crossover adversely affects the overall efficiency of the reactor system and is quantified below. Assume that n_{cross} moles of O_2 cross over. Assuming all the crossed over O_2 is consumed in the oxidation reaction before CO_2 is reduced, the following reaction takes place. For the analysis, assume that oxidation goes to completion, i.e., $\delta_{oxd} = 0$.

$$CeO_{2-\delta_{red}} + n_{cross}O_2 \rightarrow CeO_{2-\delta_{red}+2n_{cross}} \tag{1.10}$$

$$CeO_{2-\delta_{red}+2n_{cross}} + (\delta_{red})CO_2 \rightarrow CeO_2 + 2\cdot n_{cross}CO_2 + (\delta_{red} - 2\cdot n_{cross})CO \tag{1.11}$$

Suppose, n_{fuel} moles of fuel is produced without crossover. Then with crossover, (n_{fuel} - $2.n_{cross}$) moles of fuel is produced (eqn. 1.11).

The crossover ratio $\boldsymbol{C}$ of O_2 defined in eqn 1.7 can be re-written in terms of molar flow rate as follows,

$$\boldsymbol{C}_{O2} = \frac{\dot{n}_{cross}}{\dot{n}_{O_2}} \tag{1.12}$$

The relation between amount of O_2 released in a single cycle to the amount of fuel is given in eqn 1.5, $\dot{n}_{O_2} = \frac{\dot{n}_{fuel}}{2}$. Combining the above expression, the net reduction in fuel output is given below.

$$\frac{\dot{n}'_{fuel}}{\dot{n}_{fuel}} = (1 - \boldsymbol{C}_{O2}) \tag{1.13}$$

Similar expression for the reduction in fuel can be written in terms of the crossover of fuel. Thus, the efficiency of the reactor with crossover can be written as follows,

$$\eta'_{reactor} = \eta_{reactor} \cdot (1 - \boldsymbol{C}_{O2}) \cdot (1 - \boldsymbol{C}_{CO}) \tag{1.14}$$

These simplified expressions take into account the reduction in fuel output due to O_2 and CO crossovers only. The crossovers of N_2 and CO_2 can also alter the fuel output by changing chemistry of the ceria. However, they are not discussed in this study.

1.3 Fuel output

The non-stoichiometry of the ceria material, dependent on the temperature and O_2 partial pressure, is obtained at thermodynamic equilibrium from Panlener *et. al.*[19].

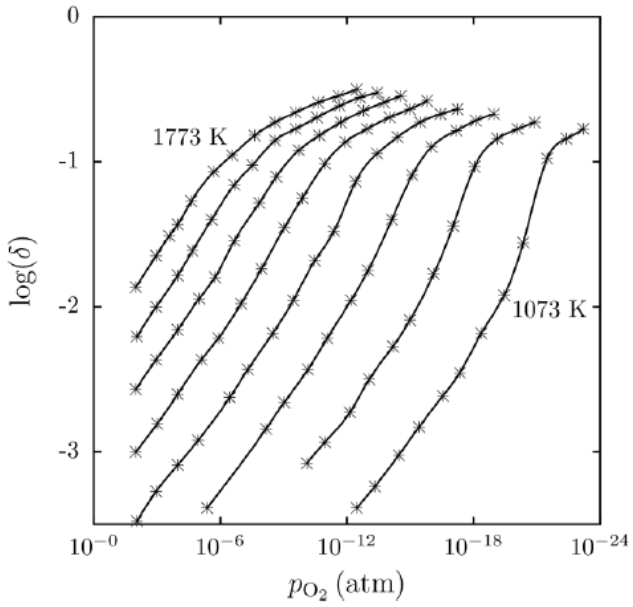

Figure 1.4: Non-stoichiometry of ceria as a function of temperature and O_2 partial pressure [19]

In Lapp's work [15], a single non-stoichiometric value for the ceria is assumed in the reduction zone based on the reduction temperature and O_2 partial pressure. In the current model, there is a temperature and O_2 partial pressure field within the reduction zone. Thus, 'non-stoichiometry field' exists at every location based on the local temperature and O_2 partial pressure. However, whether the rotating ceria attains the local non-stoichiometry depends on the kinetics of the reduction reaction. Since in this study, chemical modeling is not involved and the temperature profile of ceria ring is fixed, we will look into the O_2 partial pressure in the reduction region to estimate the fuel output. If fast kinetics is assumed, the O_2 partial pressure at the exit of the reduction zone is a relatively good measure of the upper limit of the fuel produced in that cycle.

However, since reduction reactions take finite time, average O_2 partial pressure within the reduction zone is considered.

1.4 Objectives

The design part of the study involves the study of impact of the inlet/outlet geometry on the crossover of each species. Based on this study, the model with minimum crossover is chosen. Using this model, the properties of the ceria ring like permeability is varied and the flow field is observed. The effect of the rotation of the ceria ring on the flow field and species concentration is studied. The effect of the changes in mass flow rates of sweeping gas and the oxidizer on the flow field is studied. Differences in flow field due to the effect of different oxidizers like CO_2, H_2O are also noted. The effects of changing inlet/outlet configurations on the fluid flow field within the reactor and dependence on crossover are studied.

1.5 Outline of the thesis

Chapter 2 provides the results of the parametric study of the inlet and outlet widths, angular and circumferential positions. Chapter 3 provides the results of the flow field due to variations in physical properties of the porous ceria ring. Chapter 4 deals with the effects of the rotation of the ceria ring. Chapter 5 provides the results of changes in mass flow rates of sweep gas and the oxidizer on the flow field within the reactor. Chapter 6 deals with the results of different inlet/outlet configurations on the flow field. At the end, summary and the future outlook are presented.

2.0 Parametric study of the inlet/outlet geometry

2.1 Introduction

This chapter deals with the design of the gas channels so as to minimize the species' crossover. A parametric study is done with respect to the angular positions of the inlets/outlets (θ), width of the inlets/outlets (w), and circumferential position of the channels (α), shown in figure 2.1. Based on this study, the most suitable gas channels design is chosen for the prototype reactor.

2.2 Modeling approach

Different reactor models are used in this study. The crossover of the species depends on the geometric parameters of the inlet/outlet geometry if the inlet and outlet flow conditions are fixed. Hence, majority of the parametric runs are carried out using a simplified 2D fluid flow model of the reactor. Figure 2.1 shows the 2D simplified model of the reactor with crossover paths indicated. N_2, CO_2 enter through the sweep gas and oxidizer inlets and exit through sweep gas and oxidizer outlets, respectively. The O_2 and CO source terms are modeled along the circumference of the solid cylinder in the reduction and oxidation zones, respectively as mass inlets (kg/s). The porous ceria and the recuperator are modeled as impermeable cylinder. The low permeability value (K = 3.8×10^{-12} m^2 [20]) of the porous ceria is assumed to lead to low flow rates of the species through the ceria ring (see chapter 3). The rotation of the porous cylinder is also neglected (see chapter 4).

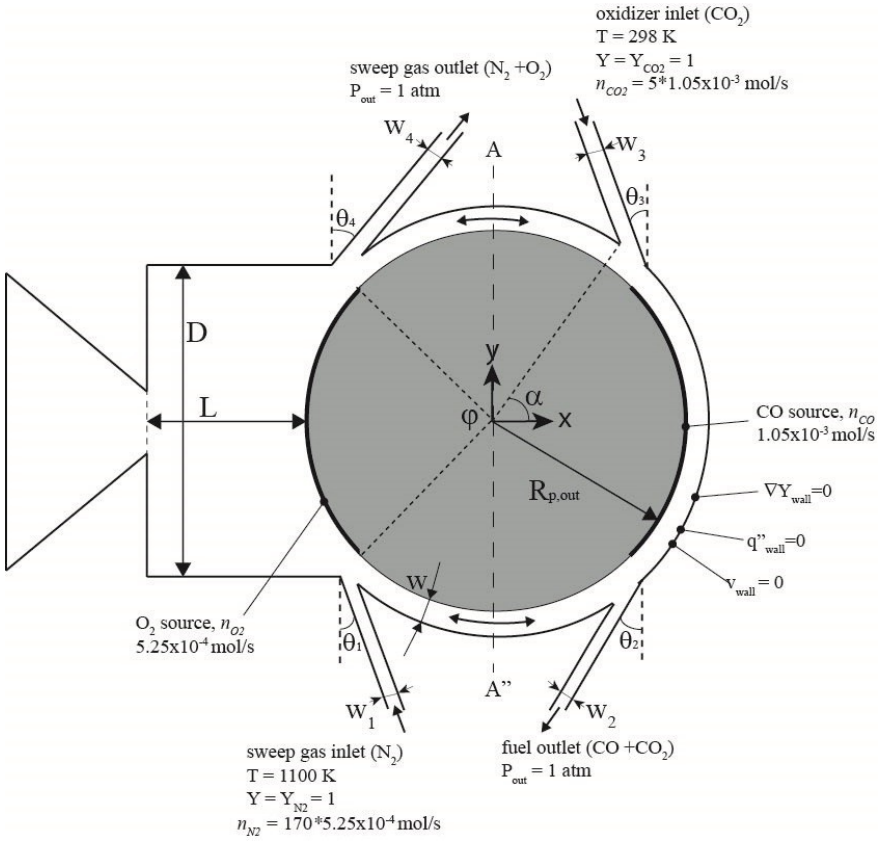

Figure 2.1: 2D simplified reactor model

The prototype reactor design was carried out using the target maximum average ceria temperature of 1850 K and O_2 partial pressure of 10^{-2} atm in the reduction region [18]. The non-stoichiometry calculated using these values is $\delta_{red} = 0.025$. Using the total moles of ceria (12.6 moles) and the rotation speed (0.2 rpm), the fuel output has been calculated using equation 1.5, assuming complete oxidation ($\delta_{oxd} = 0$).

$$\dot{n}_{fuel} = \left(\delta_{red} - \delta_{oxd}\right) \cdot \dot{n}_{ceria} = 2\dot{n}_{O_2}$$

$$\dot{n}_{fuel} = 1.05 \times 10^{-3} \text{ mol/s}$$

$$\dot{n}_{O_2} = 5.25 \times 10^{-4} \text{ mol/s}$$

The O_2 and fuel release is distributed uniformly along the reduction and oxidation zones. These values of the O_2 release and the fuel is fixed for all the simulations in this study. This 2D reactor model is utilized for most of the parametric runs. The 2D reactor model with porous ceria ring and 3D reactor model, described below are used in the final run of the parametric study.

Generally, extra amount of oxidizer is passed through the reactor to promote greater reaction extent of the oxidation reaction. A 5:1 (5x) ratio of oxidizer to fuel is assumed in the current study. Hence, the flow rate of CO_2 is set to $5 \times 1.05 \times 10^{-3}$ mol/s or 2.31×10^{-5} kg/s. Preliminary analysis using a 2D simplified geometry indicates a 170:1 (170x) ratio of sweep gas (N_2) to oxygen release is required to maintain a mean PP_{O2} of 10^{-2} atm in the reduction zone. Thus, mass flow rates of N_2 is fixed at $170 \times 5.25 \times 10^{-4}$ mol/s or 2.5×10^{-3} kg/s for the set of parametric study.

2D reactor model with porous ceria ring is shown in figure 2.2. This model incorporates the inner gap between the ceria ring and the recuperator. The porous ceria ring acts as additional crossover path. The porous ceria ring is divided into 4 separate zones - reduction, oxidation, pre-cooling, pre-heating zones, each of 90°. The reduction and oxidation zones are symmetric about the X-axis. Similarly, pre-cooling and pre-heating zones are symmetric about the Y-axis. The O_2 and the fuel (H_2/CO) release in equations 1.5 are modeled as uniform volumetric sources (kg/m^3-s) (with unit depth) in the reduction and oxidation zones, respectively.

The dimensions of the reactor is given in table 2.1. These dimensions were determined in a separate heat transfer study carried out by Lapp [18].

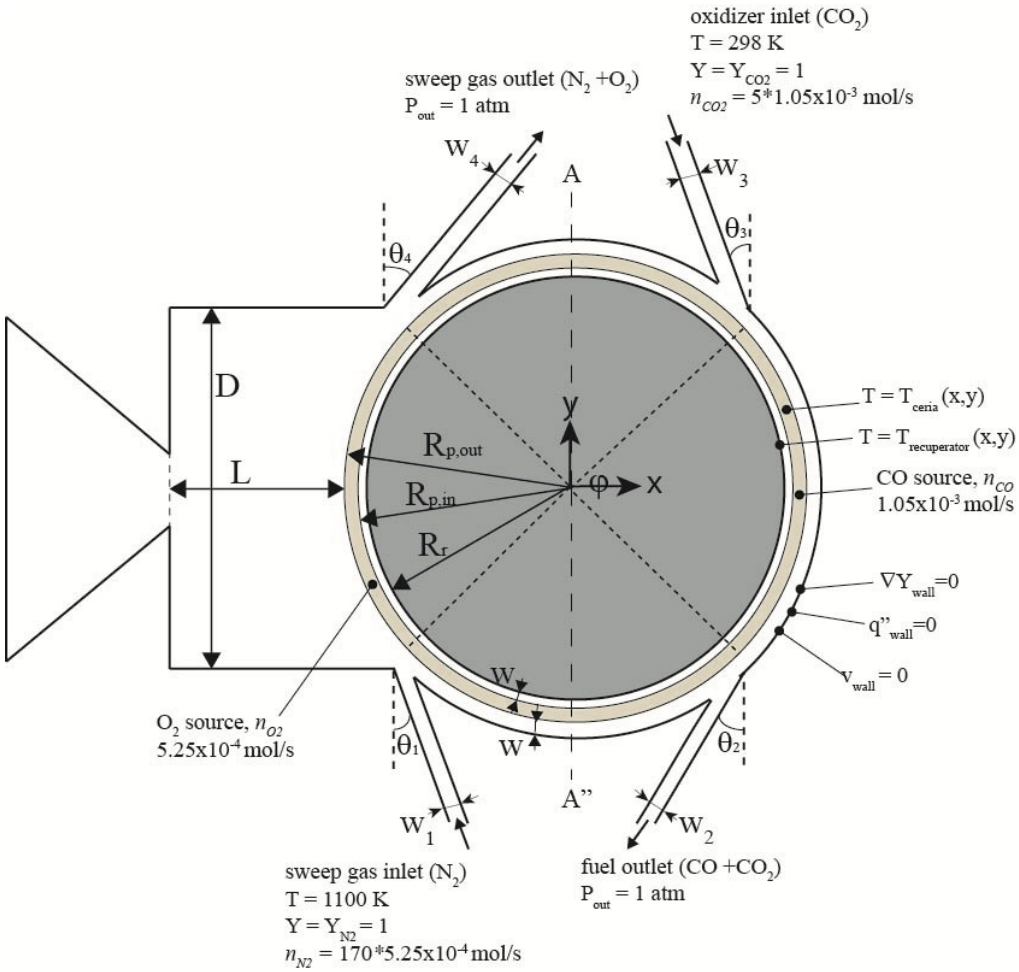

Figure 2.2: 2D reactor model with ceria ring

A 3D fluid flow model which includes more crossover paths is developed for final test run. The top view of the reactor model is same as in the figure 2.2. The side view of the reactor is shown in the figure 2.3. This model includes paths at the top and the bottom of the reactor. All the crossover paths are extended in the z-direction as shown. The O_2 and CO sources are modeled as volumetric sources (kg/m^3-s).

Geometric dimensions	Value
Length of the cavity (L)	100 mm
Diameter of the cavity (D)	200 mm
Crossover gap (w)	5 mm
Radius of the outer surface of ceria ring ($R_{p,out}$)	135 mm
Radius of the inner surface of ceria ring ($R_{p,in}$)	127 mm
Inner gap between ceria and recuperator (w)	5 mm
Radius of the recuperator (R_r)	122 mm
Height of the reactor (h)	200 mm
Zone width (φ)	π/2 radians

Table 2.1: Dimensions of the reactor system

The material properties of the porous ceria have been obtained from the modeling work done by Haussner *et al* [20]. The properties of ceria used in the modeling is given in the table 2.2.

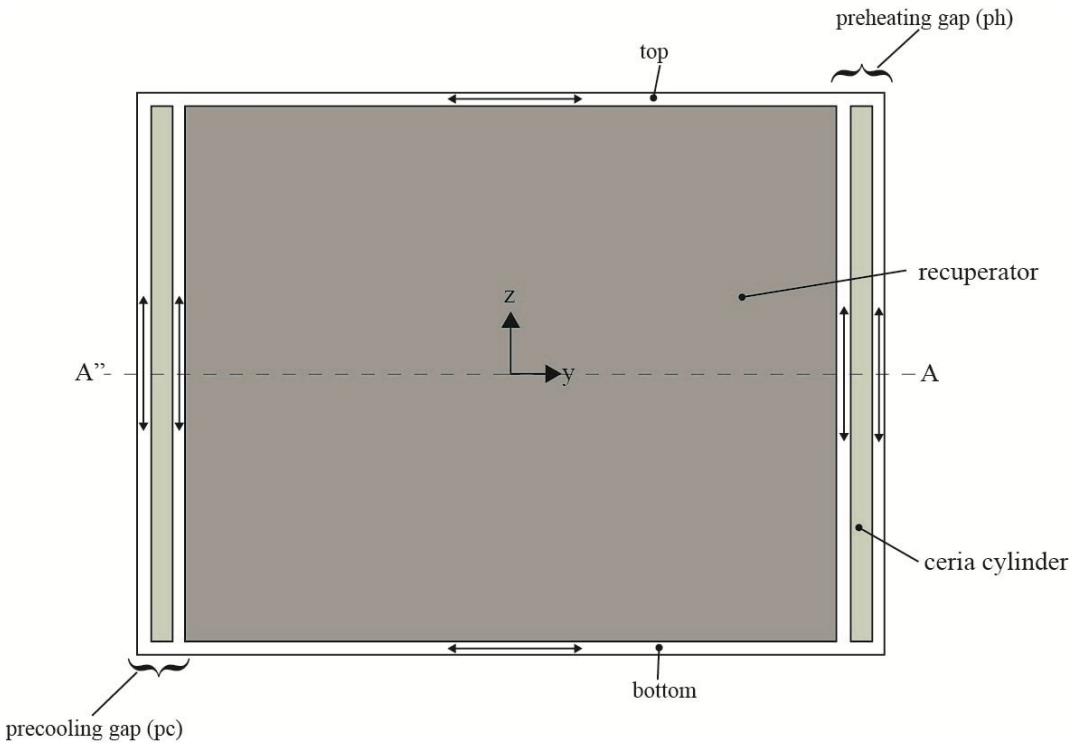

Figure 2.3: Side view of the 3D reactor with crossover paths

Parameter	Value
Porosity (γ)	0.75
Permeability (K)	3.8×10^{-12} m^2
Dupuit-Forchheimer coefficient (F_{DF})	17.5×10^{4} m^{-1}

Table 2.2: Material properties of porous ceria [20]

2.3 Governing Equations

The governing equations for the fluid flow model are outlined in this section. The Reynolds number at the inlets is 565 based on twice the width as characteristic length for the maximum mass flow rates considered in this study. This is well below the critical Reynolds number for flow between parallel plates of 2800. The flow in the gaps has much smaller Reynolds number than at the inlets. Hence, the flow within the reactor system is assumed to be laminar. All the simulation results are time invariant. Conservation of mass, species, momentum, energy equations are solved within the reactor system.

Mass conservation equation

$$\nabla \cdot \left(\rho_f \overline{\mathbf{V}} \right) = 0 \tag{2.1}$$

The fluid mixture within the reactor system cannot be treated as incompressible due to spatial changes in density of the mixture. The temporal term of the continuity equation is set to zero since we are interested in steady-state results of the simulations.

Momentum conservation equation

$$\nabla \cdot \left(\rho_f \overline{\mathbf{V}}\,\overline{\mathbf{V}}\right) = -\nabla p + \nabla \cdot \underline{\underline{\tau}} + \rho_f \overline{\mathbf{g}} \tag{2.2}$$

The left hand side of the equation represents the convective term - the acceleration of fluid with respect to the space independent of time. The right hand represents the summation of divergence of stress and body forces. The first term on the right hand side is the pressure gradient. The second term represents the divergence of shear stress. The third term includes body forces like gravity.

The stress tensor is given by the expression,

$$\underline{\underline{\tau}} = \mu\left[\left(\nabla\overline{\mathbf{v}} + \left(\nabla\overline{\mathbf{v}}\right)^{\mathrm{T}}\right) - \frac{2}{3}\left(\nabla \cdot \overline{\mathbf{v}}\right)\underline{\underline{\mathbf{I}}}\right] \tag{2.3}$$

Energy Conservation equation

$$\nabla \cdot \left(\overline{\mathbf{v}}\left(\rho_{\mathbf{f}} E + p\right)\right) = \nabla \cdot \left(k_f \nabla T - \sum_i h_i \bar{J}_i\right) + S_h \tag{2.4}$$

$E = h - p/\rho_f + \mathrm{v}^2/2$ is the total energy per unit volume. The enthalpy of the ideal gas mixture is calculated as the mass fraction weighted average of the individual enthalpies of species. The first term on the right hand side represents the heat transfer due to conduction. The second term represents the enthalpy transport due to diffusion of each species within the system. The third term represents any energy source within the system. Viscous dissipation is neglected ($Br \ll 1$).

Species conservation equation

In the current reactor model, four species are considered – N_2, O_2, CO_2, CO. The species conservation equation describes the transport of species *i* in the gas mixture due to diffusion and convective mass transfer, as well as species production and consumption due to chemical reactions:

$$\nabla \cdot (\rho_f \bar{\mathbf{v}} Y_i) = -\nabla \cdot \bar{\mathbf{J}}_i + S_i \tag{2.5}$$

The left hand side of the equation represents the species transport due to convection of species. The first term on the right hand side of the equation represents the species transport due to diffusion of each species. The last term takes into account any presence of chemical source/sink within the system.

In the current model, full scale multi-component method has been used to model mass diffusion within the fluid mixture. The diffusion flux of species i, $\bar{\mathbf{J}}_i$, is calculated from [21]

$$\bar{\mathbf{J}}_i = -\sum_{j=1}^{N-1} \rho_f D_{i,j} \nabla Y_j - D_{T,i} \frac{\nabla T}{T} \tag{2.6}$$

where $N = 4$ is the number of species present in the system. The multi-component diffusion coefficients $D_{i,j}$ are calculated from:

$$A_{i,i} = -\left(\frac{X_i M_f}{\mathcal{D}_{i,N} M_N} + \sum_{\substack{j=1 \\ j \neq i}}^{N} \frac{X_i M_f}{\mathcal{D}_{i,j} M_i} \right) \tag{2.7}$$

$$A_{i,j} = X_i \left(\frac{M_{\mathrm{f}}}{\mathcal{D}_{i,j} M_j} - \frac{M_{\mathrm{f}}}{\mathcal{D}_{i,N} M_N} \right) \text{ for } j \neq i \tag{2.8}$$

$$B_{i,i} = -\left(\frac{X_i M_{\mathrm{f}}}{M_N} + \left(1 - X_i\right) \frac{M_{\mathrm{f}}}{M_N} \right) \tag{2.9}$$

$$B_{i,j} = X_i \left(\frac{M_{\mathrm{f}}}{M_j} - \frac{M_{\mathrm{f}}}{M_N} \right) \text{ for } j \neq i \tag{2.10}$$

$$D = A^{-1} B$$

$\mathcal{D}_{i,j}$ are the binary diffusion coefficients, calculated from the Chapman-Enskog theory [22]:

$$\mathcal{D}_{i,j} = \frac{1.86 \cdot 10^{-3} T^{3/2} \left(1/\left(M_i \left[\mathrm{g/mol} \right] \right) + 1/\left(M_j \left[\mathrm{g/mol} \right] \right) \right)^{1/2}}{p \left[\mathrm{atm} \right] \sigma_{i,j}^2 \Omega} \tag{2.11}$$

where $\sigma_{i,j} = \left(\sigma_i + \sigma_j \right) / 2$ and Ω are the collision diameter and the collision integral, respectively. FLUENT computes the thermal diffusion coefficients using the empirically-based expression derived from [23]

$$D_{T,i} = -2.59 \times 10^{-7} T^{0.659} \left[\frac{M_i^{0.511} X_i}{\sum_{i=1}^{N} M_i^{0.511} X_i} - Y_i \right] \cdot \left[\frac{\sum_{i=1}^{N} M_i^{0.511} X_i}{\sum_{i=1}^{N} M_i^{0.489} X_i} \right] \tag{2.12}$$

The Lennard-Jones parameters σ and the energy parameter $\left(\varepsilon / k_B \right)$ for each species required to calculate the mass diffusivity of a mixture using kinetic theory are listed in Table 2.3 [21].

Additionally, continuity, momentum and species transport equations are solved within the porous region.

Species	Collision diameter $\sigma[\mathrm{A}]$	Energy parameter $\varepsilon/k_{\mathrm{B}}[\mathrm{K}]$
N_2	3.798	71.4
O_2	3.467	106.7
CO_2	3.941	195.2
CO	3.690	91.7

Table 2.3: Lennard-Jones potential parameters for different species [21]

Mass conservation equation

Mass conservation equation within the porous zone is written in terms of the true velocity. The right hand side represents the any mass source within the porous media.

$$\nabla \cdot \left(\rho_f \bar{\mathbf{v}} \gamma\right) = S_m \gamma \tag{2.13}$$

Momentum conservation equation

The Navier-Stokes equations are volume averaged to create macroscopic momentum equations for porous media. Kaviany [24] gives the following extended semi-empirical version of the Darcy equation in an attempt to account for the pore scale flow with macroscopic variables.

$$\nabla \cdot \left(\gamma \rho_f \overline{\mathbf{v}}\overline{\mathbf{v}}\right) = -\gamma \nabla p + \nabla \cdot \left(\gamma \underline{\underline{\tau}}\right) - \left(\frac{\gamma^2 \mu}{K}\overline{\mathbf{v}} + \gamma^3 F_{DF} \rho_f |\overline{\mathbf{v}}|\overline{\mathbf{v}}\right) \tag{2.14}$$

An additional momentum source term of the form of the extended Darcy's law accounts for the flow resistance due to the porous solid phase. The extended Darcy law consists of two terms. The first term is the Darcy term, where K is the permeability. The second term is the Forchheimer term representing the microscopic inertial force.

Species transport equation

$$\nabla \cdot (\gamma \rho_f \overline{\mathbf{v}} Y_i) = -\nabla \cdot (\gamma \overline{\mathbf{J}}_i) + \gamma S_i \tag{2.15}$$

The species transport equation is similar to that solved for in the fluid zone. S_i represents the chemical source/sink used to model the source or sink of O_2/CO/CO_2 within the porous ceria.

All the boundary conditions are summarized in the figure 2.2. The mass flow rates of the incoming gases mentioned in figure 2.2 is used in studies unless otherwise mentioned. The mass flux continuity is maintained at the interface between fluid and porous region.

The boundary conditions for equation (2.1) and (2.2) are

- At the walls of the reactor, no slip condition is imposed,

$$v_{wall} = 0 \tag{2.16}$$

- At CO_2 inlet, the mass flow rate is specified,

$$\dot{m}_{inlet} = \dot{m}_{CO_2} \text{ kg/s} \tag{2.17}$$

- At N_2 inlet, the mass flow rate is specified,

$$\dot{m}_{inlet} = \dot{m}_{N_2} \text{ kg/s} \tag{2.18}$$

- At outlets, the pressure is set to atmospheric pressure,

$$P_{outlet} = P_{atmosphere} = 1\text{atm} \tag{2.19}$$

The boundary conditions for equation (2.4) are

- At the walls of the reactor system, adiabatic boundary condition is imposed,

$$q''_{wall} = 0 \tag{2.20}$$

- At the inlets, the temperature of incoming species is specified,

$$\begin{aligned} T_{N_2 inlet} &= 1100\,K \\ T_{CO_2 inlet} &= 298\,K \end{aligned} \tag{2.21}$$

The oxidizer is supplied at the room temperature, 298 K. The maximum temperature of the incoming sweeping gas based on the heating system amounts to 1100 K. The temperature profiles of the ceria ring and the recuperator are determined from a separate heat transfer analysis by Lapp [18]. The radiative exchange is the main mode of heat transfer modeled between the cylinders, inner surfaces of the reactor body, cavity and within the ceria ring. Radiation losses via window, cavity are taken into account.

Convective heat transfer is modeled only in the reduction and oxidation zones to N_2 and CO_2, respectively. It is neglected in other regions and between the cylinders [18]. The temperature profile thus obtained is imposed on the ceria ring and the recuperator in the current study. The figure 2.4 shows the temperature profile (K) of the ceria cylinder. The main limitation of this assumption is that the temperature of the ceria ring remains independent of the flow conditions.

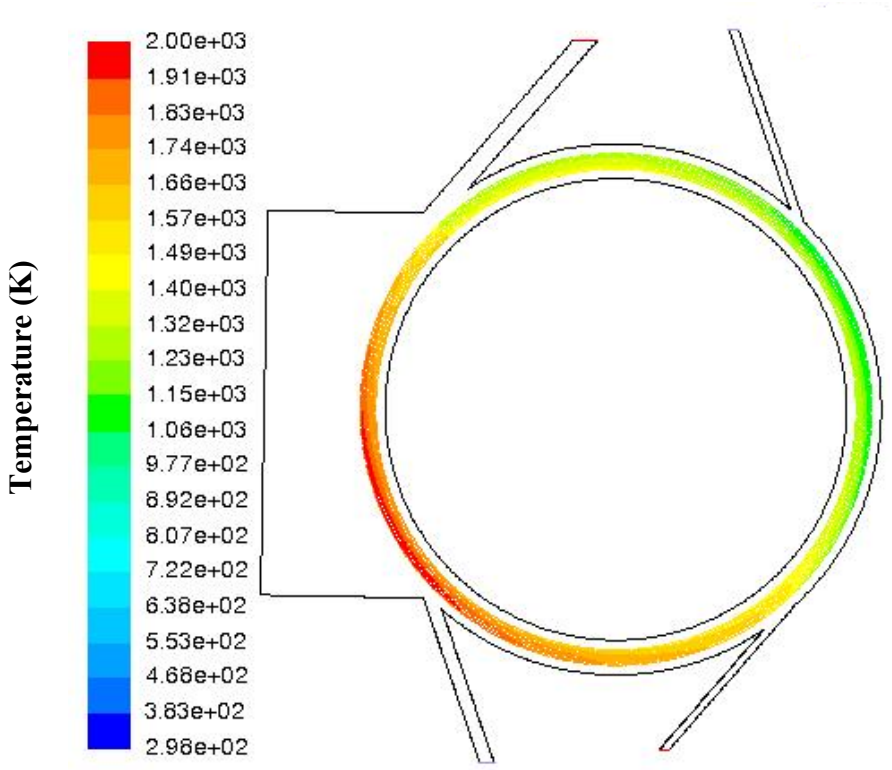

Figure 2.4: Temperature profile of the ceria ring [18]

The boundary conditions for equation (2.5) are

- At the walls of the reactor system, diffusive flux is zero,

$$\nabla Y_{wall} = 0 \tag{2.22}$$

- At the inlets, mass fraction of the particular species is set to 1. All the species are specified in the purest form.

$$\begin{aligned} Y_{N_2 inlet} &= Y_{N_2} = 1 \\ Y_{CO_2 inlet} &= Y_{CO_2} = 1 \\ Y_{CO source} &= Y_{CO} = 1 \\ Y_{O_2 source} &= Y_{O_2} = 1 \end{aligned} \tag{2.23}$$

2.4 Numerical solution

The computational domain of the reactor model in 2D and 3D are shown in figures 2.5, 2.6 and 2.7. All the equations are discretized using finite volume method and the resulting algebraic equations are solved in each control volume to yield solutions using FLUENT. The mass imbalance of less than 0.1% of the input values are observed in the final solutions. There are four species included in the reactor model – N_2, O_2, CO_2, CO. The mass flow rate expression at the inlets and outlets is calculated using eqn 2.24.

$$\dot{m}_{i,A} = \int_A Y_i(x,y,z) \cdot \dot{m}''_A(x,y,z) \cdot dA \tag{2.24}$$

For each of the species, the expression for mass imbalance is given in eqn 2.25.

$$\begin{aligned} \Delta\dot{m}_{O_2} &= \dot{m}_{O_2 inlet} - \dot{m}_{CO_2 outlet} - \dot{m}_{N_2 outlet} \\ \Delta\dot{m}_{N_2} &= \dot{m}_{N_2 inlet} - \dot{m}_{CO_2 outlet} - \dot{m}_{N_2 outlet} \end{aligned} \tag{2.25}$$

$$\Delta \dot{m}_{CO} = \dot{m}_{COinlet} - \dot{m}_{CO_2\,outlet} - \dot{m}_{N_2 outlet}$$

$$\Delta \dot{m}_{CO_2} = \dot{m}_{CO_2 inlet} - \dot{m}_{CO_2 outlet} - \dot{m}_{N_2 outlet}$$

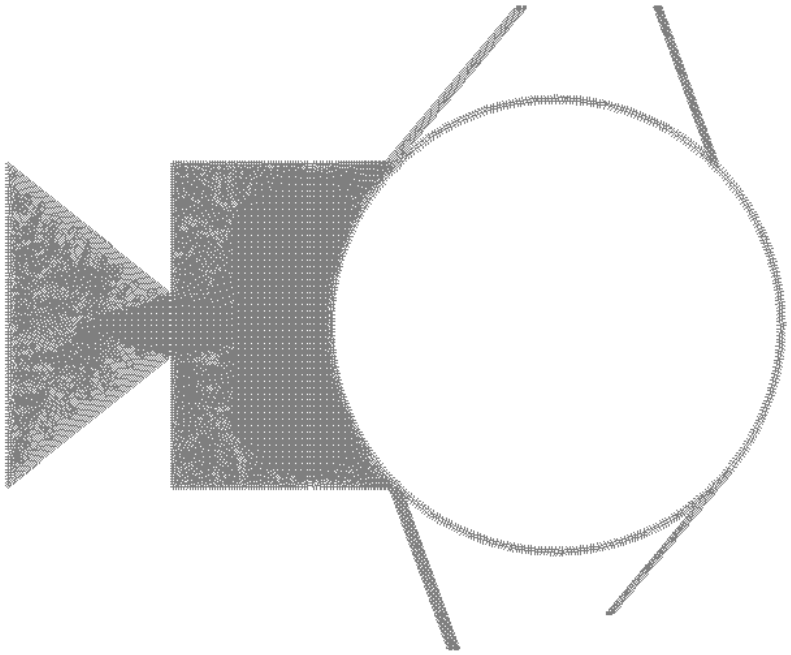

Figure 2.5: Mesh of the simplified 2D reactor model

Each of the expressions should be equal to zero for exact solutions. However, for all simulations in this study, the mass imbalance of 0.1% of the input values or less is considered acceptable (appendix A). This desired accuracy is achieved with a scaled residual ratio of 10^{-4} or less.

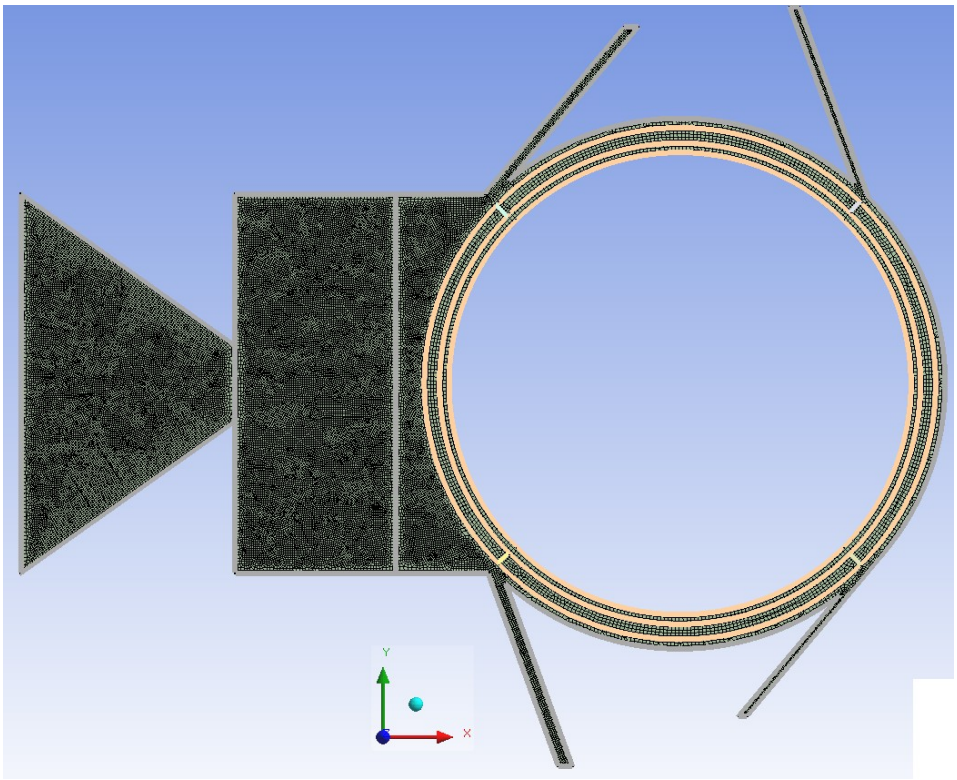

Figure 2.6: Mesh of the 2D reactor model with porous ceria ring

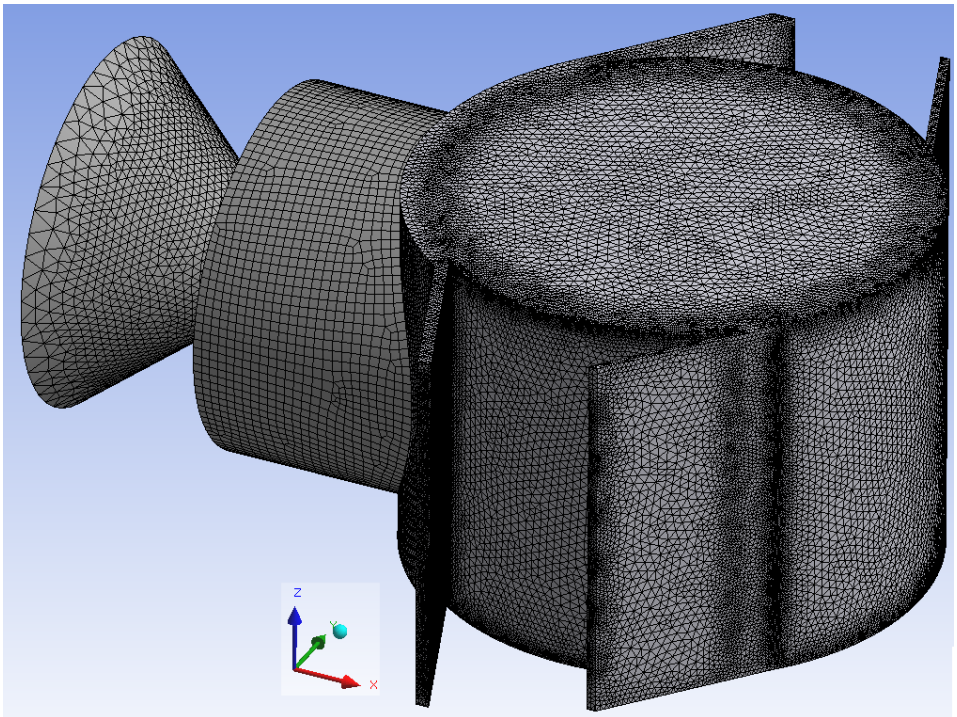

Figure 2.7: Mesh of the 3D reactor model

2.5 Material Properties

All the material properties such as dynamic viscosity, thermal conductivity, specific heat capacity of individual species are assumed to be temperature dependent. The co-relations of the properties of individual species with respect to temperature are provided in Appendix B [21-23, 25-27]. The diffusion coefficients are calculated based on kinetic theory, mentioned in section 2.3. The properties of the mixture are calculated based on mass fraction weighted average of the individual properties (Appendix C).

2.6 Methodology

The three main geometric parameters associated with the gas channels are shown in figure 2.1. They are the angular positions of the inlets/outlets (θ), width of the inlets/outlets (w), and circumferential position of the channels (α). These parameters are determined with respect to the other dimensions of the reactor system mentioned in table 2.1. The inlet/outlet geometry dimensions are optimized with respect to the species' crossover value (***C***). The crossover for each species is calculated as follows.

$$\boldsymbol{C}_{O2} = \frac{\dot{m}_{O_2}\big|_{CO_2\ outlet}}{\dot{m}_{O_2}\big|_{O_2\ source}} \tag{2.26}$$

$$\boldsymbol{C}_{CO2} = \frac{\dot{m}_{CO_2}\big|_{N_2\ outlet}}{\dot{m}_{CO_2}\big|_{CO_2\ inlet}} \tag{2.27}$$

$$\boldsymbol{C}_{CO} = \frac{\dot{m}_{CO}\big|_{N_2\ outlet}}{\dot{m}_{CO}\big|_{CO\ source}} \tag{2.28}$$

$$C_{N2} = \frac{\dot{m}_{N_2}\big|_{CO_2\ outlet}}{\dot{m}_{N_2}\big|_{N_2\ inlet}} \tag{2.29}$$

The simplified 2D reactor model described is utilized for most of the test runs. The final two runs involve 2D reactor model with porous ceria ring and the 3D reactor model, respectively. The set of parametric study is given in table 2.4.

The parametric study with simplified 2D reactor model involves varying the angle and the width of the inlets/outlets. To begin with, the width of the inlet/outlet on the oxidation side is set to 5mm, while that on the reduction side is set to 7.5mm to account for higher flow rates. The angle of the inlets is set to 0°. The angle of the outlets is set tangential to 40°. The inlets/outlets are positioned just outside the reduction and oxidation zones (50°). The angle of the N_2 inlet is changed from 0° to 20° to 40°. For each case, the angle of the N_2 outlet is also varied from 40° to 20° to 0°. Based on these 9 simulations, the angle of N_2 inlet and outlet is set. These constitute the set of runs 1-3 in table 2.4. Next, the angles of CO_2 inlet and the CO_2 outlet are varied individually in runs 4-5. Runs 6-9 involve varying the widths of the inlets/outlets. A 2D reactor model with ceria ring and recuperator is used for test run 10. The circumferential position of N_2 inlet is varied to reduce the O_2 crossover via the pre-cooling gap. A 3D reactor model is used to vary the width of N_2 outlet from 7.5mm to 10mm to 12.5mm to reduce the O_2 crossover.

Runs	Model	Angle of N_2 inlet (θ_1)	Angle of CO_2 inlet (θ_3)	Angle of N_2 outlet (θ_4)	Angle of CO_2 outlet (θ_2)	Width of N_2 inlet (w_1)	Width of N_2 outlet (w_4)	Width of CO_2 inlet (w_3)	Width of CO_2 outlet (w_2)	Circumferential position of N_2 inlets (α_1)
1	2D	0°	0°	40°, 20°, 0°	40°	7.5 mm	7.5 mm	5 mm	5 mm	50°
2	2D	20°	0°	40°, 20°, 0°	40°	7.5 mm	7.5 mm	5 mm	5 mm	50°
3	2D	40°	0°	40°, 20°, 0°	40°	7.5 mm	7.5 mm	5 mm	5 mm	50°
4	2D	20°	40°, 20°, 0°	40°	40°	7.5 mm	7.5 mm	5 mm	5 mm	50°
5	2D	20°	20°	40°	40°, 20°, 0°	7.5 mm	7.5 mm	5 mm	5 mm	50°
6	2D	20°	20°	40°	40°	7.5, 10, 12.5 mm	7.5 mm	5 mm	5 mm	50°
7	2D	20°	20°	40°	40°	7.5 mm	7.5, 10, 12.5 mm	5 mm	5 mm	50°
8	2D	20°	20°	40°	40°	7.5 mm	7.5 mm	10, 7.5, 5 mm	5 mm	50°
9	2D	20°	20°	40°	40°	7.5 mm	7.5 mm	5 mm	10, 7.5, 5 mm	50°
10	2D (ceria ring)	20°	20°	40°	40°	7.5 mm	7.5 mm	5 mm	5 mm	46°, 49°, 52°, 55°
11	3D	20°	20°	40°	40°	7.5 mm	7.5, 10, 12.5 mm	5 mm	5 mm	55°

Table 2.4*:* Parametric study of the inlet/outlet geometry

2.7 Results

The table 2.5.a, b, c gives the species' crossover values (***C***) and the varied geometric parameter at each test run. The mass flow rate of N_2 is the largest compared to flow rates of other species in the reactor model. It is expected that the N_2 inlet/outlet geometry affects the overall crossover to a greater extent. Hence, the first three set of parametric study involved varying the angle of N_2 inlet/outlet. After the first three sets, angle of N_2 inlet/outlet were fixed for the rest of the parametric study. Set 4 and 5 involved the variation of angles of CO_2 inlet/outlet. After set 5, the angles of all the inlets/outlets were fixed. Set 6 to 9 includes the parametric study of widths of the inlets/outlets. Set 10 involved the parametric study of the circumferential positioning of N_2 inlet. Sets 1-9 were carried out using the 2D model with impermeable cylinder acting as ceria cylinder. Set 10 was carried out using the 2D model with porous ceria ring. Set 11 was carried out using the 3D model of the reactor. Hence, it can be observed that there is a significant increase of crossover values for the last two runs.

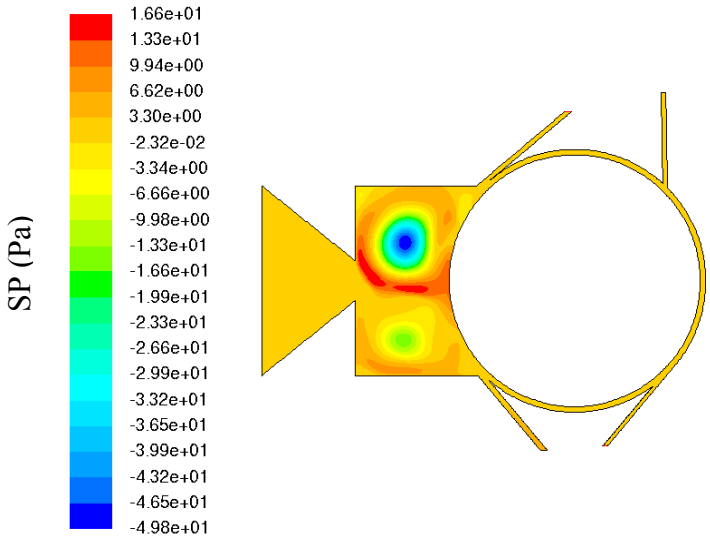

Figure 2.8: Static pressure (Pa) (gauge) within the reactor

Runs	Model	Angle of N_2 inlet (θ_1)	Angle of CO_2 inlet (θ_3)	Angle of N_2 outlet (θ_4)	Angle of CO_2 outlet (θ_2)	Width of N_2 inlet (w_1)	Width of N_2 outlet (w_4)	Width of CO_2 inlet (w_3)	Width of CO_2 outlet (w_2)	Circumferential position of N_2 inlets (α_1)	Crossover values (%)			
											N_2	O_2	CO_2	CO
1	2D	0°	0°	0°	40°	7.5	7.5	5 mm	5 mm	50°	12	0	99	34
				20°							12	0	85	12
				40°							12	0	44	1
2	2D	20°	0°	0°	40°	7.5 mm	7.5 mm	5 mm	5 mm	50°	12	2	86	0
				20°							12	2	52	2
				40°							12	2	0	0
3	2D	40°	0°	0°	40°	7.5 mm	7.5 mm	5 mm	5 mm	50°	Reverse flow at the outlets			
				20°										
				40°										
4	2D	20°	0°	40°	40°	7.5 mm	7.5 mm	5 mm	5 mm	50°	12	2	0	0
			20°								8	0	2	0
			40°								8	0	22	0

Table 2.5a: Crossover values of species for the parametric study

Runs	Model	Angle of N_2 inlet (θ_1)	Angle of CO_2 inlet (θ_3)	Angle of N_2 outlet (θ_4)	Angle of CO_2 outlet (θ_2)	Width of N_2 inlet (w_1)	Width of N_2 outlet (w_4)	Width of CO_2 inlet (w_3)	Width of CO_2 outlet (w_2)	Circumferential position of N_2 inlets (α_1)	Crossover values (%)			
											N_2	O_2	CO_2	CO
5	2D	20°	20°	40°	0°	7.5 mm	7.5 mm	5 mm	5 mm	50°	16	0	0	0
					20°						12	3	0	0
					40°						8	0	2	0
6	2D	20°	20°	40°	40°	7.5 mm	7.5 mm	5 mm	5 mm	50°	8	0	2	0
						10 mm					10	0	1	0
						12.5 mm					10	3	0	0
7	2D	20°	20°	40°	40°	7.5 mm	7.5 mm	5 mm	5 mm	50°	8	0	2	0
							10 mm				5	0	53	0
							12.5 mm				3	0	69	4
8	2D	20°	20°	40°	40°	7.5 mm	7.5 mm	5 mm	5 mm	50°	8	0	2	0
								7.5 mm			8	0	2	0
								10 mm			8	0	9	1

Table 2.5b: Crossover values of species for the parametric study

Runs	Model	Angle of N_2 inlet (θ_1)	Angle of CO_2 inlet (θ_3)	Angle of N_2 outlet (θ_4)	Angle of CO_2 outlet (θ_2)	Width of N_2 inlet (w_1)	Width of N_2 outlet (w_4)	Width of CO_2 inlet (w_3)	Width of CO_2 outlet (w_2)	Circumferential position of N_2 inlets (α_1)	Crossover values (%)			
											N_2	O_2	CO_2	CO
9	2D	20°	20°	40°	40°	7.5 mm	7.5 mm	5 mm	5 mm	50°	8	0	2	0
									7.5 mm		16	5	0	0
									10 mm		20	9	0	0
10	2D (ceria ring)	20°	20°	40°	40°	7.5 mm	7.5 mm	5 mm	5 mm	46°	19	9	0	0
										49°	19	8	0	0
										52°	19	7	0	0
										55°	19	6	0	0
11	3D	20°	20°	40°	40°	7.5 mm	7.5 mm	5 mm	5 mm	55°	28	15	0	0
							10 mm				16	10	0	0
							12.5 mm				10	6	8	0

Table 2.5c: Crossover values of species for the parametric study

Set 3 involved variation of angle of N_2 outlet for fixed N_2 inlet angle of 40°. Reverse flow is observed at N_2 outlet for this set of simulations. The crossover values are not calculated for these simulations. Figure 2.8 shows the static pressure plot for one of these cases. The negative static pressure leads to reverse flow at N_2 outlet. Hence, N_2 inlet angle of 40° is not considered.

The flow is always from reduction side to the oxidation side in the pre-cooling zone. The N_2 crossover of 8-12% represents the leakage of N_2 via pre-cooling zone. With changes in geometric parameters, the only observable change in flow pattern is in the pre-heating zone. For the fixed flow rates of CO_2 and N_2, the direction of fluid flow through pre-heating zone changes based on the changes in geometric parameters. Thus, the direction of the flow in the pre-heating zone ultimately influences the amount of crossover and also determines the species which undergoes crossover. High crossover values of CO_2 in runs 1-2 indicate that the flow direction in the pre-heating gap is from oxidation to reduction side. Correspondingly, there is nil or low crossover of O_2 and N_2 via pre-heating gap.

Increasing the widths of the inlets does not have noticeable effect on the crossover. However, the widths of the outlets (set 7 & 9) have a greater effect on the amount of crossover, especially N_2 outlet. Increasing N_2 outlet width (set 7) decreases N_2, O_2 crossover but increases CO_2, CO crossover. Similarly, increasing CO_2 outlet (set 9) width increases N_2, O_2 crossover but decreases CO_2, CO crossover.

It can also be observed that O_2 crossover is negligible in set 1 to 9. However, in set 10, O_2 crossover increases to 9%. This is due to the change in the way O_2 source is

modeled, the inclusion of porous ceria ring and the additional gap between ceria ring and the recuperator. For sets 1 to 9, O_2 source is modeled as mass inlet along the circumference of the cylinder (figure 2.1) and N_2 sweeps away all of the O_2. For set 10, O_2 source is modeled as a volumetric source within the porous ceria ring (figure 2.2). Due to low permeability of the porous ring, only part of the O_2 is swept away by N_2 and the remaining O_2 within the ceria ring and the inner gap crosses over. This leakage of O_2 can be reduced by positioning the N_2 inlet away from the reduction zone as observed from set 10, thus reducing the O_2 crossover via pre-cooling gap.

Final set of simulations (set 11) are carried out to alter the width of the N_2 outlet to minimize the crossover. In set 11, N_2 outlet with 12.5 mm is chosen (over N_2 outlet of 10 mm) as the optimum geometry due to lower O_2 crossover value. O_2 crossover leads to reduction in the overall efficiency of the reactor, as explained in section 1.3. It should be noted that the optimum geometry for the 2D and 3D cases are different. In case of 2D model, any further increase in the N_2 outlet width leads to high crossover of CO_2.

The tables 2.6, 2.7 provide the optimum geometry dimensions of inlets/outlets for 2D and 3D cases, respectively. The crossover of each species for optimum geometry for 2D and 3D cases are given in table 2.8. All the crossover values are rounded off to the nearest integer. Crossover values of each species for the same dimensions of 2D and 3D model of the reactor are tabulated in table 2.9. From table 2.9, it is clear that the crossover values is different for 2D and 3D reactor models of same geometry.

Geometric parameters	Value
Angle of N_2 inlet (θ_1)	20°
Angle of CO_2 inlet (θ_3)	20°
Angle of N_2 outlet (θ_4)	40°
Angle of CO_2 outlet (θ_2)	40°
Width of N_2 inlet (w_1)	7.5 mm
Width of N_2 outlet (w_4)	7.5 mm
Width of CO_2 inlet (w_3)	5 mm
Width of CO_2 outlet (w_2)	5 mm
Circumferential position of inlets, outlets (α)	50° (55° for N_2 inlet)

Table 2.6: Optimum inlet/outlet geometry for 2D model

Geometric parameters	Value
Angle of N_2 inlet (θ_1)	20°
Angle of CO_2 inlet (θ_3)	20°
Angle of N_2 outlet (θ_4)	40°
Angle of CO_2 outlet (θ_2)	40°
Width of N_2 inlet (w_1)	7.5 mm
Width of N_2 outlet (w_4)	12.5 mm
Width of CO_2 inlet (w_3)	5 mm
Width of CO_2 outlet (w_2)	5 mm
Circumferential position of inlets, outlets (α)	50° (55° for N_2 inlet)

Table 2.7: Optimum inlet/outlet geometry for 3D model

	N_2	O_2	CO_2	CO
2D	19	6	0	0
3D	10	6	8	0

Table 2.8: Crossover values (%) of species for optimum inlet/outlet geometries in 2D and 3D

	N_2	O_2	CO_2	CO
2D	19	6	0	0
3D	25	16	0	0

Table 2.9: Crossover values (%) of species for the same geometry in 2D and 3D

The tables 2.1 and 2.6, 2.7 provide the details of the dimensions of the overall reactor system used for simulations in all subsequent sections. Note that these dimensions are optimum with respect to the flow rate conditions discussed earlier.

2.8 Conclusions

The crossover of the species within the reactor is dependent on the inlet and outlet flow conditions. Once those conditions are fixed, the crossover values of the species is dependent on the inlet/outlet geometry. The parametric study of the geometric variables is carried out to determine an inlet/outlet geometry with minimum crossover of the species. The flow direction in pre-cooling gap is unaffected by the changes in geometric parameters. The flow direction in the pre-heating gap ultimately influences the crossover species and their values. In other words, changes in geometric parameters causes changes in the pressure difference between the CO_2 inlet and N_2 outlet which influences the

crossover values. Based on the study, crossover values are the most sensitive to orientation and the width of N_2 outlet. For the optimum geometry, there is no crossover of fuel. The O_2 crossover may result in maximum reduction in fuel output of 6%. The O_2 crossover is lower than 6% for other flow conditions for the optimized geometry. The N_2 and CO_2 crossovers are 10% and 8% respectively. Quantifying the changes in the fuel output due to N_2 and CO_2 crossover requires detailed chemical modeling and is not part of the study. Further, 3D model of the reactor provides more accurate crossover values as compared to 2D reactor model.

3.0 Effect of physical properties of porous ceria ring

3.1 Introduction

The porous ceria ring in the reactor model is characterized by porosity (γ), permeability (K) and Forchheimer coefficient (F_{DF}). The porosity indicates the volume of voids relative to the total volume. The permeability and the Forchheimer coefficient indicate the viscous and inertial resistance to the flow in the porous medium, respectively [24]. The material used in the chemical cycling of the reactor can be either monolith porous ceria [20] or the reticulated porous ceramic (RPC) material [28]. Their permeability can range from 10^{-12} m^2 to 10^{-7} m^2. The variation in permeability changes the fluid flow across the ceria ring and thus alters the crossover values. The objective of this study is to observe the changes in fluid flow field with the variation in properties of the ceria ring.

3.2 Methodology

The 2D reactor model with porous ceria ring previously described is utilized for this study, shown in figure 3.1. The dimensions of the reactor are given in table 2.1 and 2.6.

The governing equations and the procedure for numerical solution are explained in the previous chapter. The mass flow rates of the sweep gas and the oxidizer and the overall boundary conditions of the reactor model are unchanged from the previous chapter. The following cases, as tabulated in table 3.1, are evaluated and the observations are noted down.

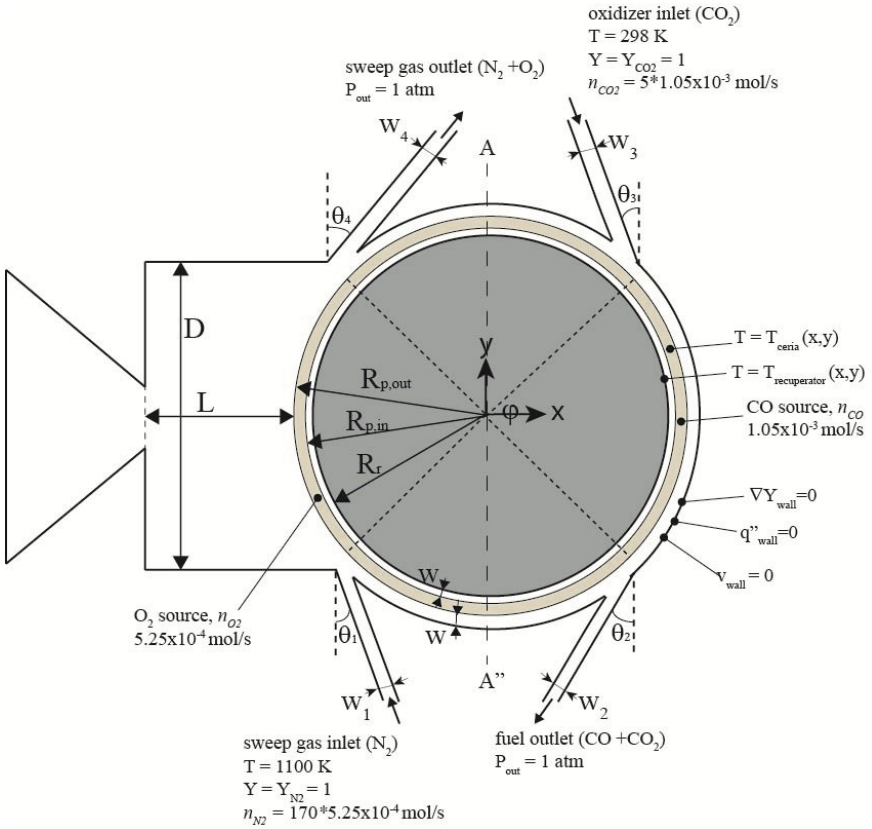

Figure 3.1: 2D reactor model with ceria ring with boundary conditions

	Permeability (K) (m^2)	Forchheimer coefficient (F_{DF}) (m^{-1})
Case I	$3.8x10^{-12}$	$17.5x10^4$
Case II	$3.8x10^{-6}$	0
Case III	∞	0

Table 3.1: Physical properties of ceria used in test cases

Case I corresponds to the porous ceria modeled in the previous section from Haussener *et al.* [20]. Case II involves only the permeability value increased by 6 orders of magnitude. In the final case, Case III, permeability value is set to infinity, thus allowing for maximum flow of the species through the porous media. The final case is tantamount to increasing the crossover gap between the oxidation and reduction zone

from 10 mm to 18 mm. Thus, evaluating these cases provides a good picture of the functioning of the reactor with respect to different materials used within the reactor. The porosity value is set to 0.75 in all these cases for comparison.

3.3 Results

For Case I, the maximum value of the velocity within the porous media reaches 10^{-4} m/s. The Reynolds number within the porous media is given by

$$\mathrm{Re}_{por} = \frac{\rho v l}{\mu}$$

where, l is the characteristic length. For the current work, the characteristic length is obtained from the specific interfacial area [20] as 1/706 mm. With these values,

$$\mathrm{Re}_{por} \approx 4 \times 10^{-6}$$

Since, $\mathrm{Re}_{por} << 1$, the flow can be well defined using Darcy law and the inertial losses can be neglected. Another measure of Darcy flow is given by Forchheimer number,

$$Fo = \frac{K F_{DF} \rho v}{\mu}$$

The Forchheimer number is the ratio of the inertial term to the Darcy term in equation 2.6. It is found to be $\approx 2 \times 10^{-6}$. Such a low value of Forchheimer number indicates that the Darcy law is sufficient to model the fluid flow within the porous ceria ring [29]. Thus, Forchheimer coefficient can be ignored to model the ceria within the reactor system.

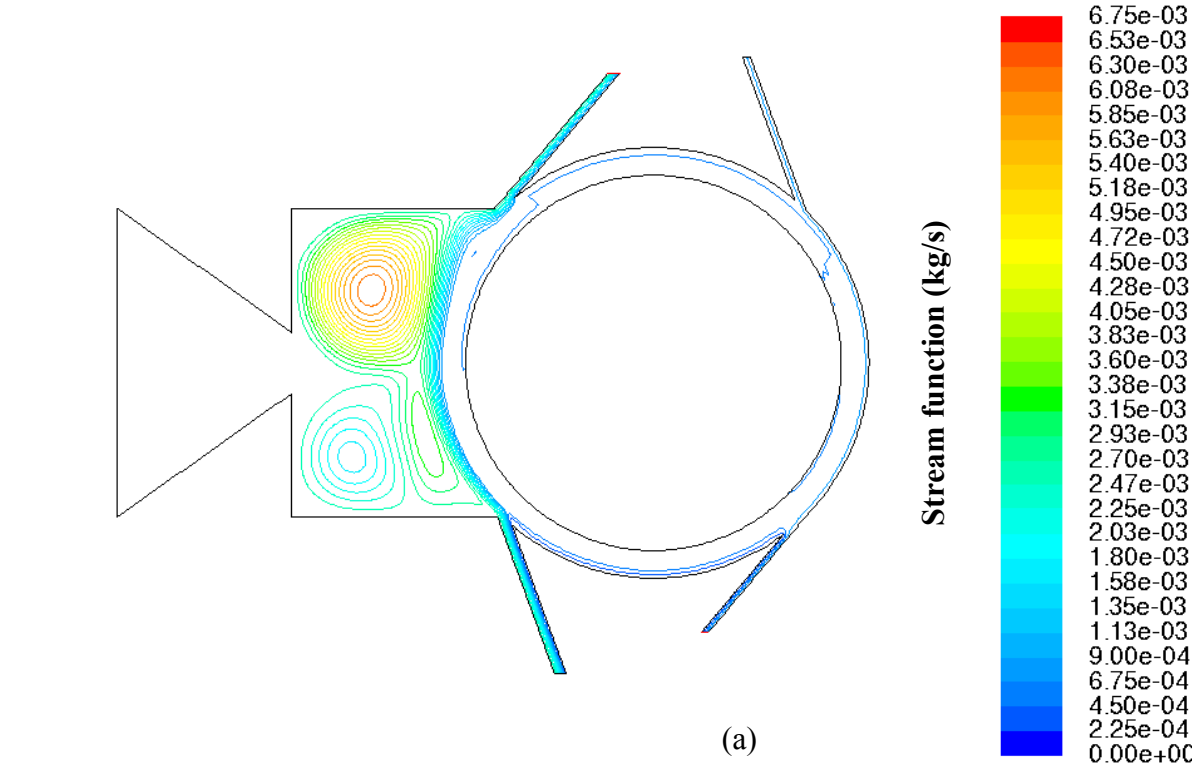

(a)

(b) (c)

Figure 3.2: Streamlines for a) Case I, K=3.8x10^{-12} m^2, b) Case II, K=3.8x10^{-6} m^2, c) Case III, K=∞

Figure 3.2 shows the streamlines for the three cases. Figure 3.2a shows the streamlines for the lowest permeability. Figure 3.2b shows the streamlines for the higher permeability (by 6 orders). Figure 3.2c shows the streamlines for infinite permeability of the ceria ring. The figures depict the flow field as the permeability of the ceria ring varies for 3 distinct cases.

It is observed that the shape of the streamlines is similar for Cases I and III within the cavity. However, for case I, there are very few streamlines passing through the ceria ring. For case III, streamlines are observable within the entire ceria ring except within the pre-cooling region. For case II, there are streamlines passing through the ceria ring, however, the shape of the streamlines is completely different from the other cases. For case II, the high velocity N_2 stream flows through the ceria ring, hits the recuperator wall and loses speed. Then it follows the least resistance path and flows out of the ceria ring. This creates a large recirculation zone in the reduction zone towards the N_2 outlet. Figure 3.3 shows the velocity field in the cavity for case II.

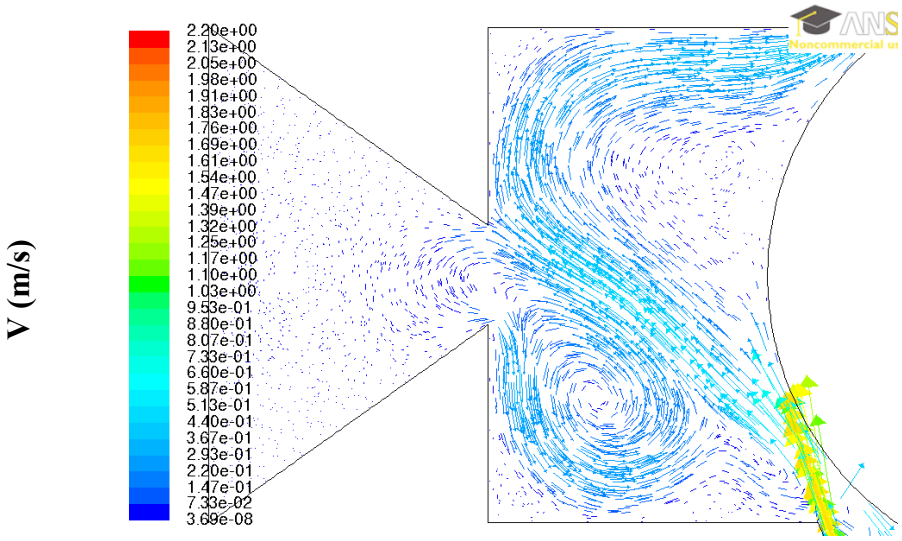

Figure 3.3: Velocity field in the cavity for $K=3.8x10^{-6}$ m^2

The O_2 partial pressure (atm) within the reactor is shown in the figure 3.4 for three cases. Figure 3.4a shows the O_2 partial pressure plot for the ceria ring with the lowest permeability. Figure 3.4b shows the plot for the higher permeability (by 6 orders). Figure 3.4c shows the O_2 partial pressure for infinite permeability of the ceria ring. The O_2 partial pressure plot gives a relative measure of the non-stoichiometry of the ceria ring within the reactor. Lower the O_2 partial pressure observed within the reduction zone, higher is the non-stoichiometry of the ceria, greater the fuel output of the reactor.

Among the cases, the O_2 partial pressure is the least for case III. Since, the ceria ring has the highest permeability in this case, N_2 stream sweeps through the ceria ring to produce the lowest O_2 partial pressure within the ceria ring. Similarly, case II has the highest O_2 partial pressure in the reduction zone. This region corresponds to the region of recirculation zone in the cavity as observed in figure 3.3. Among all three cases, O_2 concentration ($<10^{-3}$ atm) is the lowest in the pre-cooling region. Increasing the permeability leads to increasing concentration of O_2 in the oxidation zone, as seen from the figures. This is corroborated from the crossover values table 3.2 presented later in the section.

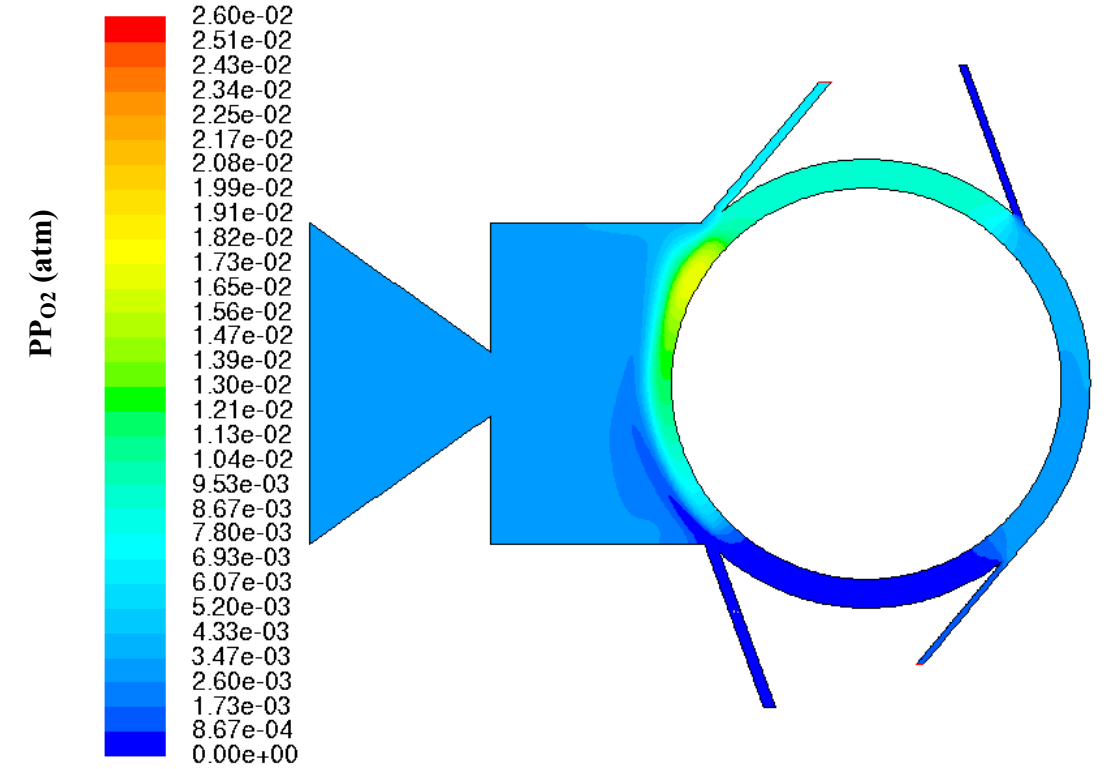

(a)

(b) (c)

Figure 3.4: O_2 partial pressure (atm) within the reactor a) case I, b) case II, c) case III

The variation of the O_2 partial pressure (atm) along the curve length of the reduction zone is presented for all three cases in figure 3.5 at r=0.135 m, r=0.131 m, r=0.127 m respectively. The exit of the reduction zone (N_2 inlet) is represented by the beginning of the curve length.

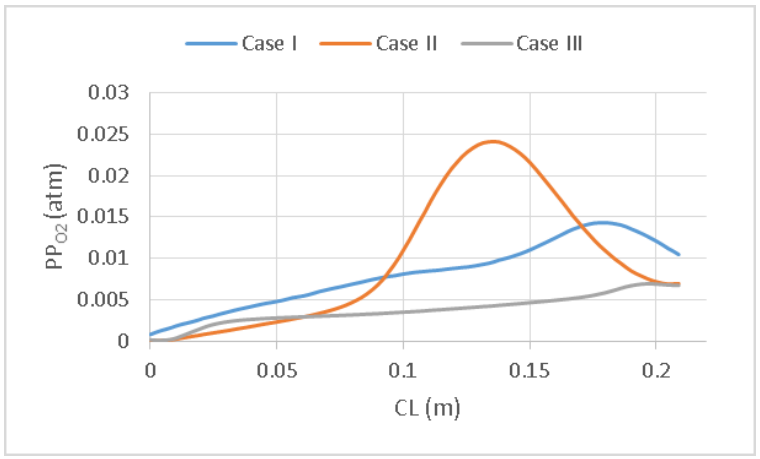

(a)

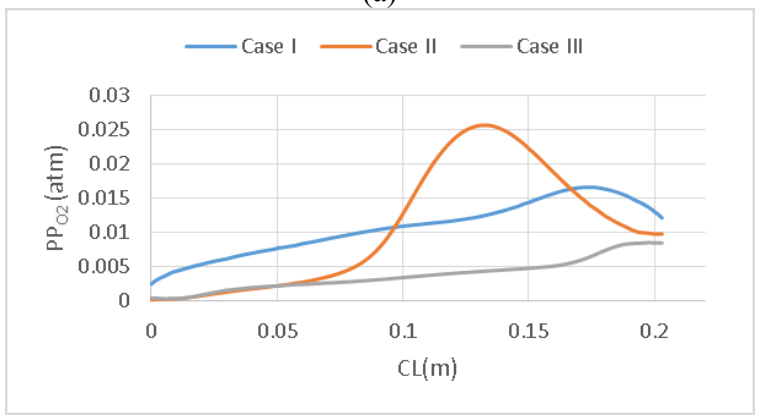

(b)

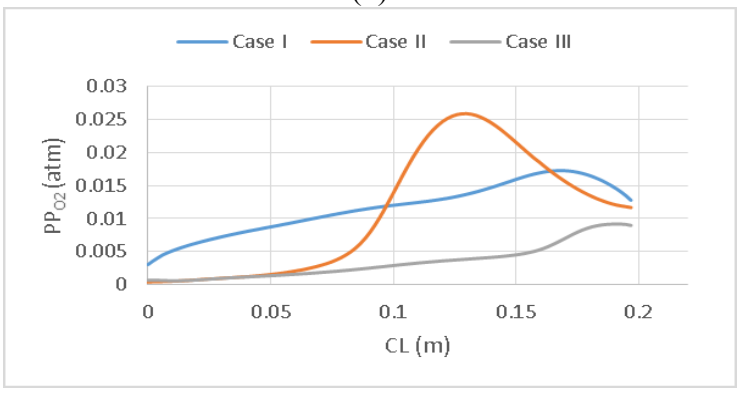

(c)

Figure 3.5: O_2 partial pressure (atm) along the curve length for all cases at (a) r=0.135 m, (b) r=0.131 m, (c) r=0.127m

From the figures 3.5, the general trend observed is that O_2 partial pressure increases along the reduction zone as we move from N_2 inlet to N_2 outlet. The O_2 concentration increases only slightly as we move towards the inner surface of the ceria

ring. Hence, the O_2 partial pressure only at the surface of the ceria ring is reported, henceforth.

The mean O_2 partial pressure for 3 cases are $8x10^{-3}$ atm, $9.7x10^{-3}$ atm and $3x10^{-3}$ atm at r=0.135 m. If the mean O_2 partial pressure is used as a criteria for fuel output, then the monolith ceria has a slightly lower PP_{O2}. However, increasing the permeability in general, lowers the average PP_{O2}. Even in this case, the curve of case II PP_{O2} follows that of case III until the quarter length of the reduction zone and then rises rapidly due to the recirculation zone.

The u-velocities at the pre-cooling and pre-heating gaps along the y-axis are a good measure of the crossover. Hence, they are plotted along the y position for all three cases in figure 3.6. The position 0.135 to 0.127 m in pre-heating gap and -0.135 to -0.127 m in pre-cooling gap represents the porous ceria ring. The porous ceria ring is surrounded by fluid region on both the sides. The blue line represents the u-velocities for case I which has the lowest permeability of the ceria ring among all the cases. The orange line represents case II which as higher permeability compared to case I. The grey line represents case III which has the highest permeability of the ceria ring. The figures depict the changes in local u-velocities of the fluid mixture with the changes in permeability of the ceria ring. The u-velocities at both pre-cooling and pre-heating zone are positive, indicating that the net flow in both these regions is from reduction to oxidation side within the reactor.

In the pre-cooling gap, for case I, the low permeability of the ceria ring causes the u-velocity to drop from 0.38 m/s in the fluid region to the orders of 10^{-7} m/s within the

porous ring. The u-velocity is negligible within the inner gap between the ceria ring and the recuperator. For case II, the higher permeability of the ceria ring provides lower resistance to the fluid flow within the ceria ring. The minimum u-velocity within the ceria ring in the pre-cooling gap is 0.08 m/s for case II. The u-velocity profile for case II is close to parabolic on both the sides with a dip in the middle representing the relatively less permeable ceria ring. For case III, the entire pre-cooling gap acts as a single fluid region (due to infinite permeability of the porous media) and parabolic velocity profile is observed. The mean u-velocities decrease as the permeability of the ceria ring is increased (case I to case III). This indicates that the leakage of the fluid mixture (N_2+O_2) through the pre-cooling gap decreases with the increase in the permeability of the ceria ring. This result is proven through the crossover values of each species, shown later.

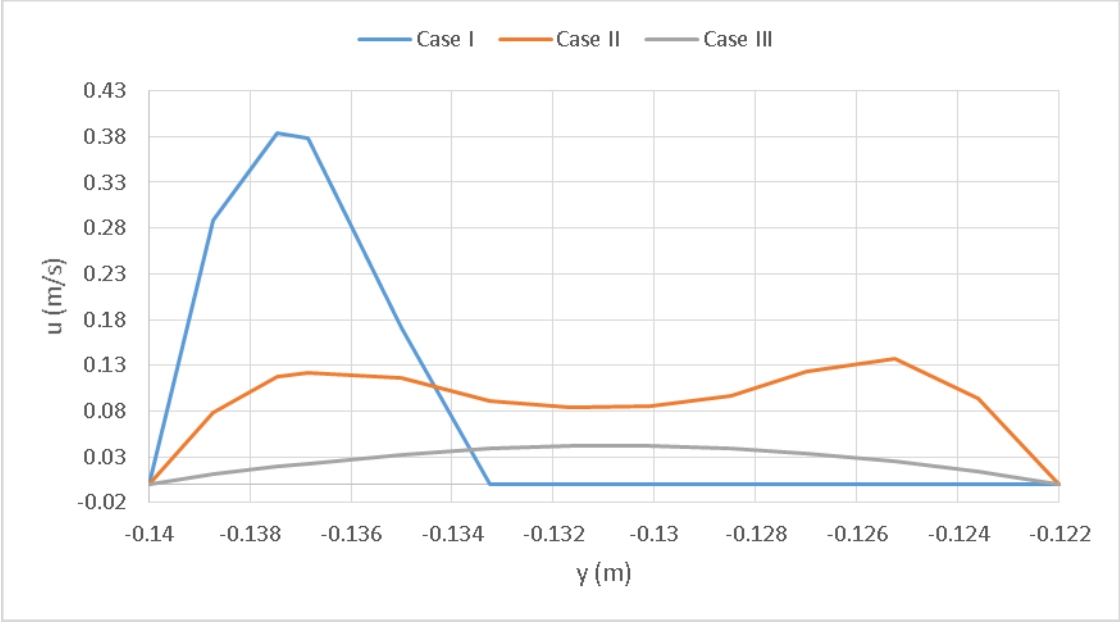

(a)

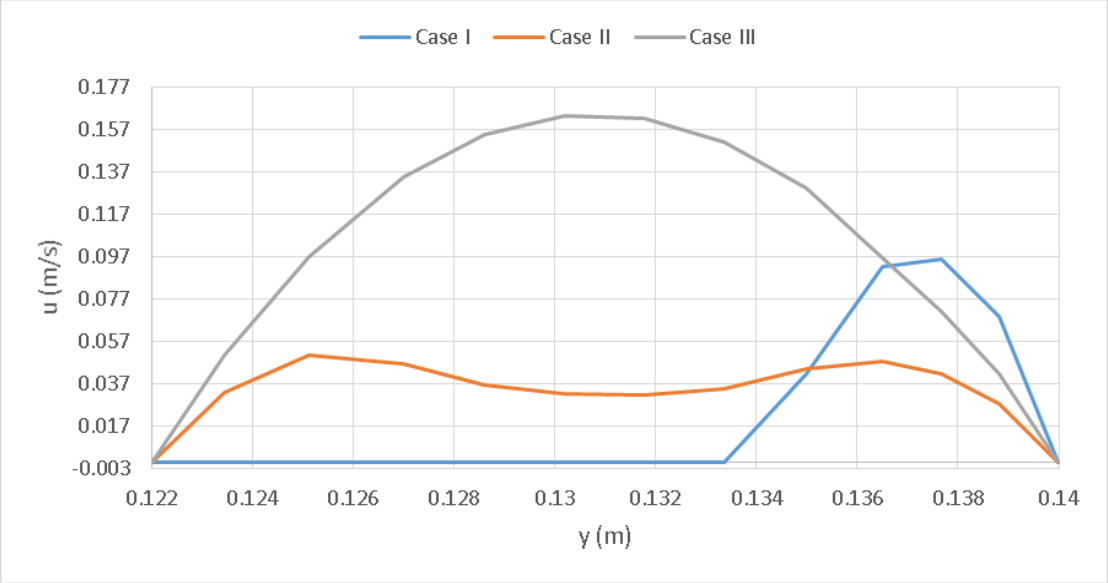

(b)

Figure 3.6: u-velocities for all cases at (a) pre-cooling gap at ϕ=270°, (b) pre-heating gaps at ϕ=90°

Similar profiles for u-velocities can be observed in the pre-heating gap for all three cases. However, the magnitude of the velocities are quite different from the pre-cooling region. For case I, the maximum u-velocity in the pre-heating gap is 0.097 m/s, way lower than 0.38 m/s observed in the pre-cooling gap. Thus, for case I, the leakage of fluid mixture is higher through the pre-cooling gap compared to the pre-heating gap. The mean u-velocities in the pre-heating gap increase with the increase in the permeability of the ceria ring (case I to case III). For case III, the mean u-velocity is 0.1 m/s, much higher than 0.025 m/s observed in the pre-cooling region. Thus, the leakage of the fluid mixture (N_2+O_2) through the pre-heating gap increases with the increase in the permeability of the ceria ring. This result is corroborated through the crossover values of each species, shown later.

Static pressure field within the reactor is shown for all the cases in figure 3.7. For cases II and III, there is no noticeable static pressure difference within the reactor. The low permeability of the ceria ring in case I leads to negligible flow and thus, higher pressure gradient across the ceria ring.

From figure 3.7, for case I, it is clear that the region of interest for pressure gradient lies within the ceria ring and the regions just adjacent to it. Figure 3.8 shows the static pressure as a function of the position at different locations within the reactor. The static pressure is plotted within the pre-cooling and pre-heating gaps at x=0 line, and within the reduction and oxidation gaps at y=0 line. From figure 3.7, it is clear that the pressure gradient points towards the recuperator. The low permeability of the ceria ring leads to steep pressure gradient and negligible flow across the ring. The static pressure variation within the ceria ring can be approximated as linear and constant slope can be calculated.

Static pressure across the ceria ring and the inner fluid region is shown in figure 3.8. The plots show the variation of the static pressure at a) pre-cooling gap b) pre-heating gap c) reduction gap d) oxidation gap for case I. The static pressure gradient is constant in the reduction and oxidation zone and is around 650 Pa/m, while in the pre-cooling and pre-heating gap it is around 400 Pa/m.

Figure 3.9 provides the CO_2 concentration plots within the reactor for all three cases. It is clear that the spread of CO_2 is restricted only to the oxidation zone. The partial pressure of CO_2 is close to zero in all other regions within the reactor. However, for case III, it can be observed that CO_2 concentration in the oxidation region is lower compared

to that of the other two cases. This clearly points to higher leakage of the fluid mixture (N_2+O_2) from the reduction to the oxidation side and thus, diluting the CO_2 concentration within the oxidation region. Thus, higher permeability of the ceria ring leads to higher crossover of the fluid mixture into the oxidation side.

The crossover values of each species for different cases are mentioned in table 3.2. The numbers indicate the leakage of each species as a fraction with respect to their input values. From the table, it is observed that there is no crossover of CO_2, CO. For case I, the total leakage of N_2 is 20% of its incoming stream. Similarly, the O_2 crossover is 7% of its incoming mass flow rate. When the permeability of the ceria ring is low (for cases I, II), the leakage of N_2 is higher via pre-cooling gap. Lower permeability of the ceria ring acts as a barrier for the incoming N_2 stream, thus, branching it. For case III, N_2 stream is unobstructed and as a result, N_2 leakage via pre-cooling is significantly lesser than other cases. For O_2, almost all of the leakage happens through pre-heating gap

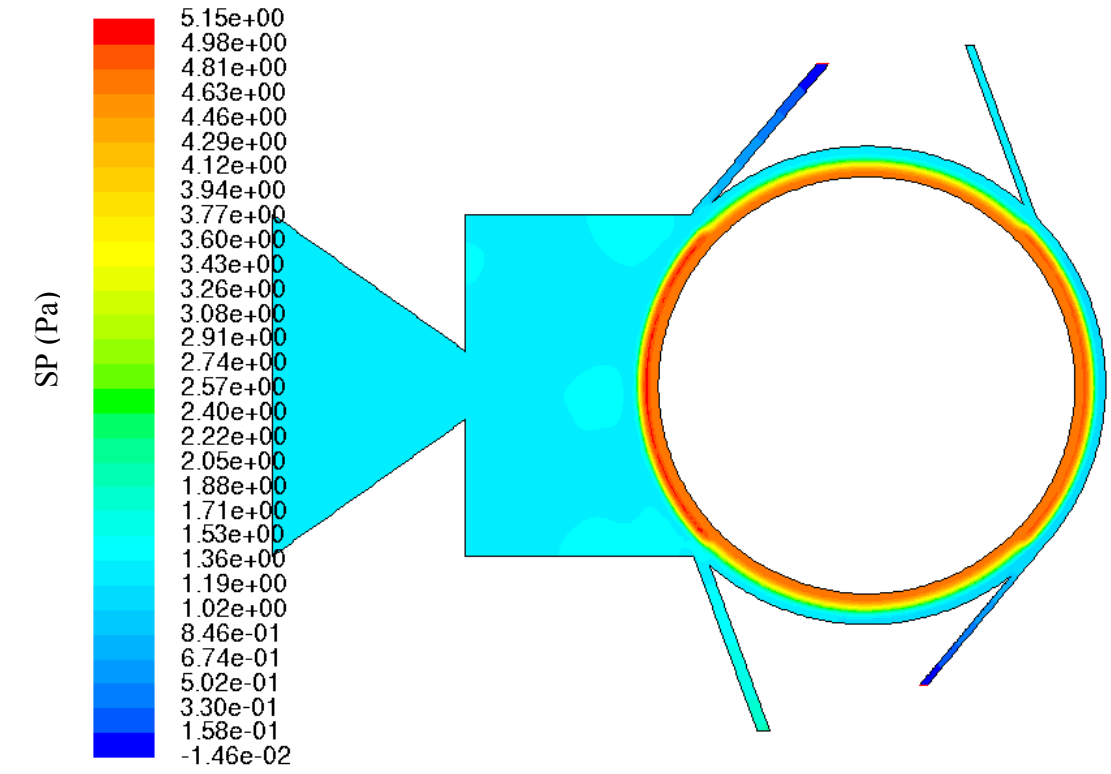

(a)

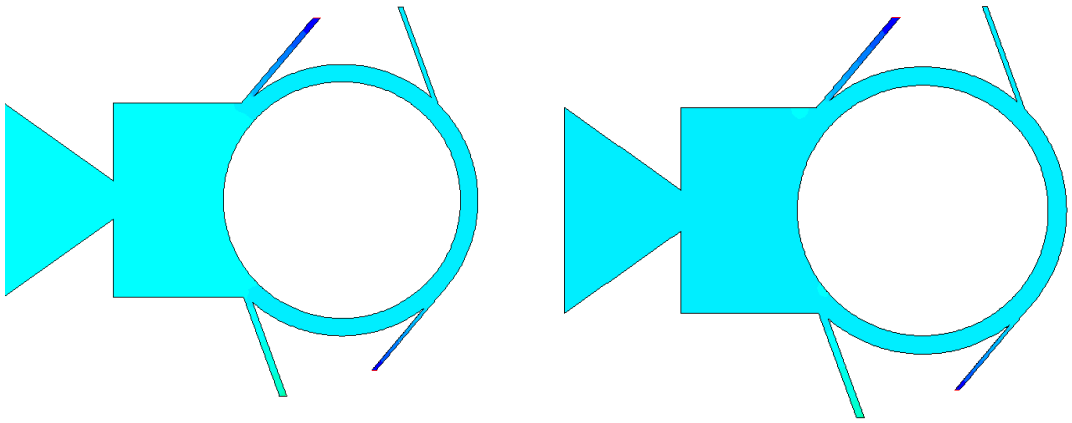

(b) (c)

Figure 3.7: Static pressure (Pa) (gauge) within the reactor for a) $K=3.8\times10^{-12}$ m^2, b) $K=3.8\times10^{-6}$ m^2, c) $K=\infty$

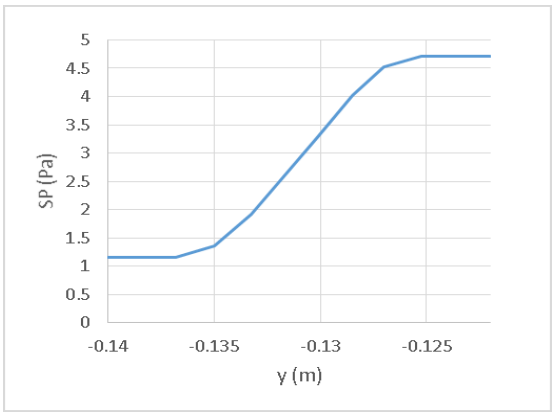

(a)

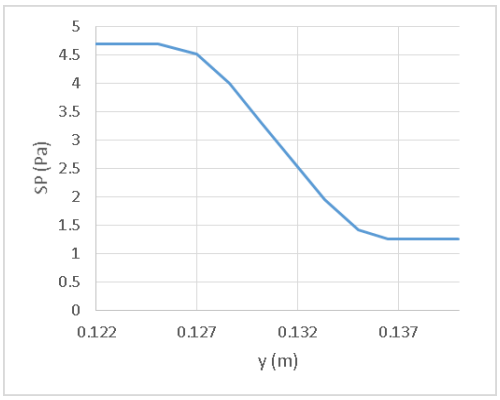

(b)

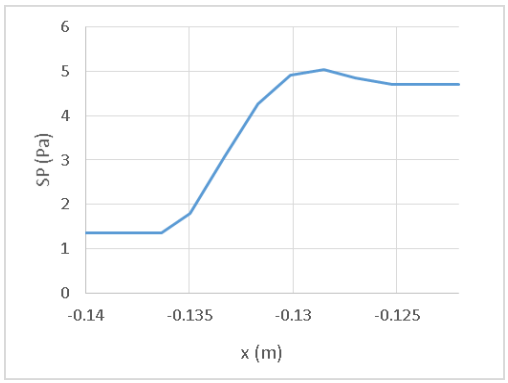

(c)

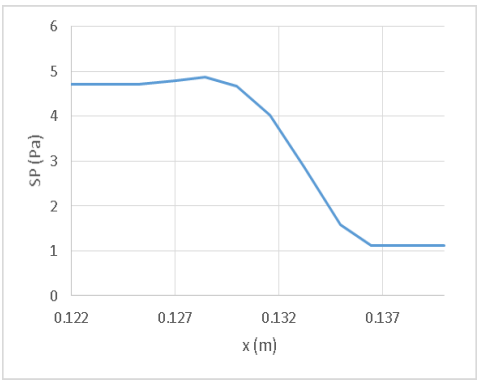

(d)

Figure 3.8: Static pressure along position for case I at (a) ϕ=270°, (b) ϕ=90°, (c) ϕ=180°, (d) ϕ=0°

for all three cases. The overall crossover of N_2 and O_2 increases with increase in the permeability of the ceria ring. Thus, lowering the permeability of the ceria ring leads to higher crossover of the species on the reduction side.

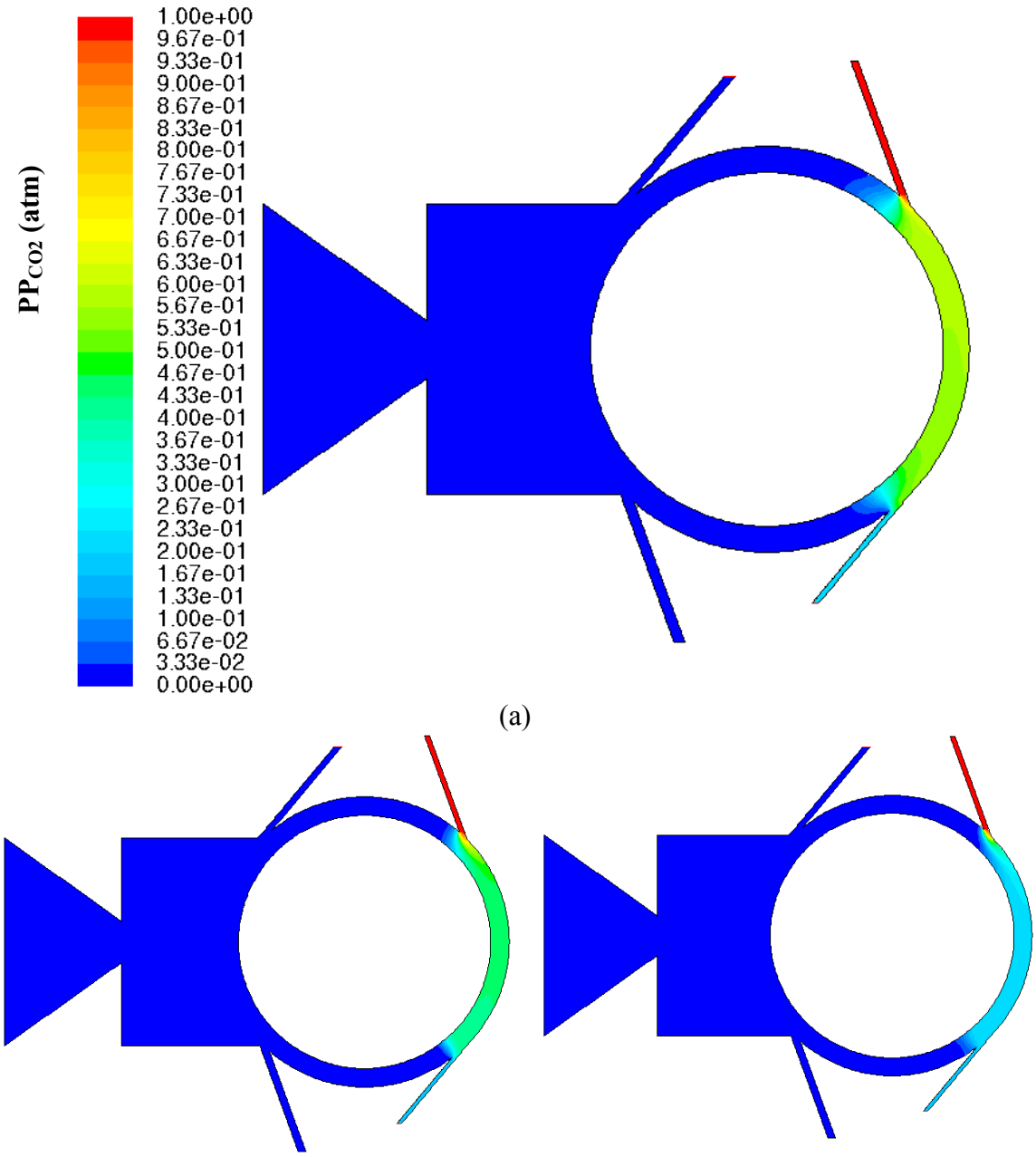

Figure 3.9: CO_2 partial pressure (atm) within the reactor for (a) case I, (b) case II, (c) case III

	N_2		O_2		CO_2	CO
	Pre-cooling gap	Pre-heating gap	Pre-cooling gap	Pre-heating gap		
Case I	16	4	1	6	-	-
Case II	17	7	1	13	-	-
Case III	5	20	1	25	-	-

Table 3.2: Crossover values (%) for $K=3.8x10^{-12}$ m^2, $K=3.8x10^{-6}$ m^2, $K=\infty$

It is also noted that for case I, 0.07% of the total flow through the gap flows through ceria ring, while for case II, this increases to 38% due to increased permeability. It is important to note that for the permeability range 10^{-12} to 10^{-8} m^2, there is very little change in streamlines or the crossover (<1%). Further increase in permeability, however, results in rapid increase in crossover values as shown.

3.4 Conclusions

The 2D reactor model with porous ceria ring is simulated with different permeability of the porous ring. The Forchheimer number is lows so that the flow through ceria ring is governed by Darcy flow and the inertial losses are negligible. The general trend for the mean O_2 partial pressure in the reduction zone is to decrease with higher permeability of the ceria ring. However, for the case evaluated in this study ($K\sim10^{-6}$ m^2), the mean PP_{O2} shows a slight increase due to larger PP_{O2} in the recirculation zone. With the increase in permeability ($K\sim10^{-6}$ m^2), the crossover of N_2 and O_2 increases through the pre-heating gap, with almost negligible change in the flow through pre-cooling gap. With permeability set to infinity, overall the crossover values increase. Since

there is no obstruction to the flow of N_2 by the ceria ring, most of the sweep gas flows through the reduction zone and thus, crossover of N_2 via pre-cooling gap decreases significantly. In general, it is observed that increasing the permeability leads to higher crossover of the fluid from the reduction side. The reduction in fuel output due to O_2 crossover is 7% for monolith ceria whereas it is 14% for RPC material. The monolith ceria is recommended based on the lower O_2 crossover and thus, higher fuel output potential.

4.0 Effect of rotation of the ceria ring

4.1 Introduction

The cycling of the ceria from the high temperature to the low temperature region and back is achieved by the rotation of the ceria ring. Among the reduction and oxidation reactions, reduction step is the faster one and the oxidation reaction is the rate determining step [30]. The solid heat recovery is also affected by rotation speed of the ceria ring and the recuperator [18]. Based on these considerations, the rotation speed is set to 0.2 rpm in counter-clockwise direction. The recuperator rotates in clockwise direction at the same speed resulting in solid phase heat recovery. In the current study, the fluid flow field is observed for two rotation speeds a) 0.2 rpm, b) 1 rpm both in counter-clockwise direction and compared with respect to the reactor model with stationary ceria ring as discussed in the previous chapter.

4.2 Methodology

The 2D reactor model with porous ceria ring described previously is utilized for this study. However, the ceria ring rotates with 0.2 rpm in counter-clockwise direction and the recuperator rotates with 0.2 rpm in clockwise direction. The properties of the monolith ceria (table 2.2) are used for this study.

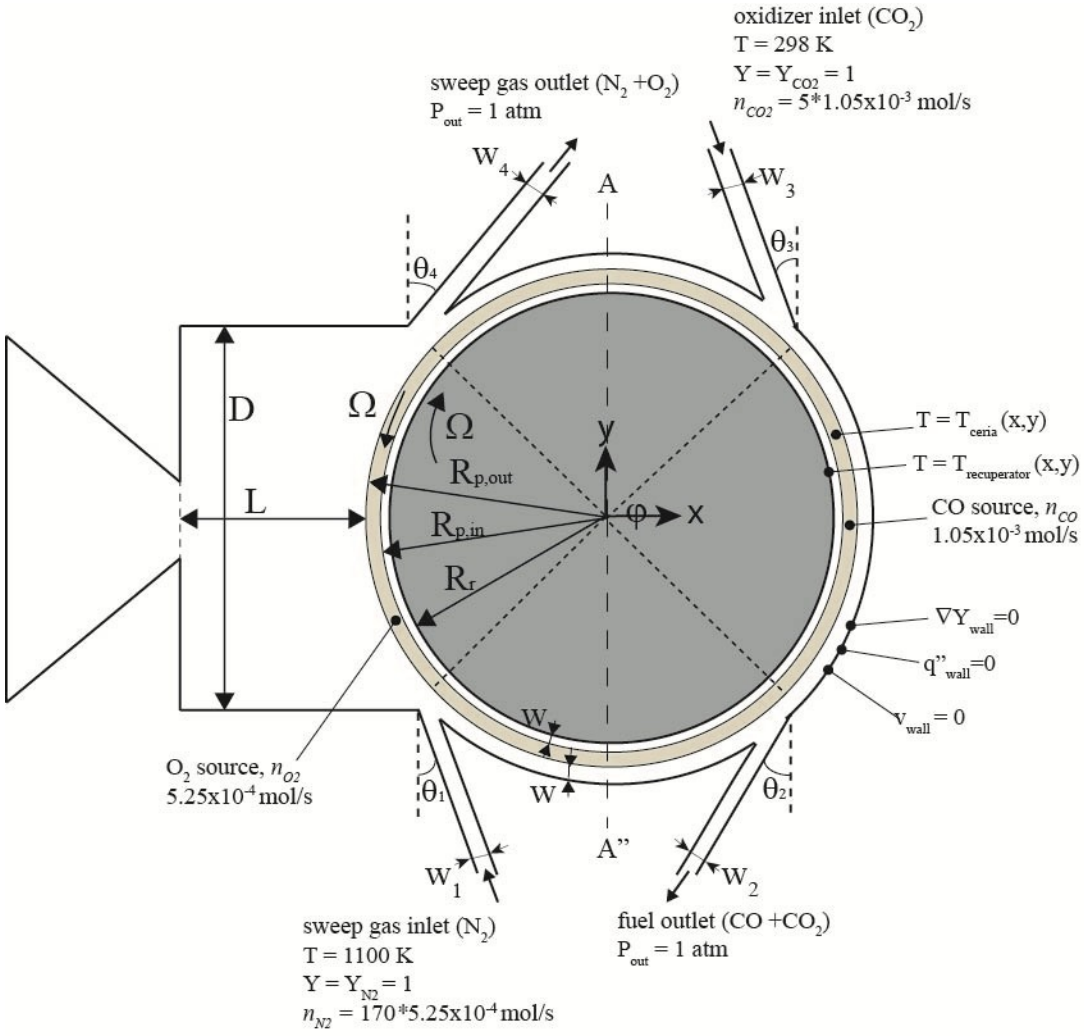

Figure 4.1: 2D reactor model with rotating ceria ring

The governing equations mentioned in section 2.3 still hold in the fluid region. However, equations within the porous media is written with respect to the rotating frame of reference.

4.3 Governing Equations

The governing equations of the flow inside the steadily rotating porous ceria cylinder are expressed with respect to a non-inertial coordinate system that rotates at the angular velocity of the ceria cylinder, $\overline{\Omega}$, and whose z-axis is coincident with the z-axis

of the inertial coordinate system (x, y). Primes denote operations and vectors relative to the rotating reference frame. Eulerian approach is adopted for the porous zone, in the sense that, the mesh is fixed and the fluid particles pass through it. The velocity within the porous zone in the governing equations implies the true velocity. The continuity, momentum and the species transport equations are given below.

$$\nabla' \cdot \left(\rho_{\mathrm{f}} \bar{\mathbf{v}}' \gamma \right) = S_{\mathrm{m}} \gamma \tag{3.1}$$

$$\nabla' \cdot \left(\gamma \rho_{\mathrm{f}} \bar{\mathbf{v}}' \bar{\mathbf{v}}' \right) = -\gamma \nabla' p + \nabla' \cdot \left(\gamma \underline{\underline{\boldsymbol{\tau}}}' \right) - \gamma \rho_{\mathrm{f}} \left(\underbrace{\quad}_{\text{Coriolis}} \quad \underbrace{\quad}_{\text{centrifugal}} \right) - \underbrace{\left(\frac{\gamma^2 \mu}{K} \bar{\mathbf{v}}' + \gamma^3 F_{\mathrm{DF}} \rho_{\mathrm{f}} \left| \bar{\mathbf{v}}' \right| \bar{\mathbf{v}}' \right)}_{\text{extended Darcy law}} \tag{3.2}$$

$$\nabla \cdot (\gamma \rho \bar{\mathbf{v}}' Y_i) = -\nabla \cdot (\gamma \bar{\mathbf{J}}_i') + \gamma S_i \tag{3.3}$$

The apparent body forces, the Coriolis force, and the centrifugal force, appear due to the rotation of the reference frame in the momentum equation. Other equations are similar to those described in section 2.3 but are expressed with respect to the rotational frame of reference.

4.4 Results

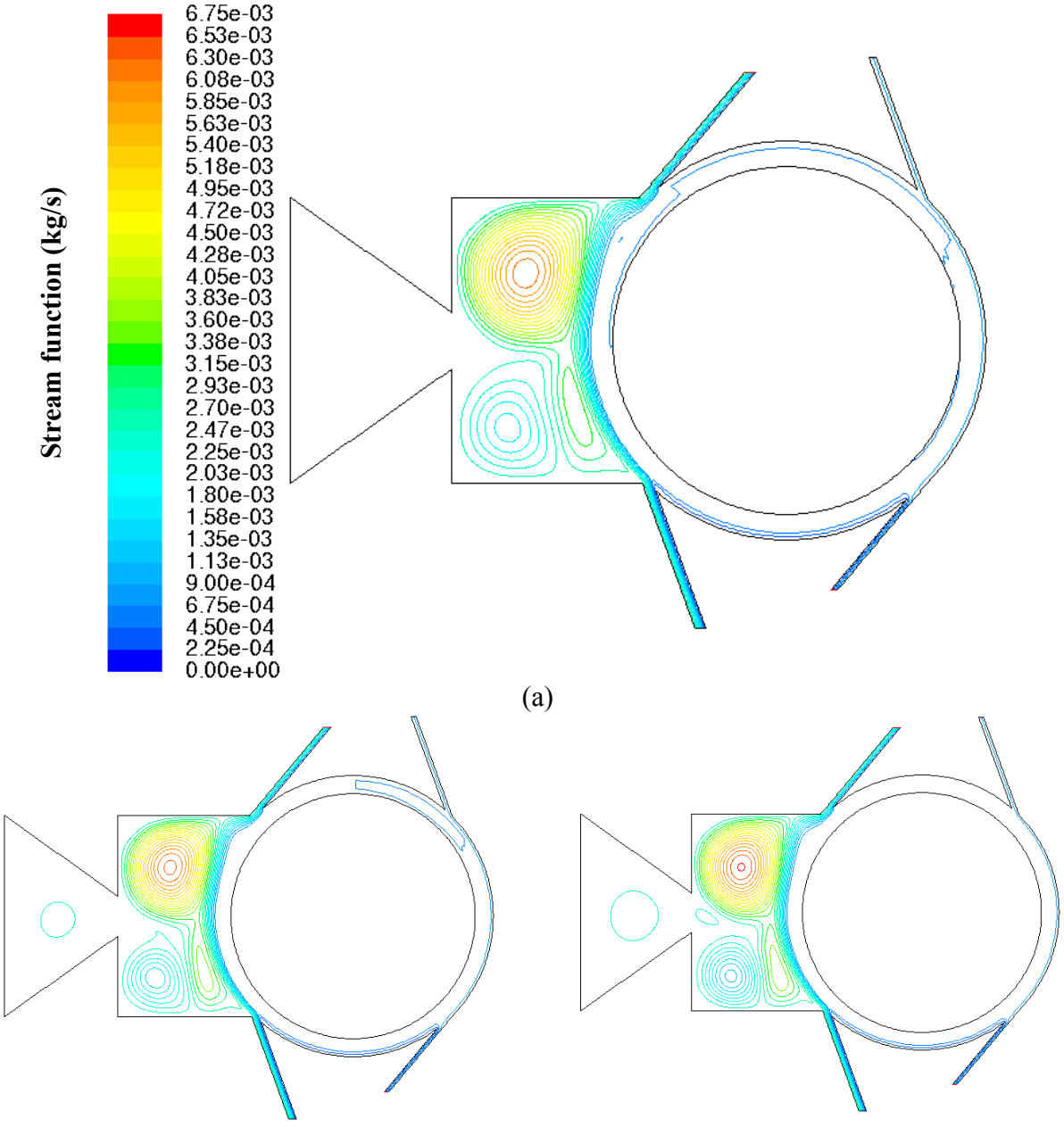

Figure 4.2: Streamlines with ceria ring rotation speed of a) 0 rpm, b) 0.2 rpm, c) 1 rpm

Figure 4.2 shows the streamlines within the reactor for different rotation speeds of a) 0 rpm, b) 0.2 rpm, c) 1 rpm. The streamlines within the cavity and the crossover gaps are similar on a qualitative basis.

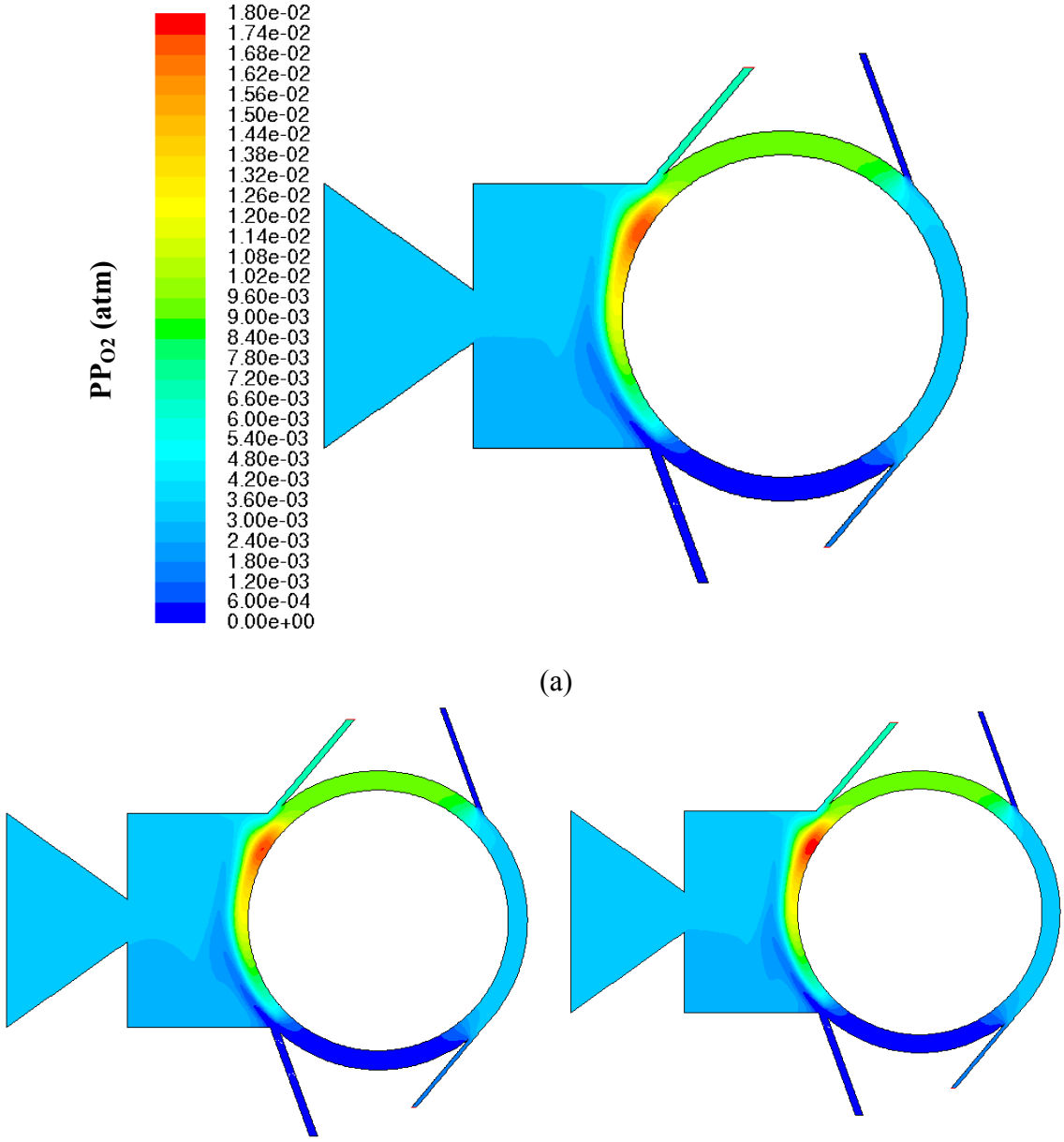

Figure 4.3: O_2 partial pressure in the reactor with ceria ring rotation speed of a) 0 rpm, b) 0.2 rpm, c) 1 rpm

Figures 4.3 provide the O_2 partial pressure within the reactor for three cases. The profiles of the O_2 concentration within the reactor are similar for all cases. For the case with 1 rpm rotation of the ceria ring, the highest O_2 partial pressure observed is 1.8×10^{-2} atm, slightly higher than that observed in the non-rotating case.

The crossover values for each species for all cases are similar. With increase in rotation speed in the counter-clockwise direction, the leakage of the species through the pre-heating gap decreases slightly (<1%). However, the overall crossover remains the same in each of the case.

Figures 4.4 shows the u-velocities in the pre-cooling and pre-heating gap as a function of y position for all cases. The maximum linear velocity of the ceria ring due to rotation is 0.01 m/s in the direction of the rotation. Compared to the flow velocities observed in the pre-cooling gap, this velocity is negligible and hence, the velocity profiles coincide in figure 4.4a. The rotation of the ring causes a greater effect in pre-heating gap due to the lower velocities observed. Since the flow direction and direction of rotation are opposite to each other in pre-heating gap, the net u-velocities decrease with increase in rotation speed.

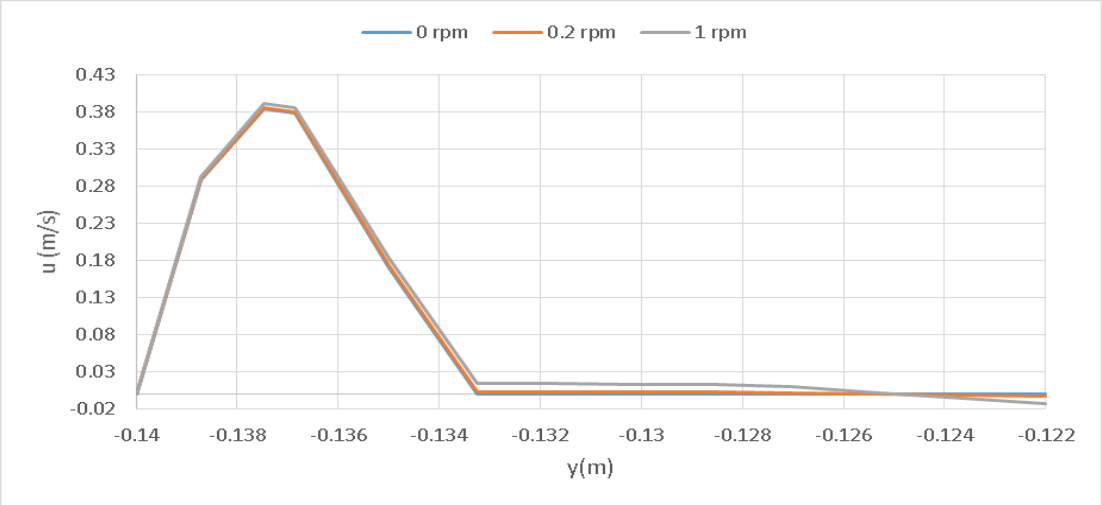

(a)

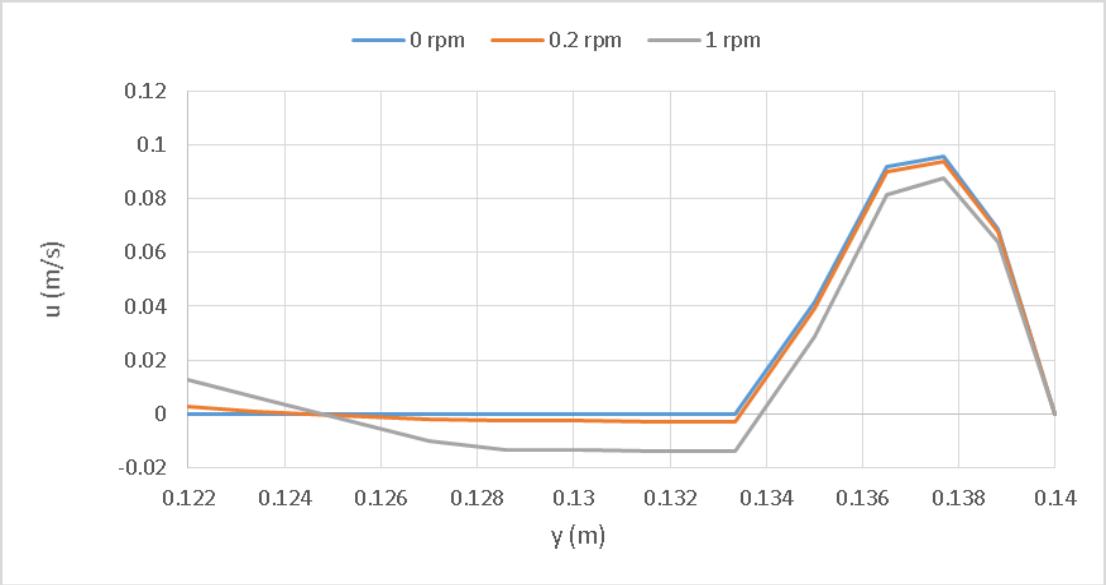

(b)

Figure 4.4: u-velocity as a function of position at (a) ϕ=270°, (b) ϕ=90°

4.5 Conclusions

The reactor model with rotating ceria ring is simulated for non-rotating case, rotation with speeds 0.2 rpm, 1 rpm. The streamlines, concentration plots, crossover values for each species were observed. For all three cases, there were negligible changes in all these plots. The u-velocity plots for all these cases indicate the similarity in the crossover values. Thus, it can be concluded that the rotation of the ceria ring up to 1 rpm doesn't affect the fluid flow field. However, the rotation of the ceria ring changes the ceria throughput which certainly affects the reduction and oxidation reactions. The current reactor model without chemical modeling is out of the scope to provide any insights related to the efficiency of the reduction and oxidation reactions with changes in rotation speeds.

5.0 Effect of varying mass flow rates of incoming gases

5.1 Introduction

Until this chapter, all the simulations are carried out using fixed amounts of incoming gases. The design of the inlet/outlet geometry is carried out with 170:1 ratio of N_2 to O_2 (170x) and 5:1 ratio of CO_2 to CO (5x). In this chapter, the mass flow rates of the incoming gases are varied and the fluid flow field within the reactor examined. The amount of sweeping gas and the oxidizer affects the efficiency of the reactor by altering the heating requirements of the gases and/or by changing the fuel output of the reactor. The mass flow rates of the sweep gas is changed and its effect on the flow field within the reactor is observed with the mass flow rate of the oxidizer held constant. Similarly, the oxidizer flow rate is varied with the sweep gas flow rate held constant and the observations are noted. The reactor can also be used with H_2O as the oxidizer instead of CO_2. Hence, in one of the study, the oxidizer is changed from CO_2 to H_2O and the resulting differences are observed for the same molar flow rate of oxidizer. These set of simulations are carried out in 3D and so, any 3D effects are also noted.

5.2 Methodology

The 3D reactor model with porous ceria ring described previously is utilized for this study. The simulations in 3D are time-consuming and resource-exhaustive. Hence, the comparisons are restricted to two values of mass flow rates for the sweep gas and the oxidizer, respectively. The reactor model is tested with two different flow rates of N_2 - 170x, 100x and two different flow rates of CO_2 - 5x, 10x. The 3D model provides

additional crossover gap at the top and the bottom of the reactor as shown in figure 5.1b. The 3D model includes gravity in the –z direction. In the final simulation, the oxidizer is changed from CO_2 to H_2O and the differences are studied.

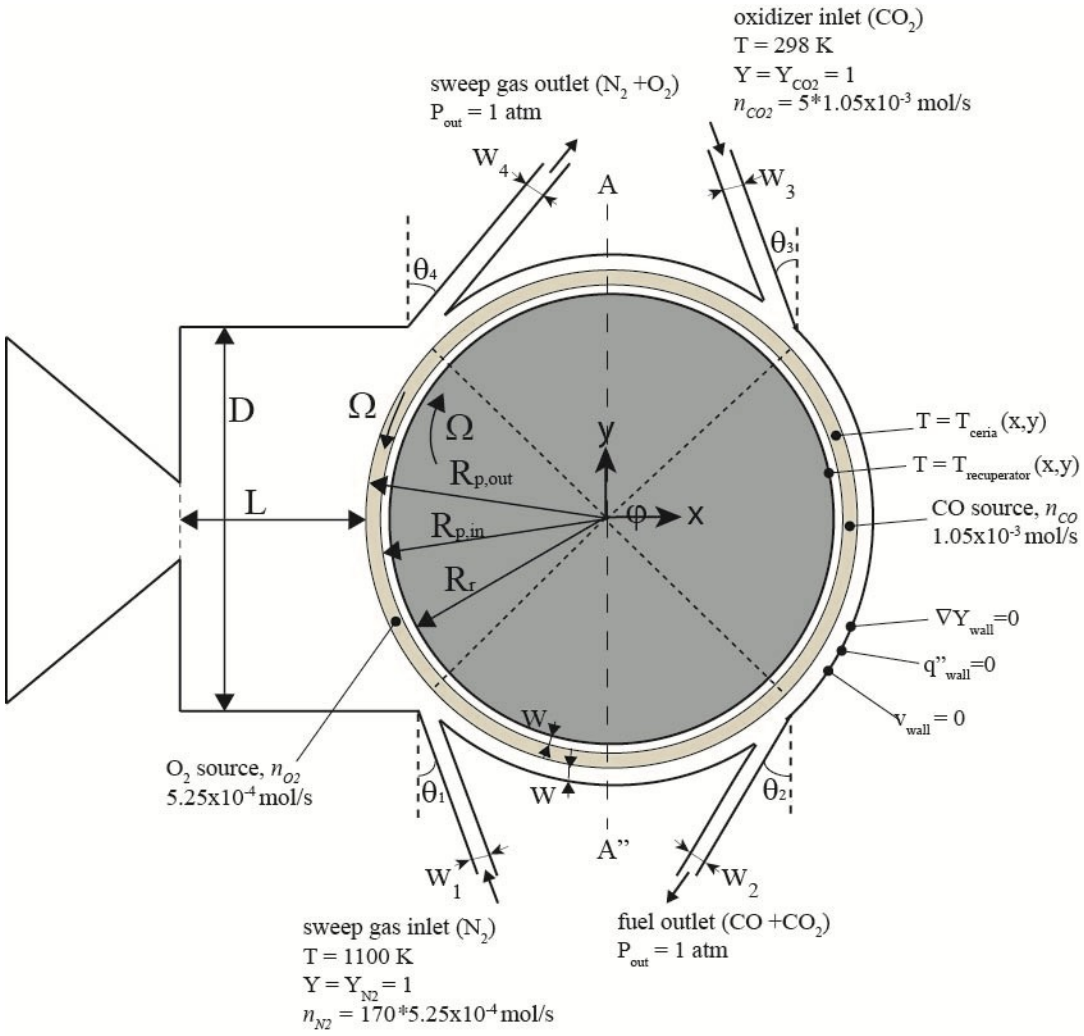

Figure 5.1a: 3D reactor model with rotating ceria ring

All the governing equations mentioned previously apply for the 3D model. The concentration plots are plotted along the height at different locations within the oxidation and reduction zones. The velocity plots are also plotted at different locations within the reactor. The different results are also compared with the case with no gravity.

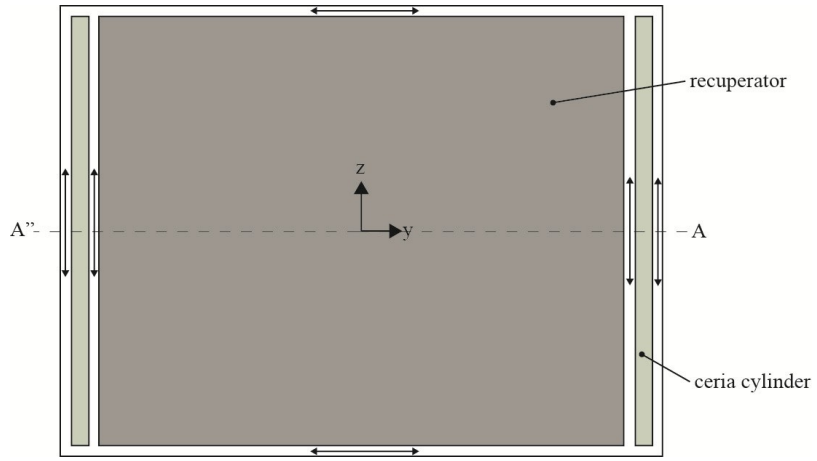

Figure 5.1b: Side view of the 3D reactor with crossover paths

5.3 Results

Different mass flow rates of N_2

The reactor is tested with 2 different mass flow rates of N_2 - 100x, 170x. The flow rate of CO_2 is fixed at 5x. For these two cases, the O_2 partial pressure is observed in the reduction zone at r=0.135m at ϕ = 225°, 180°, 135° along the height of the reactor with and without gravity.

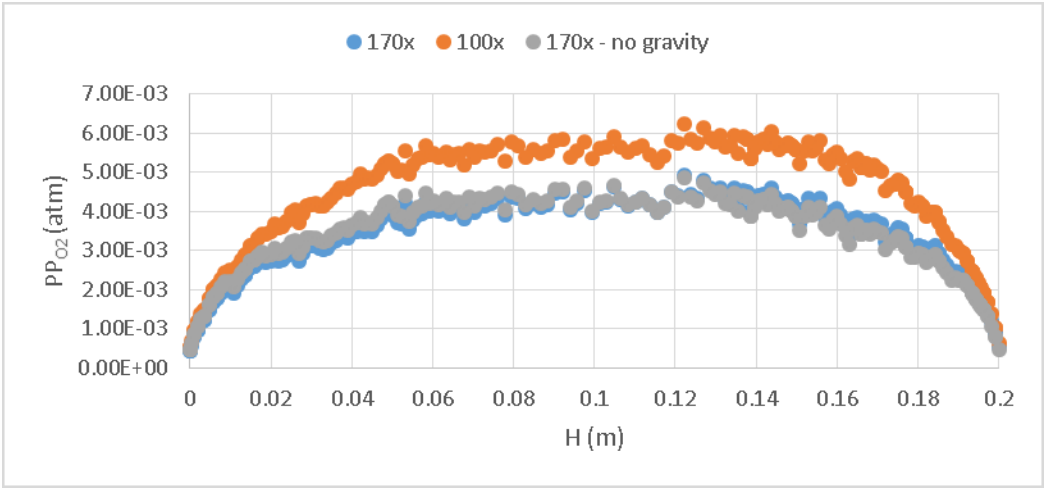

(a)

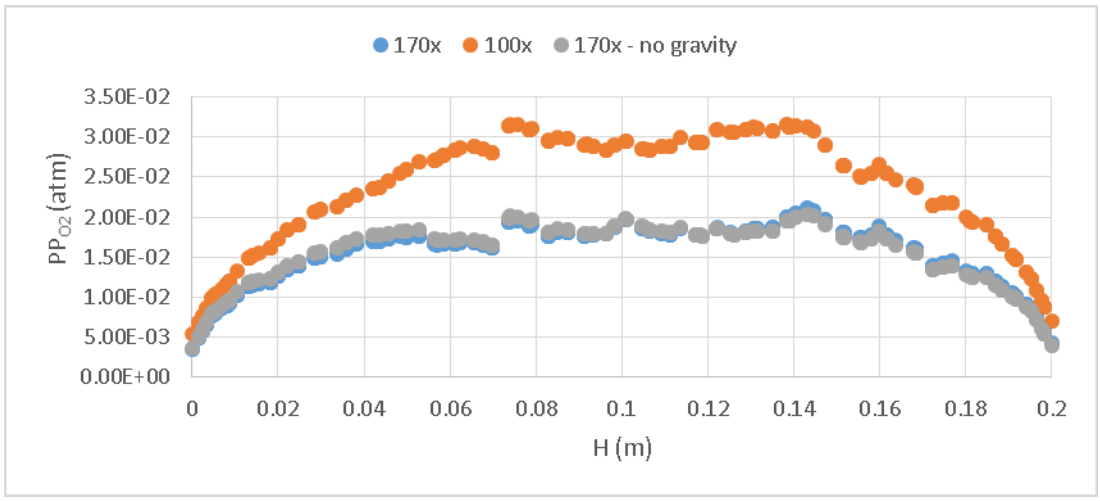

(b)

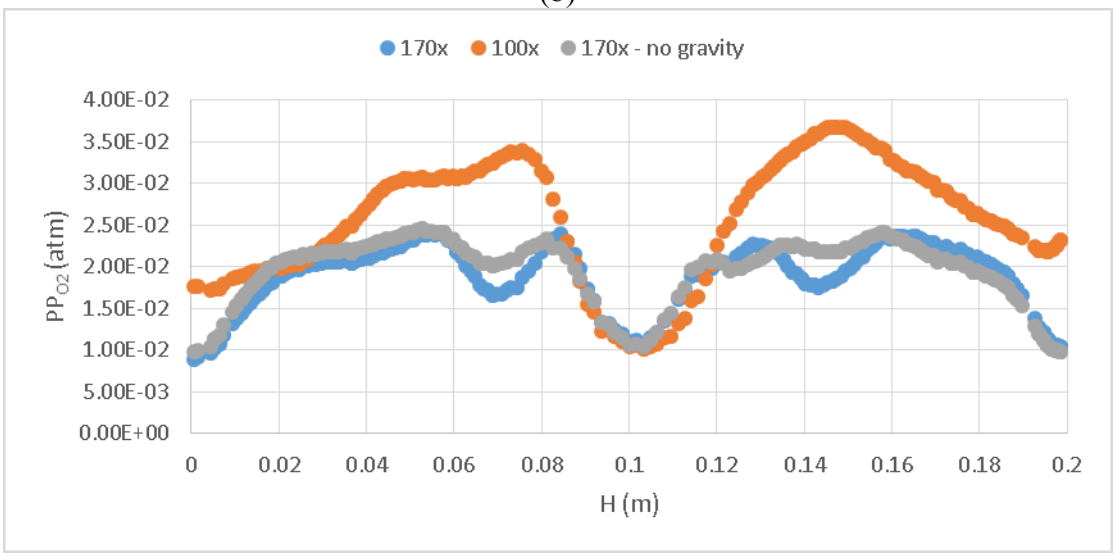

(c)

Figure 5.2: O_2 partial pressure (atm) along the height (m) at r=0.135 m at a) 225°, b)180°, c)135°

Figure 5.2 shows the variation of O_2 partial pressure along the height of the reactor. The O_2 partial pressure is highest at the middle and tapers off at the top and the bottom of the reactor. The O_2 partial pressure is higher for the 100x case than the 170x case for all the locations. The O_2 partial pressure progressively increases along the reduction zone from the N_2 inlet to the N_2 outlet. The case with no gravity shows no significant difference from the case with gravity. The O_2 partial pressure averaged over

the height at these locations are plotted in figure 5.3 for the different mass flow rates of N_2.

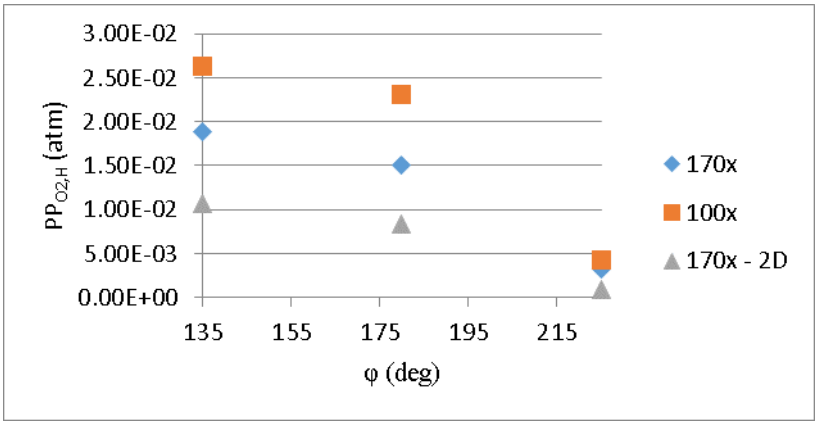

Figure 5.3: Height-averaged O_2 partial pressure (atm) along the reduction zone angle (ϕ)

The difference between O_2 partial pressures for the two cases is the least at the N_2 inlet - $1x10^{-3}$ atm. This difference increases to $8x10^{-3}$ atm at other locations. This difference constitutes $\Delta\delta = 0.002$ at the maximum (Appendix D). The extra heating required for the increased flow rate of N_2 $\left(\Delta\dot{n}_{N_2} \cdot \left(h(T_{1100}) - h(T_{300})\right)\right)$ far outweighs the small increase in fuel output $[\Delta\delta \cdot \dot{n}_{ceria} \cdot HHV_{fuel}]$ possible with the $\Delta\delta$ of 0.002. Hence, flow rate of N_2 should be restricted to 100x or lesser.

The plot also shows the average O_2 partial pressure (along the height) for 170x case in 3D model with the O_2 partial pressure for 170x case in 2D model. Again the difference is $8x10^{-3}$ atm except at the N_2 inlet. The average values from the 3D model is almost 50% higher than the corresponding values from the 2D model.

Mass flow rates of N_2	Crossover values (%)			
	N_2	O_2	CO	CO_2
170x	10	6	0	8
100x	8	2	2	26

Table 5.1: Crossover values (%) for different mass flow rates of N_2

The crossover table gives the leakage values of each species for two different mass flow rates of N_2. The main difference is the drastic increase in the crossover values of CO_2 from 8% to 26%. There is slight decrease in N_2, O_2 crossover. The increase in CO_2 is through pre-heating gap, while reduction in N_2, O_2 crossover is mainly via pre-cooling gap. Thus, for 100x case, the net reduction in fuel output due to combined CO and O_2 crossover leads to 4% whereas, for 170x case, the net fuel reduction is 6%. Based on the crossover values, lower mass flow rate of N_2 is desirable.

The u-velocities at pre-heating gap (90°), pre-cooling gap (270°) at r=0.135 are shown in figure 5.4. These figures are representative of the u-velocities in the gaps. It can be seen that net flow rate in pre-cooling gap is from reduction side to oxidation side, while it is the reverse in the pre-heating gap. In the pre-cooling gap, the mean u-velocity decreases for 100x compared to 170x, indicating decreased crossover for 100x case. The maximum u-velocity (0.07 m/s) in the negative direction occurs close to the bottom of the reactor. This is entirely composed of oxidizer as seen from figure 5.5c. While the flow in the pre-cooling gap is entirely composed of N_2 and O_2 for both cases, all the species are present in the pre-heating gap. Figure 5.5 shows the variation of species concentration in the pre-heating gap.

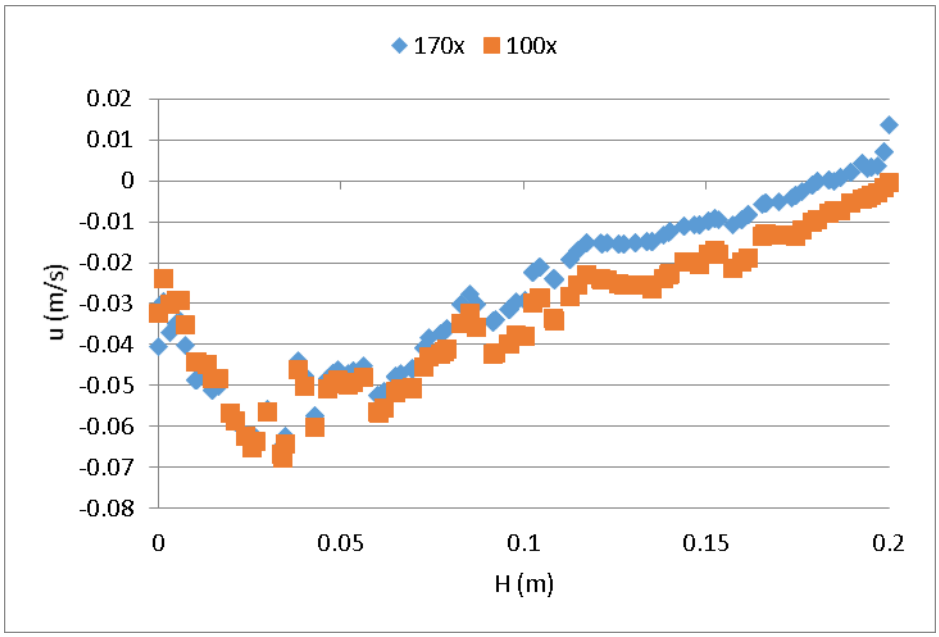

(a)

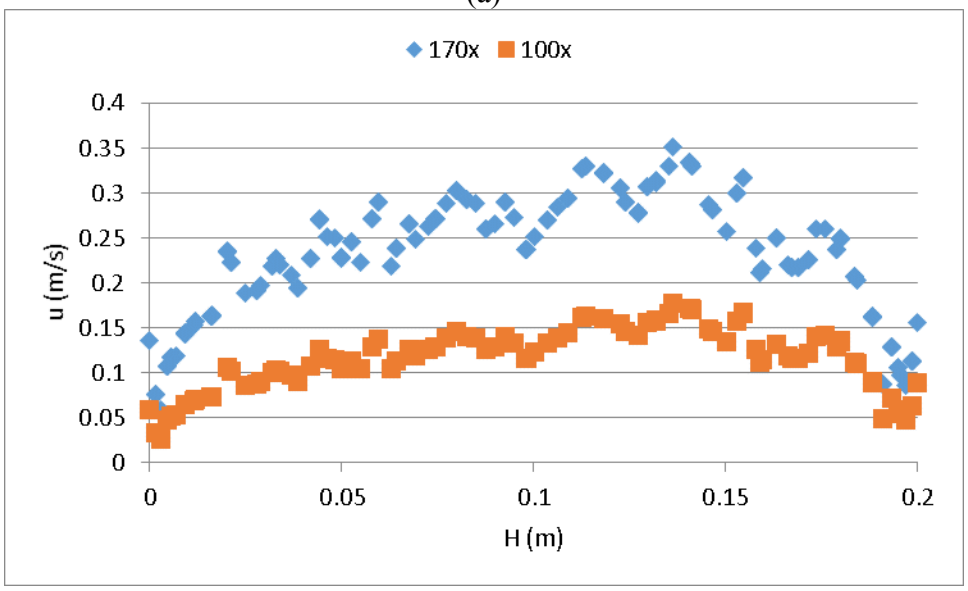

(b)

Figure 5.4 : u-velocities at r=0.135 m at a) pre-heating gap (90°), b) pre-cooling gap (270°)

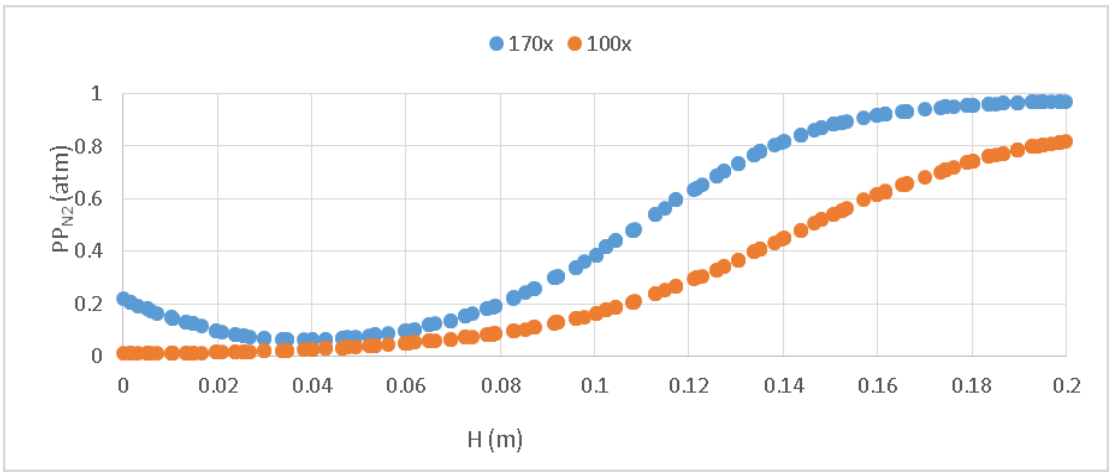
170x
100x
1
0.8
0.6
0.4
0.2
0
PP$_{N2}$ (atm)
0
0.02
0.04
0.06
0.08
0.1
0.12
0.14
0.16
0.18
0.2
H (m)

(a)

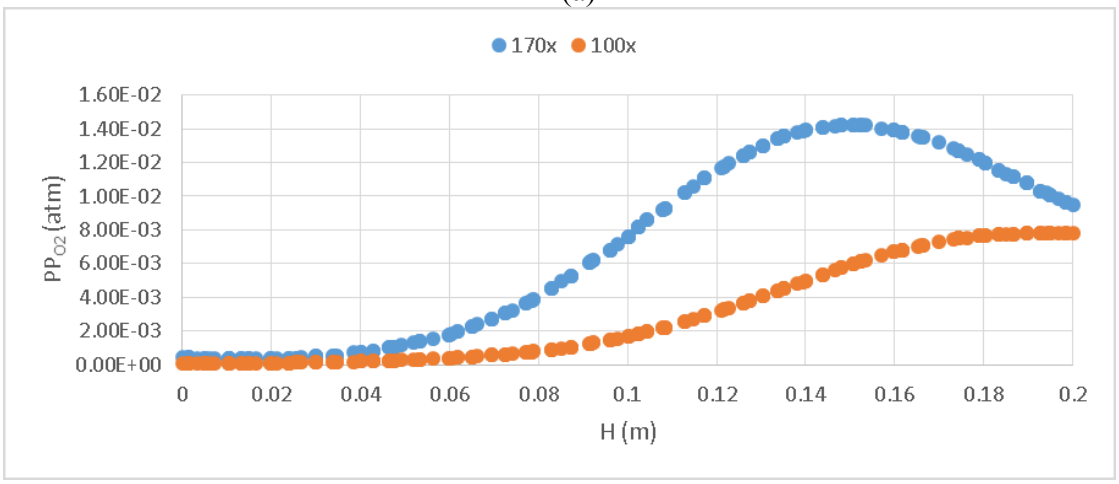
170x
100x
1.60E-02
1.40E-02
1.20E-02
1.00E-02
8.00E-03
6.00E-03
4.00E-03
2.00E-03
0.00E+00
PP$_{O2}$ (atm)
0
0.02
0.04
0.06
0.08
0.1
0.12
0.14
0.16
0.18
0.2
H (m)

(b)

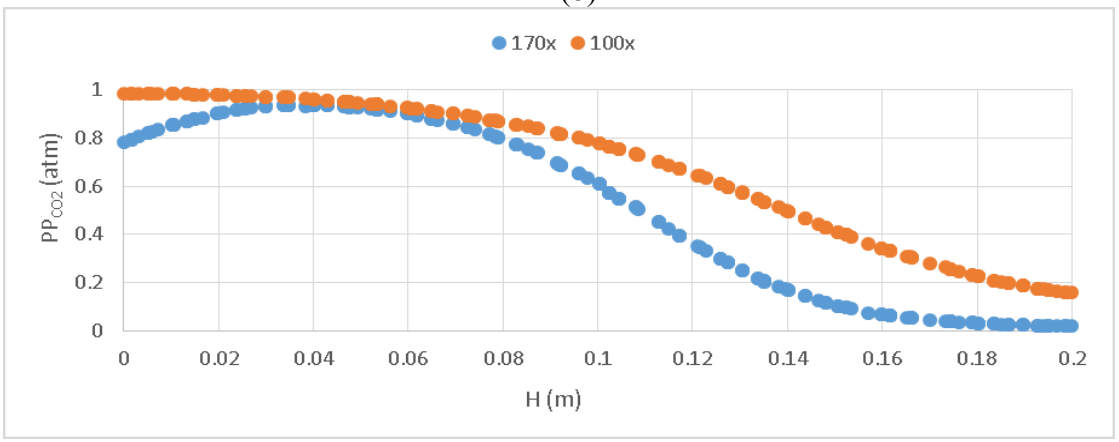
170x
100x
1
0.8
0.6
0.4
0.2
0
PP$_{CO2}$ (atm)
0
0.02
0.04
0.06
0.08
0.1
0.12
0.14
0.16
0.18
0.2
H (m)

(c)

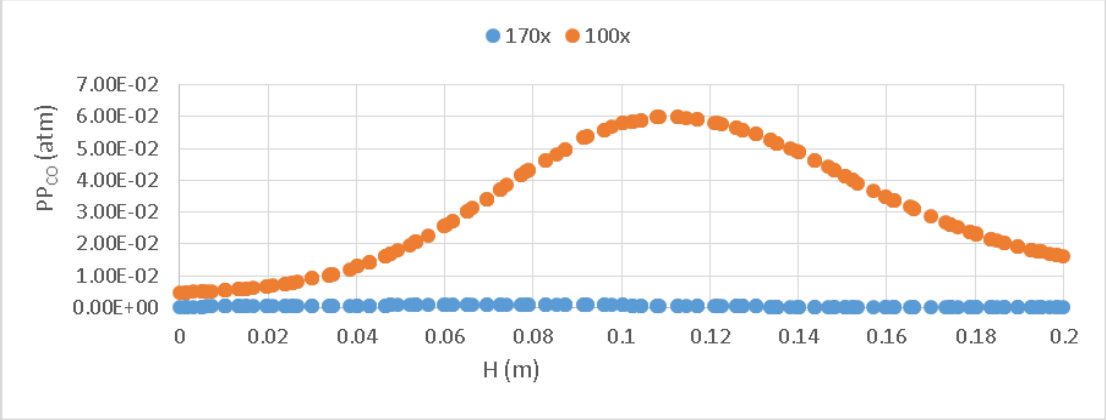

(d)

Figure 5.5: Partial pressure plots at r=0.135 m, ϕ=90° of (a) N_2, (b) O_2, (c) CO_2, (d) CO

Figure 5.5 shows the partial pressure variation of each species along the height of the reactor at r=0.135 m and ϕ=90° for two different mass flow rates of N_2 - 170x (blue), 100x (red). N_2, O_2 concentration is higher at the top of the reactor and almost zero at the bottom of the reactor. In contrast, the CO_2 concentration is higher at the bottom of the reactor for both cases. From the N_2, O_2 plots, it is clear that their partial pressure is higher for the 170x case. This indicates for 170x case, the crossover of N_2, O_2 via pre-heating gap increases. From the plots, it is clear that the leakage of N_2, O_2 occurs mainly in the upper part of the reactor. In contrast, from the CO_2 plot, it is clear that the CO_2 concentration increases with decrease in mass flow rate of N_2. Thus, CO_2 leakage via pre-heating gap increases with the decrease in mass flow rate of sweep gas, as shown in the crossover table 5.1. For 170x, CO concentration is almost zero, for 100x, the CO partial pressure peaks to 0.06 atm indicating a slight leakage via pre-heating gap. Presence of CO_2 only at the bottom and pre-heating zones is clearly illustrated by the velocity vectors colored by N_2 at the top and the bottom of the reactor in figure 5.6.

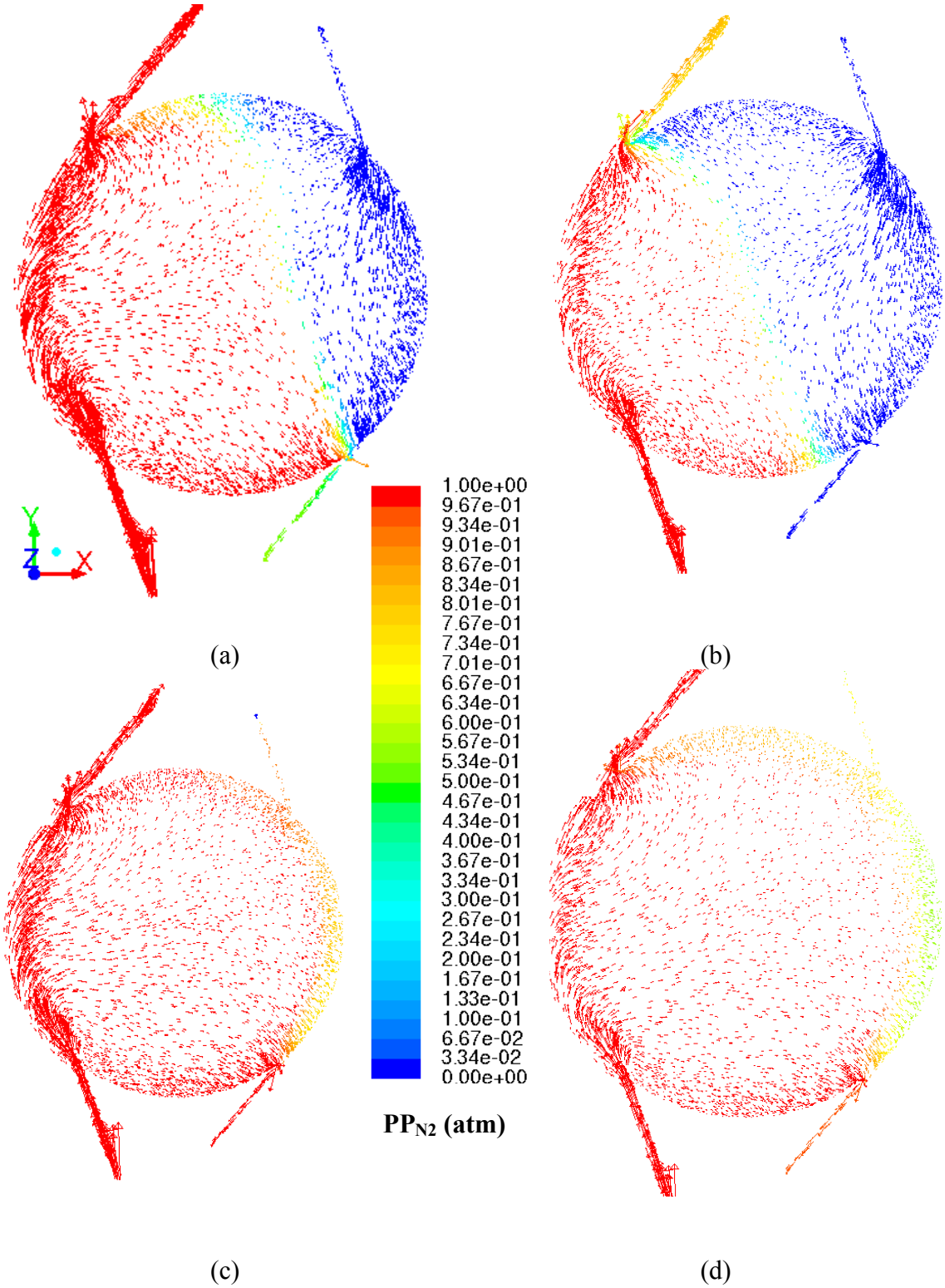

Figure 5.6: N_2 colored velocity vectors at a) z=0.004 m, 170x, b) z=0.004 m, 100x c) z=0.204m, 170x, d) z=0.204m, 100x

In figure 5.6, the red vectors represent N_2 (P_{N2}=1 atm), while dark blue vectors indicate the presence of CO_2. From the figure 5.6, it is clear that N_2 spreads completely over the top part of the reactor for both cases. For the bottom part, the spread of N_2 depends on its mass flow rate. However, for both cases, CO_2 is present only in the pre-heating region. This is true for the entire height of the reactor. It is clear from figure 5.6 b, c that the N_2 crosses over the top of the reactor to the oxidation zone. Figure 5.7 shows the representative partial pressure of N_2 as a function of the height of the reactor at one location within the oxidation zone. Until z=0.1m, the N_2 partial pressure is almost similar for both cases and is less than 0.1 atm. However, above the halfway mark, the differences become clear and N_2 partial pressure is higher for 170x case.

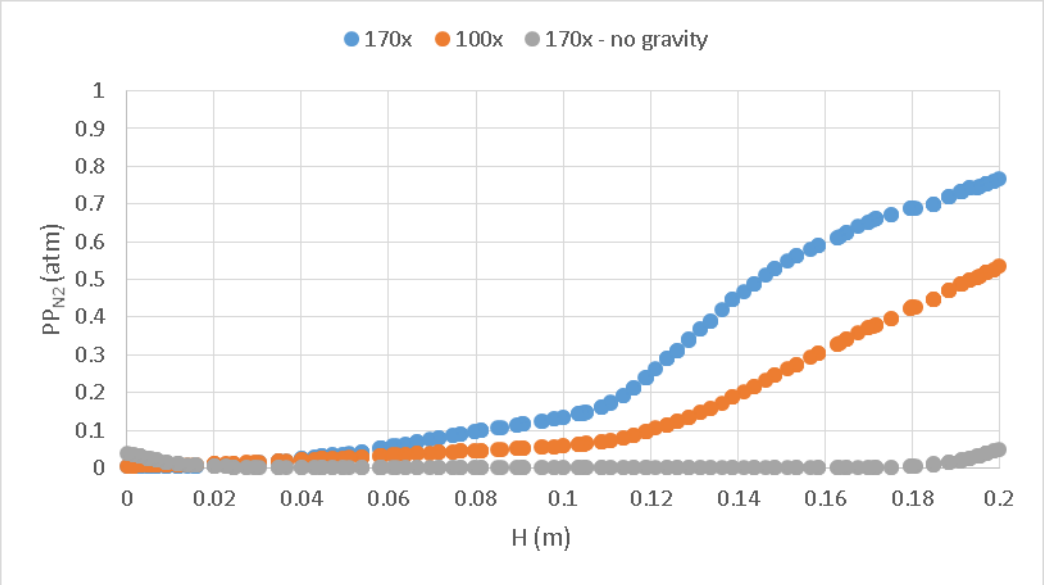

Figure 5.7: N_2 partial pressure in the oxidation zone at r=0.135 m, ϕ=0°

Figure 5.8 shows the w-velocity at r=0.135m at ϕ=45° for 170x case. The z component of the velocity is slightly negative at the top and the bottom of the reactor. The negative w-velocity at the top indicates the downward velocity of N_2 stream flowing from the

reduction side, while at the bottom, it represents the CO_2 flowing towards the bottom of the reactor.

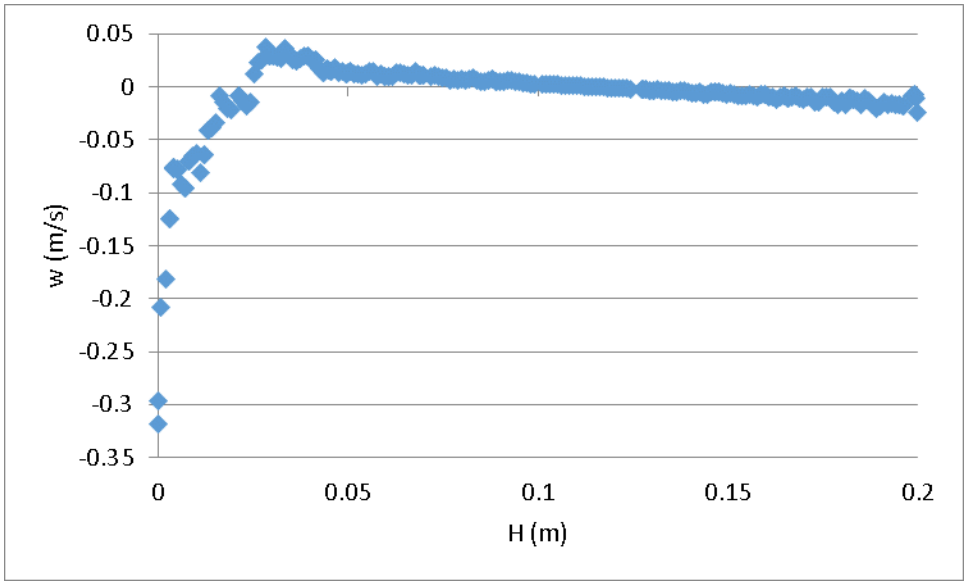

Figure 5.8: w-velocity along height at r=0.135 m at ϕ=45°

Different flow rates of CO_2

Similar to the previous section, the mass flow rate of CO_2 is set to two values - 5x, 10x, 5 and 10 times the stoichiometric value and the observations are noted. The N_2 mass flow rate is fixed to 170x for these cases. The CO_2 partial pressure is observed at r=0.135 at different locations ϕ=45°, 0°, 315° along the height of the reactor in figure 5.9. ϕ=45° represents the oxidation zone closer to the CO_2 inlet, ϕ=315° represents the oxidation zone at the CO_2 outlet. It is clear from the figure that CO_2 concentration for both cases is close to 1atm at the bottom of the reactor The general trend is the CO_2 partial pressure decreases along the height of the reactor. The CO_2 partial pressure is higher for higher mass flow rate of CO_2. For all three locations, the CO_2 partial pressure decreases to a low value towards the top part of the reactor due to the crossing over of N_2.

For the top quarter of the reactor, the CO_2 concentration decreases below 0.1 atm for 5x case.

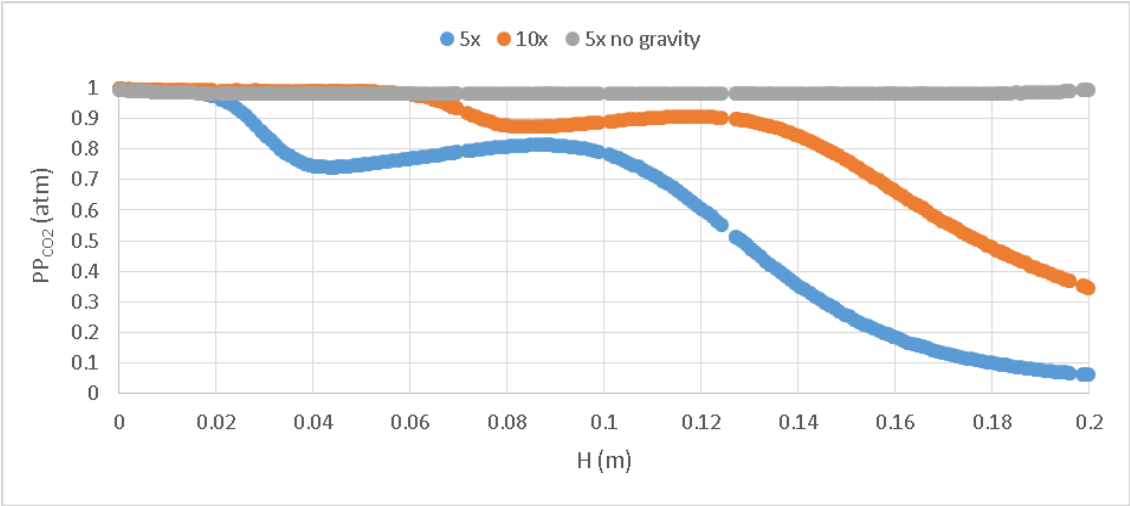

(a)

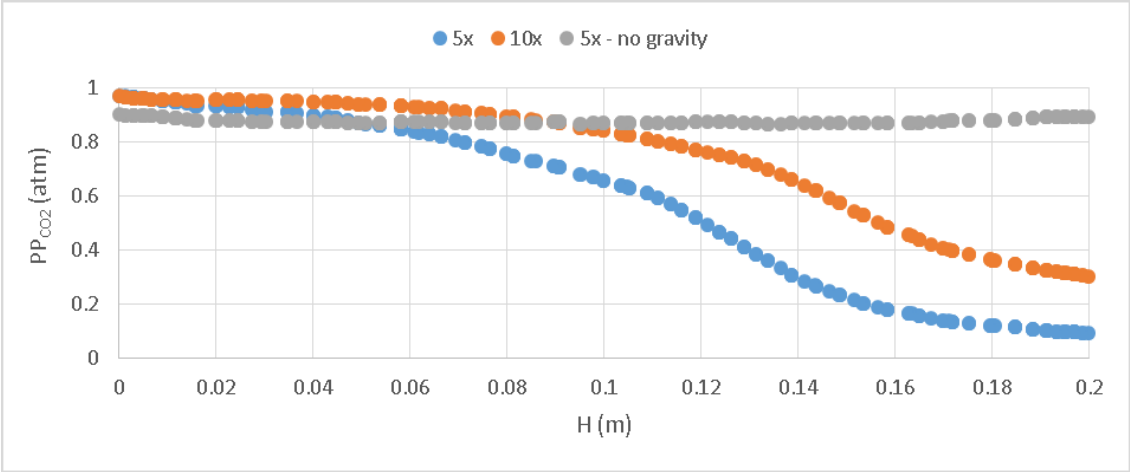

(b)

Some of the CO_2 flows through the bottom and the pre-heating region of the reactor and exits through the N_2 outlet. Unlike N_2, changes in mass flow rates of CO_2 do not affect the flow field within the reduction zone and the pre-cooling zone of the reactor. Unlike N_2, the variation of CO_2 concentration along the height is different with and without gravity.

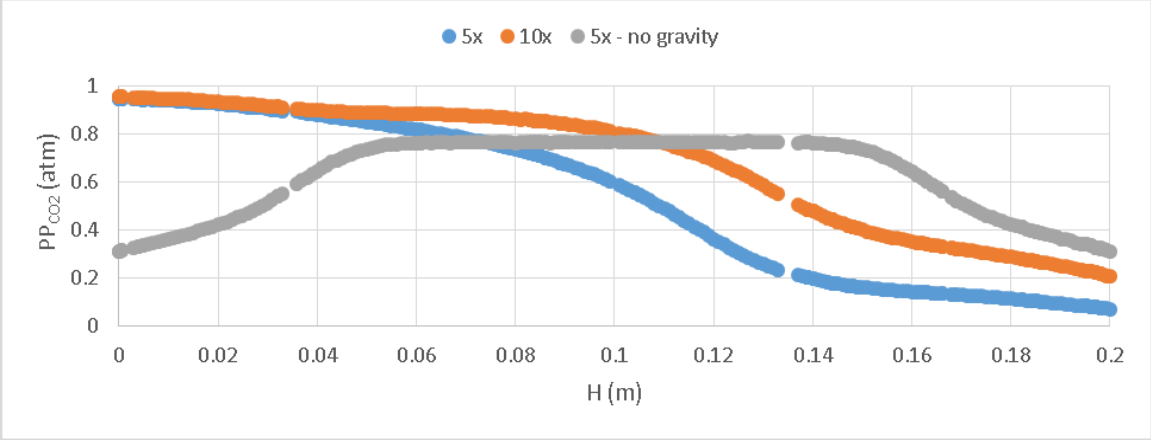

(c)

Figure 5.9: CO_2 partial pressure (atm) along the height (m) in the oxidation zone at (a) ϕ=45°, (b) ϕ=0°, (c) ϕ=315°

Mass flow rates of CO_2	Crossover values (%)			
	N_2	O_2	CO	CO_2
5x	10	6	0	8
10x	8	4	0	21

Table 5.2: Crossover values (%) for different mass flow rates of CO_2

Table 5.2 gives the crossover values of each species for two different flow rates of oxidizer. The leakage of CO_2 via pre-heating gap increases with increase in mass flow rate of CO_2. The crossover values increase from 8% to 21% when the CO_2 flow rate is doubled. This increase causes slight reduction in leakage of N_2 and O_2.

The non-uniform spreading of CO_2 along the height of the reactor can be explained by two ways. The first way is by using a non-dimensionless number called Richardson number. Richardson number is mostly used to analyze stability in atmospheric air currents [31]. In its most basic form, Richardson number is defined as the

ratio of potential to kinetic energy of the species. If the number is significantly higher than unity, then the kinetic energy of the species is not enough to homogenize the fluids.

$$\mathrm{Ri} = \frac{gH}{U^2}$$

Figure 5.10 shows the variation of CO_2 partial pressure along the height for different Richardson number at ϕ=45°. Ri = 0 represents the case with no gravity, Ri = 31 represents the case with 10 times the stoichiometric amount of CO_2 input, while Ri = 125 belongs to the case with 5 times the stoichiometric amount of CO_2 input. Without gravity, the Richardson number is zero regardless of the speed of the incoming gas. Without gravity, CO_2 partial pressure is uniform along the height of the reactor. This holds true at every location within the oxidation zone. For the cases with gravity, higher mass flow rates of CO_2 or lower Richardson number leads to better spread (more uniform) of CO_2 along the height.

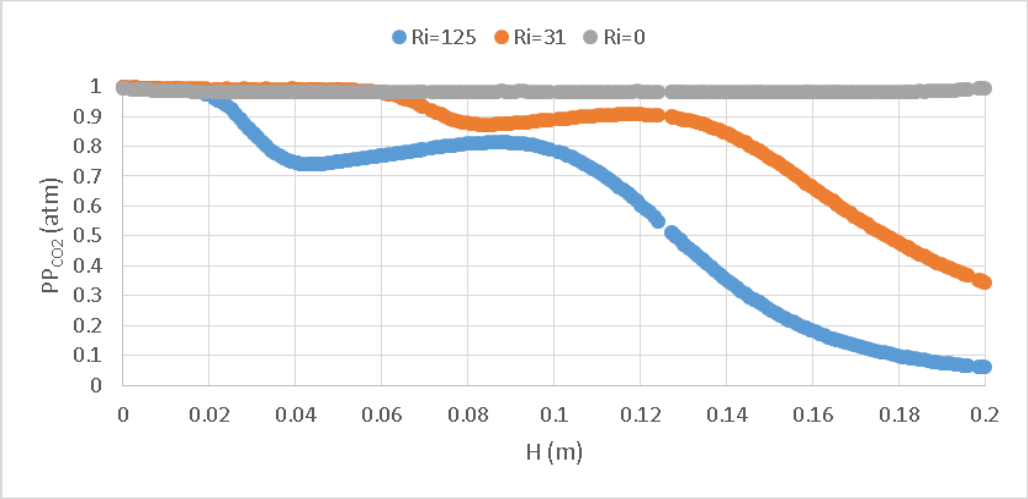

Figure 5.10: CO_2 partial pressure (atm) as a function of height (m) for different Ri at r=0.135 m, ϕ=45°

Second way to explain the non-uniform distribution of CO_2 along the height of the reactor is using the buoyancy effect. It should be noted that CO_2 is 1.5 times heavier

than N_2 and N_2 is 1.5 times heavier than H_2O. Therefore, H_2O should spread more uniformly compared to CO_2 in a N_2 environment. Figure 5.11 shows the plot of the variation of partial pressure along the height of the reactor for same Richardson number (Ri=125) for CO_2 and H_2O. Note that for CO_2, Ri of 125 represents 5 times the stoichiometric value, while for H_2O it represents 3.6 times the stoichiometric value. From figure 5.10, it is clear that for the same Ri, H_2O spreads more uniformly along the height of the reactor as compared to CO_2 in similar N_2 environment.

In figure 5.12, the variation of partial pressure of the oxidizer as a function of height for the same molar flow rate of oxidizer is shown. The molar flow rate is set at 5 times the stoichiometric value. The N_2 molar flow rate is also kept constant. For same molar flow rates of oxidizer, the spread of H_2O is higher than CO_2. From figures 5.11, 5.12, it is evident that the spread of H_2O is more uniform not only because of its higher velocity, but also due to its lighter density compared to CO_2 (and N_2).

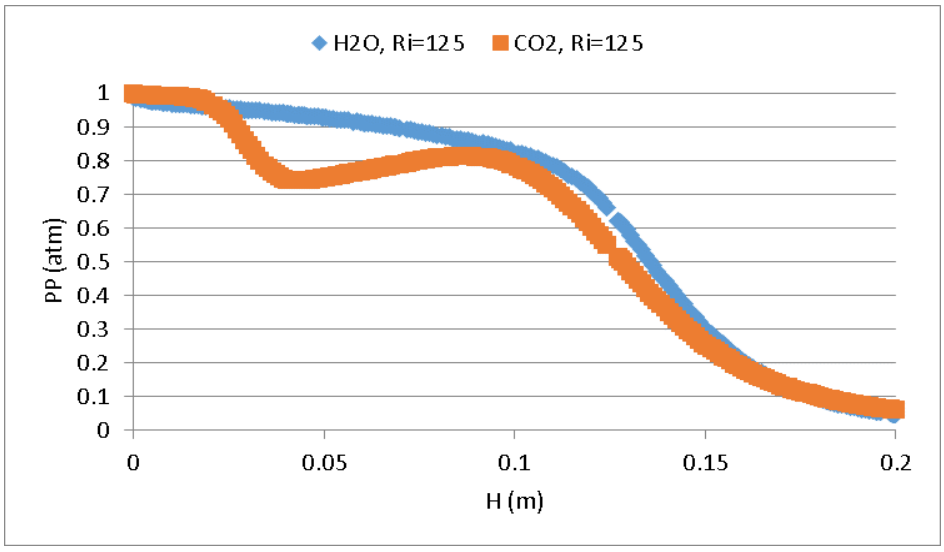

Figure 5.11: Partial pressure of the oxidizers (atm) as a function of height (m) for Ri = 125 at r=0.135 m, ϕ=45°

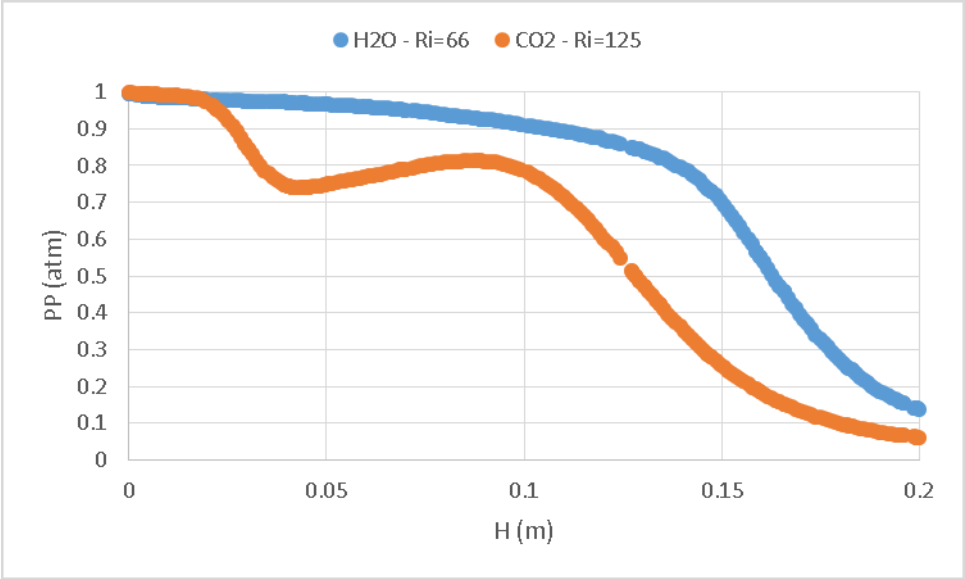

Figure 5.12: Partial pressure of the oxidizers (atm) as a function of height (m) at r=0.135 m ϕ=45°

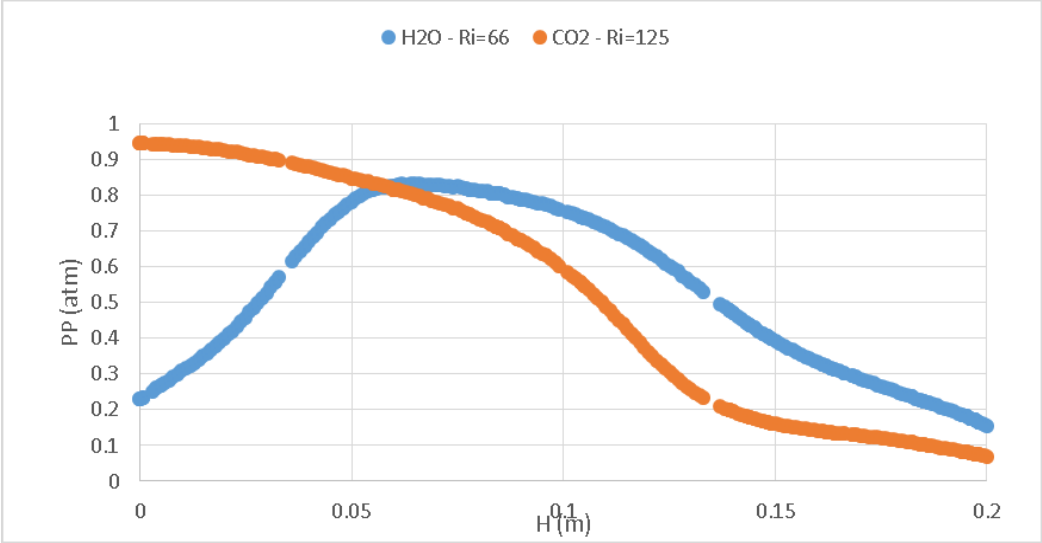

Figure 5.13: Partial pressure of the oxidizers (atm) as a function of height (m) at r=0.135 m ϕ=315°

Figure 5.13 shows the partial pressure plot at the CO_2 outlet (ϕ=315°). It can be seen from the figure that, at the top of the reactor, the concentration of H_2O is higher than CO_2. In contrast, at the bottom, CO_2 has a higher concentration compared to H_2O. This is because in the case with H_2O, N_2 displaces H_2O from the bottom and settles there since N_2 is heavier compared to H_2O.

5.4 Conclusions

The reactor model is tested with two different flow rates of N_2 - 170x, 100x, while keeping the oxidizer flow rate fixed at 5x. The net flow for both cases at the top and the pre-cooling zone is from reduction to oxidation side and consists of N_2 and O_2. The net flow in the pre-heating zone is from oxidation to reduction side and consists of all species. Lighter N_2, O_2, CO have higher concentration towards the top, while the heavier CO_2 settles at the bottom of the reactor. The decrease in O_2 partial pressure in the reduction zone for the 170x compared to the 100x is not sufficient to warrant flowing 70 times more N_2. This conclusion can be also reached based on the crossover numbers. The lower mass flow rates of N_2 (100x) lead to 4% reduction in fuel, whereas higher mass flow (170x) rate leads to 6% reduction. The amount of sweep gas affects the species concentration in the oxidation zone. However, the reduction zone remains unaffected by CO_2 flow. The reactor model is also simulated with two different flow rates of CO_2 - 5x, 10x. Since CO_2 is appreciably heavier than other species within the reactor, it settles towards the bottom of the reactor. The current study without the chemical modeling is unable to provide a suitable number for the mass flow rate of oxidizer. The concentration of CO_2 in the oxidation zone required for suitably greater oxidation reaction extent will ultimately determine the mass flow rate of oxidizer. Based on the study, it is found that concentration of oxidizer decreases towards the top of the reactor and should be the region of interest for further observation. It is further noted that the mass flow rate of the oxidizer five times the stoichiometric value is at least required so as not to cause the top quarter of the reactor devoid of oxidizer.

6.0 Effect of inlet/outlet configurations in 3D

6.1 Objective

The 3D model of the reactor, discussed in the previous chapter, involved slots for the inlets and outlets of the reactor. In modeling of the slots, uniform concentration of the incoming gas is assumed along the height of the reactor. Circular ports provide a much easier connection access with the external gas systems compared to the slot configuration. Hence, in this chapter, 3D reactor models with circular ports for inlets and outlets are studied. The slots are replaced by discrete number of circular holes of equal cross-sectional area in the 3D reactor model. The fluid flow field and the concentration of different species along the height is observed for different inlet/outlet configurations and compared with the slot configuration.

6.2 Methodology

In this study, the 3D simulation is carried out for the base case for four different configurations – slot inlet/outlet, single inlet/outlet, 2 inlets/outlets and 3 inlets/outlets for both N_2 and CO_2. For each case, the mass flow rate of N_2 is set to 2.5×10^{-3} kg/s (170x) and a higher mass flow rate of CO_2 is set to 4.62×10^{-4} kg/s (10x). The angular and circumferential positions of the inlets and outlets are same as in the base case slot geometry. The sum of the cross-sectional areas of the inlets/outlets is kept constant in each case and is equal to the cross-sectional area of the slot. The widths of the slots are determined as mentioned in chapter 2. The positioning of the inlet/outlet configurations along the height of the reactor is shown in figure 6.1.

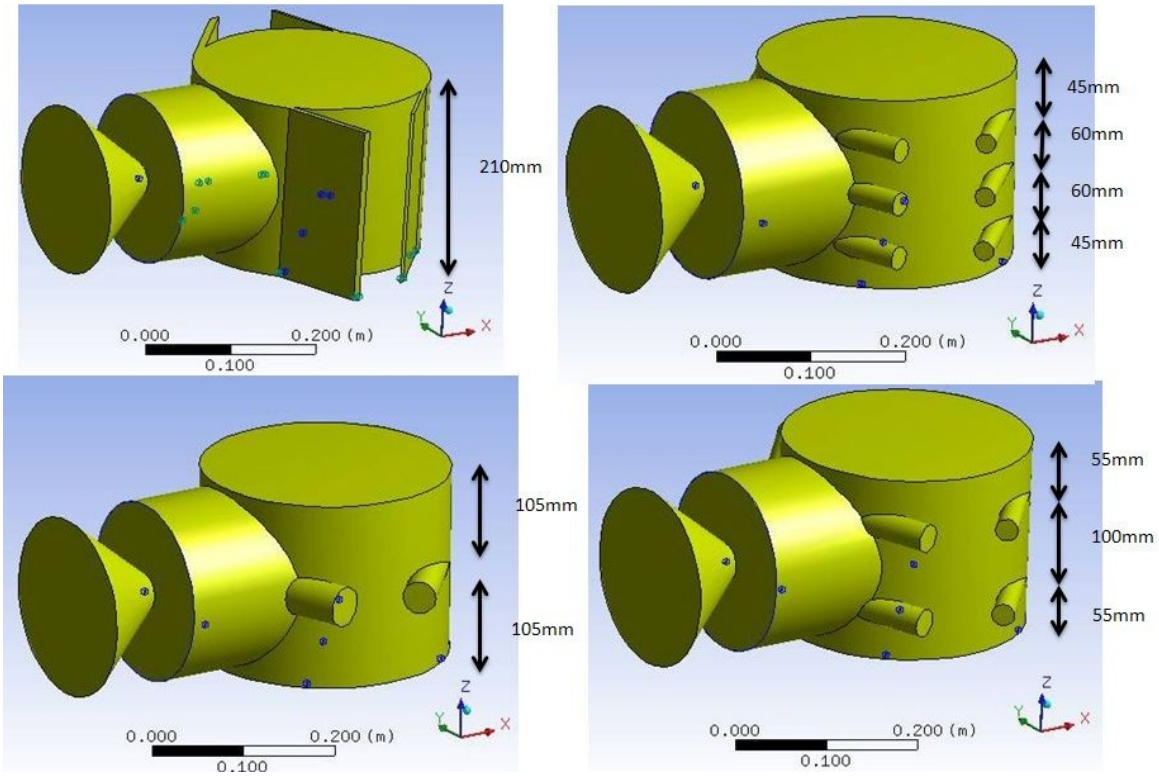

Figure 6.1: Different inlet/outlet configurations of the reactor model

The diameters of the inlets/outlets for the different configurations are shown in table 6.1.

	Diameter of N_2 inlet, d_1 (mm)	Diameter of CO_2 inlet, d_3 (mm)	Diameter of N_2/O_2 outlet, d_4 (mm)	Diameter of CO/CO_2 outlet, d_2 (mm)	Inlet/Outlet placements (m)
1 inlet/outlet	44	36	56	36	0.105
2 inlets/outlets	31	25	40	25	0.055, 0.155
3 inlets/outlets	25	21	32	21	0.045, 0.105, 0.165

Table 6.1: Dimensions of the different inlet/outlet configurations

The distribution of the sweep gas within the reduction zone is studied by observing the variation of N_2 partial pressure along the height of the reactor at different

locations within the reduction zone. The effect of the sweeping gas on the fluid flow field is observed. The effect of the inlet and outlet configuration on the flow in the oxidation zone is observed by looking at the CO_2 partial pressure variation along the height of the reactor at different locations within the oxidation zone. The crossover values for each of these cases are noted and compared. Finally, conclusion is drawn based on these findings regarding the optimum inlet/outlet configuration for the functioning of the reactor.

6.3 Results

Effect of the inlet/outlet configuration on the reduction side

Figure 6.2 shows the variation of N_2 partial pressure along the height of the reactor at different locations within the reduction zone. Figures 6.2a, 6.2b, 6.2c depict the N_2 partial pressure at ϕ=225º, ϕ=180º and ϕ=135º, respectively.

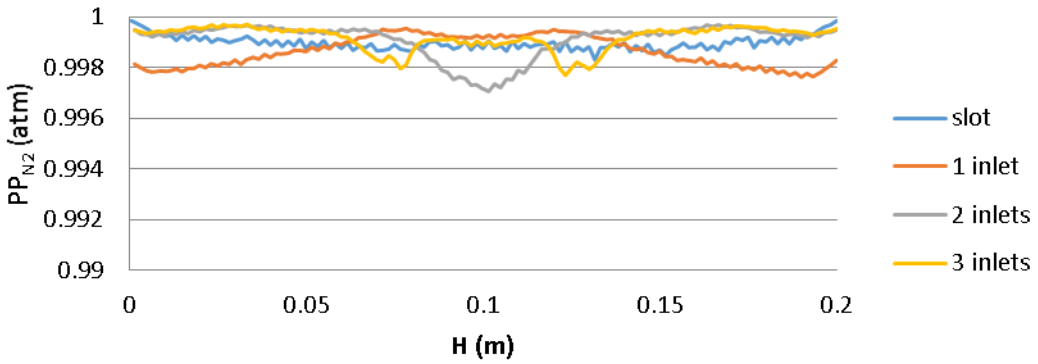

Figure 6.2a: N_2 partial pressure (atm) for different configurations at $\phi = 225^o$

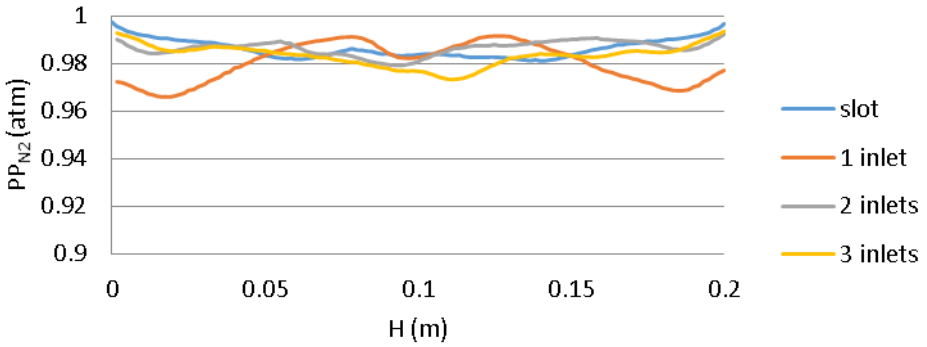

Figure 6.2b: Partial pressure of N_2 (atm) for different configurations at $\phi = 180^o$

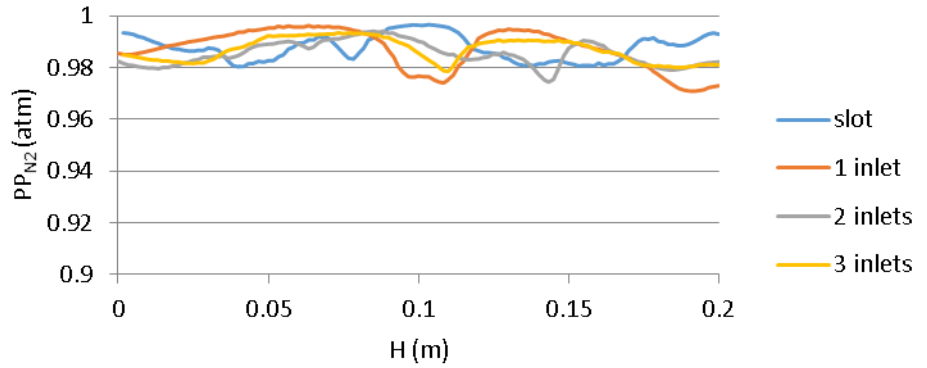

Figure 6.2c: N_2 partial pressure (atm) for different configurations at $\phi = 135^o$

The maximum variation of N_2 partial pressure from the mean value is $3x10^{-2}$ atm at ϕ=135° close to N_2 outlet. At the N_2 inlet, the variation is the least and amounts to $3x10^{-3}$ atm. At the inlet, the N_2 partial pressure increases locally at the location of inlet holes. But this increase is too small to provide advantage to any particular inlet configuration. Similarly, the maximum variation of N_2 partial pressure at the N_2 outlet is too small compared to the average value. Thus, there seems to be negligible effect of the outlet configuration too on the flow field.

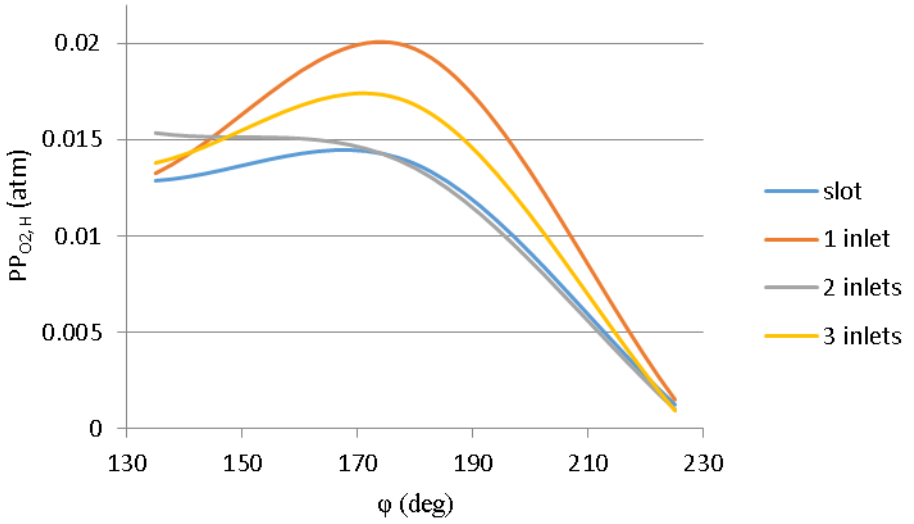

Figure 6.3: z-averaged partial pressure of O_2 (atm) as a function of circumferential angle at r=0.133m

Figure 6.3 shows the height averaged O_2 partial pressure as a function of circumferential angle within the reduction zone. Among the different configurations, the slot configuration results in the least O_2 partial pressure by a minimum of $3x10^{-3}$ atm. 1 inlet configuration has the highest O_2 partial pressure within the reduction zone.

Effect of the inlet/outlet configuration on the oxidation side

Figure 6.4 shows the variation of CO_2 partial pressure along the height of the reactor at different locations within the oxidation zone. Figures 6.4a, 6.4b, 6.4c depict the N_2 partial pressure at ϕ=45º, ϕ=0º and ϕ=315º, respectively. At the CO_2 inlet, the discrete holes configuration provide much better uniform CO_2 concentration than the slot configuration. The CO_2 concentration due to the slots are as explained in the previous chapter. All of the configurations show a sudden dip towards the top of the reactor (z>0.185 m) due to the crossover of N_2 from the top. From figure 6.3b, it is clear that towards the middle of the oxidation zone (ϕ=0º), CO_2 concentration has become more or less uniform for all configurations before dropping sharply at around z=0.15 m. However,

the main difference between the slot and other discrete holes configuration is clearly illustrated in figure 6.3c.

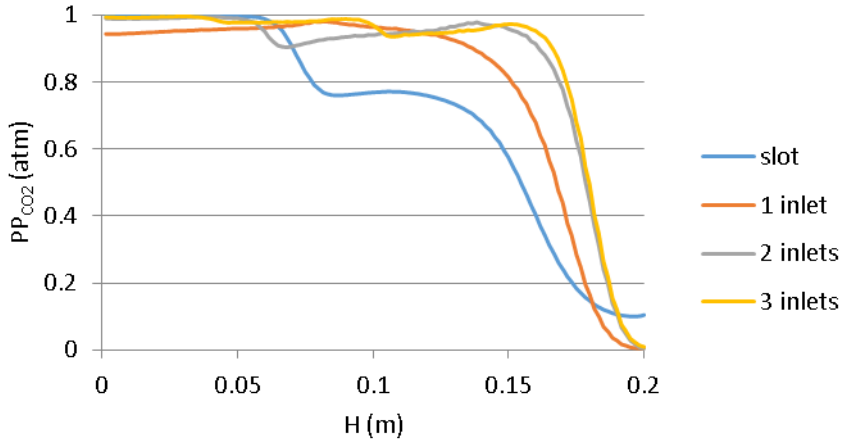

Figure 6.4a: Partial pressure of CO_2 (atm) for different configurations at $\phi = 45^o$

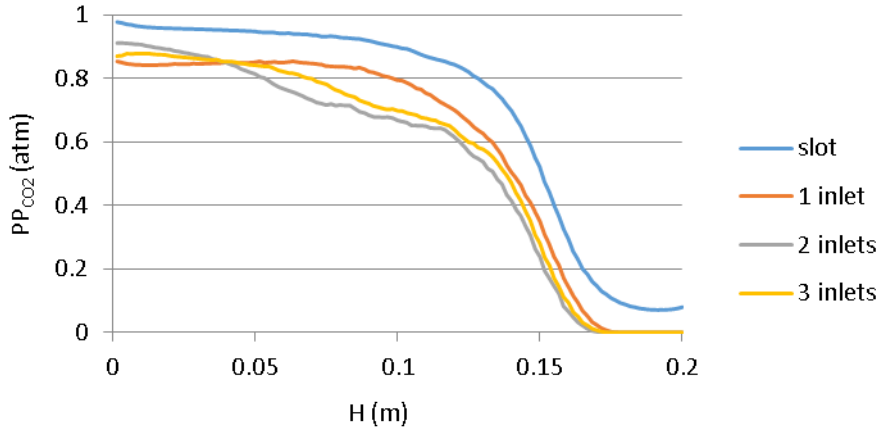

Figure 6.4b: Partial pressure of CO_2 (atm) for different configurations at $\phi = 0^o$

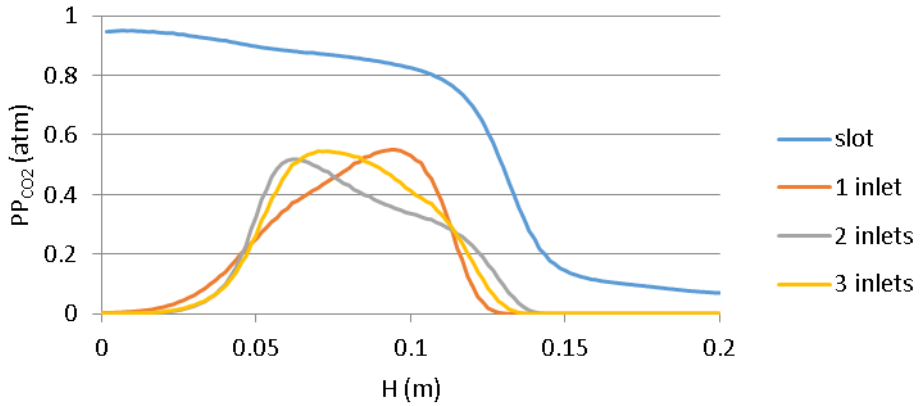

Figure 6.4c: Partial pressure of CO_2 (atm) for different configurations at $\phi = 315^o$

For the slot configuration, the CO_2 concentration decreases slightly from the bottom towards the top and drops rapidly at around z=0.14 m height. However, for other configurations, the CO_2 concentration is only between the ranges 0.05 m to 0.15 m. For two and three outlets system, the highest outlet at z=0.155 m and at z=0.165 m have zero concentration of CO_2, indicating that CO_2 doesn't pass through these outlets. Thus, at ϕ=315º, CO_2 concentration is highly skewed for discrete outlets configurations. Almost 50% of the ceria is unexposed to CO_2 which leads to poor oxidation reaction extent. Thus, among the different systems, slot configuration seems to be the most appropriate for the CO_2 outlets. The absolute values of CO_2 concentration is also higher for slot configuration compared to others. This indicates that the flow rate of CO_2 exiting through the slot outlet is higher compared to other configurations outlets.

The crossover values for different inlet/outlet configurations is given in table 6.2 for each species. The main observation to note is that there is very high crossover of CO_2 for the discrete port inlet/outlet configuration. The CO_2 crossover values alone would

discourage the use of multiple inlet/outlet configuration. The net reduction in fuel output due to combined O_2 and CO crossovers is the least for the slot configuration and is 5%.

Case	**N_2**	**O_2**	**CO_2**	**CO**
Slot	10%	5%	28%	-
1 inlet/outlet	17%	9%	66%	10%
2 inlets/outlets	22%	6%	77%	11%
3 inlets/outlets	20%	3%	76%	6%

Table 6.2: Crossover values for different inlet/outlet configurations

6.4 Conclusions

The variation of different species' concentration along the height of the reactor is studied for different configurations. In the reduction side, inlet and outlet configuration has negligible influence on the N_2, O_2 concentration. However, on the oxidation side, there are significant differences for various configurations. At the oxidizer inlet, slot configuration seems to underperform compared to other configurations. In contrast, at the oxidizer outlet, slot configuration leads to the most uniform oxidizer concentration among all other types of configurations. Based on the crossover values, slot configuration seems to be the most preferred system for the gas inlet/outlet geometry of the reactor.

7.0 Summary and Outlook

Crossover is a critical issue that needs to be addressed during fluid modeling of the reactor. Unswept O_2 released during reduction reaction when exposed to the reduced ceria, recombines with it, thus, reducing the maximum theoretical fuel output potential of the reactor. Thus, crossover adversely affects the overall efficiency of the reactor. Similarly, crossover of fuel results in lowering of fuel output.

Fluid dynamics modeling of the prototype reactor was carried out in FLUENT by developing different reactor models of varying complexity. These models were used to quantify the crossover of species and optimize the inlet/outlet gas channels design with respect to the crossover of the species, subject to other dimensions of the reactor and the inlet conditions. Parametric study of three identifiable geometric variables of the inlet/outlet geometry namely, angular position, circumferential position, width of the inlets/outlets were carried out. The fluid flow direction in the pre-heating gap changes with changes in geometric parameters. The flow direction in the pre-cooling gap is always from reduction to oxidation side for all conditions considered. The flow into the aperture is negligible. The crossover of species reduces the overall efficiency by 2% to 6% for the optimized reactor model depending on the inlet flow rate conditions.

Fluid flow within the reactor model was observed for different morphology of the reactive material (ceria) mainly characterized by different orders of permeability. There is very little flow through the low permeable ($K \sim 10^{-12}$ m^2) monolith ceria (0.07% of the fluid gap). Higher orders of permeability ($K \sim 10^{-6}$ m^2) results in considerable flow (38% of the fluid gap) and thus, increase crossover of the species. However, for the

permeability range 10^{-12} to 10^{-8} m^2, there is negligible differences in flow field. Higher permeability also provides lesser resistance to the sweeping action of the inert gas and thus, mean O_2 partial pressure in the reduction zone gets lower.

The influence of the rotation of the ceria ring and the recuperator is studied by varying the rotation speed of the ceria ring. It was found that rotation speed up to 1 rpm did not result in any significant changes in either flow field or the crossover values.

Typical flow rates of the sweep gas and the oxidizer were simulated to test their effects on the flow field within the reactor. The amount of sweep gas affects the flow field in the oxidation zone, while the reduction zone is completely isolated from the oxidizer and the fuel. Use of 170:1 ratio of N_2 to O_2 release is found to lead to lower O_2 partial pressure in the reduction zone, compared to 100:1. However, the extra heating required for higher mass flow rate of sweep gas largely outweighs the small increase in fuel output. Thus, 100:1 N_2 to O_2 release is recommended. The type of oxidizer affects the distribution of it within the oxidation zone. CO_2 and H_2O, heavier and lighter than N_2, tend to settle at the bottom and top of the reactor, respectively. N_2 crossing over the top of the reactor, coupled with CO_2 settling towards the bottom of the reactor, leads to relatively low concentration of the oxidizer in the top quarter of the reactor for 5x case. This potentially could hinder the oxidation reaction. One way to overcome this challenge is to send higher mass flow rates of CO_2

Lastly, equidistant discrete holes (1, 2, 3) were considered for inlets/outlets instead of slot configuration. On the reduction side, the distribution of the sweep gas was uniform for all configurations. On the oxidation side, slot configuration seems to perform

worse compared to others near the oxidizer inlet in terms of uniform distribution of oxidizer concentration along the height of the reactor. The presence of discrete inlets leads to better distribution for CO_2. However, at the oxidizer outlet, the oxidizer distribution is skewed around the outlets near the bottom of the reactor. Presence of discrete holes causes heavy crossover of the oxidizer via the pre-heating gap and exiting through N_2 outlet. Thus, there is very low concentration of the oxidizer present near the oxidizer outlet. Taking into account the high crossover of the oxidizer, the slot configuration is the most suitable for the gas channel inlets/outlets system.

2D reactor model with ceria ring provides a good estimate of the crossover values of the species and is useful in designing of the gas channels. However, 3D reactor model provides a better estimate of the crossover values and the species' distribution along the axial direction. All the models in the current study included uniform release of O_2 and the fuel based on a specific non-stoichiometry value of ceria, which is unlikely considering the highly non-linear nature of non-stoichiometry.

For a more rigorous and microscopic approach, chemical modeling of the reduction and oxidation reactions of the ceria is necessary. The assumption of fast kinetics and using thermal equilibrium chemistry data of ceria would be a good start in this direction. This would provide a better guess on the non-stoichiometry and the amount of O_2 and fuel release.

References

[1] J. E. Funk, R.M. Reinstrom, “Energy requirements in production of hydrogen from water”, *Ind. Eng. Chem. Process Des. Dev.,* Vol. 5, No. 3, pp 336-342, 1966

[2] L. D’Alessio, M. Paolucci, “Energetic aspects of the syngas production by solar energy: reforming of methane and carbon gasification”, *Solar & Wind Technology,* Vol. 6, No. 2, pp. 101-104, 1989

[3] A. Steinfeld and R. Palumbo, "Solar Thermochemical Process Technology," in *Encyclopedia of Physical Science and Technology*, vol. 15, R. A. Meyers, Ed., Burlington, Academic Press, 2001, p. 237–256.

[4] T. Kodama, "High-Temperature Solar Chemistry for Converting Solar Heat to Chemical Fuels," *Progress in Energy and Combustion Science,* vol. 29, p. 567–597, 2003.

[5] E. A. Fletcher, "Solarthermal Processing: A Review," *Journal of Solar Energy Engineering,* vol. 123, p. 63–74, 2001.

[6] A. Steinfeld, "Solar Thermochemical Production of Hydrogen – A Review," *Solar Energy,* vol. 78, p. 603–615, 2005.

[7] E. A. Fletcher and R. L. Moen, "Hydrogen and Oxygen from Water," *Science,* vol. 197, p. 1050–1056, 1977.

[8] T. Nakamura, "Hydrogen Production from Water Utilizing Solar Heat at High Temperatures," *Solar Energy,* vol. 19, p. 467–475, 1977.

[9] T. Kodama and N. Gokon, "Thermochemical Cycles for High-Temperature Solar

Hydrogen Production," *Chemical Reviews,* vol. 107, p. 4048–4077, 2007.

[10] G. J. Kolb and R. B. Diver, "Screening Analysis of Solar Thermochemical Hydrogen Concepts," Sandia National Laboratories, New Mexico, 2008.

[11] S. Abanades and G. Flamant, "Thermochemical Hydrogen Production From a Two-Step Solar-Driven Water-Splitting Cycle Based on Cerium Oxides," *Solar Energy,* vol. 80, p. 1611–1623, 2006.

[12] W. Lipinski, J. H. Davidson, T.R. Chase, "Thermochemical Reactor Systems and Methods", International Patent Application PCT/US12/66301, November, 2012.

[13] J. H. Davidson, W. Lipiński, A. Stein and T. Chase, "Solar Recycling of CO_2 to Fuels," IREE Award No. RL-0002-2011, 2011.

[14] P. Furler, J. R. Scheffe, A. Steinfeld, "Syngas Production by Simultaneous Splitting of H_2O and CO_2 via Ceria Redox Reactions in a High-Temperature Solar Reactor," *Energy & Enviornmental Science,* vol. 5, p. 6098–6103, 2012.

[15] J. L. Lapp, J. H. Davidson and W. Lipiński, "Efficiency of Two-Step Solar Thermochemical Non-Stoichiometric Redox Cycles with Heat Recovery," *Energy,* vol. 37, p. 591–600, 2012.

[16] J. L. Lapp, J. H. Davidson and W. Lipiński, "Heat Transfer Analysis of a Solid-Solid Heat Recuperation System for Solar-Driven Non-Stoichiometric Redox Cycles," *Journal of Solar Energy Engineering,* vol. 135, p. 031004, 2013.

[17] J. L. Lapp and W. Lipiński, "Three Dimensional Heat Transfer Modeling of a Solar Thermochemical Reactor for Water and CO_2 Splitting with Ceria," *Proc. of the 7th International Conference on Energy Sustainability,* Minneapolis, 2013

[18] J. L. Lapp, “Thermal modeling and design of a solar Non-stoichiometric redox reactor with Heat recovery,” *PhD thesis,* University of Minnesota, 2013.

[19] R. J. Panlener, R. N. Blumenthal, J. E. Garnier, W. Chueh, “A thermodynamic study of nonstoichiometric cerium dioxide”, *Journal of Physics and Chemistry of Solids,* Vol. 36, pp. 1213-1222, 1975

[20] S. Haussener, A. Steinfeld, “Effective heat and mass transport properties of anisotropic porous ceria for solar thermochemical fuel generation”, *Materials,* Vol. 5, pp. 192-209, 2012

[21] Cussler E.L., Diffusion, Cambridge University Press, 1997.

[22] McGee H.A., *Molecular Engineering,* McGraw-Hill, New York, 1991

[23] Kuo K.K.Y., *Principles of Combustion,* John Wiley & Sons, New York, 1986

[24] M. Kaviany, Principles of Heat Transfer in Porous Media, New York: Springer, 1999

[25] Yaws C., *Transport Properties of Chemicals and Hydrocarbons: Viscosity, Thermal Conductivity, and Diffusivity of C1 to C100 organics and Ac to Zr inorganics,* Elsevier, 2009

[26] Rose J.W., Cooper J.R., *Technical Data on Fuel,* Scottish Academic Press, Edinburgh, 1977

[27] Hirschfelder J.O., Curtiss C.F., Bird R.B., *Molecular Theory of Gases and Liquids,* John Wiley & Sons, New York, 1954

[28] J. Petrasch, F. Meier, H. Friess, A. Steinfeld, “Tomography based determination of permeability, Dupuit-Forchcheimer coefficient, and interfacial heat transfer

coefficient in reticulate porous ceramics", *International Journal of Heat and Fluid Flow,* Vol. 29, pp. 315-326, 2008

[29] Z. Zeng, R. Grigg, "A Criterion for Non-Darcy Flow in Porous Media", *Transport in Porous Media,* Vol. 63, pp. 57-69, 2006

[30] W. Chueh, *et. al,* "High-Flux solar-driven thermochemical dissociation of CO_2 and H_2O using nonstoichiometric ceria", *Science,* Vol. 330, pp. 1797-1801, 2010

[31] D. Chapman, K. A. Browning, "Radar observations of wind-shear splitting within evolving atmospheric Kelvin-Helmholtz billows", *Quart. J. Roy. Meteor. Soc.,* Vol. 123, pp. 1433-1439, 1997

Appendix A: Mesh independence study

2D reactor model is meshed with two different settings of mesh and the u-velocity at the pre-cooling gap and the O_2 partial pressure along the surface of the ceria ring in the reduction zone are plotted. Mesh refinement is done based on the average values of aspect ratio and the skewness. Refining the mesh increased the number of cells by about 10%.

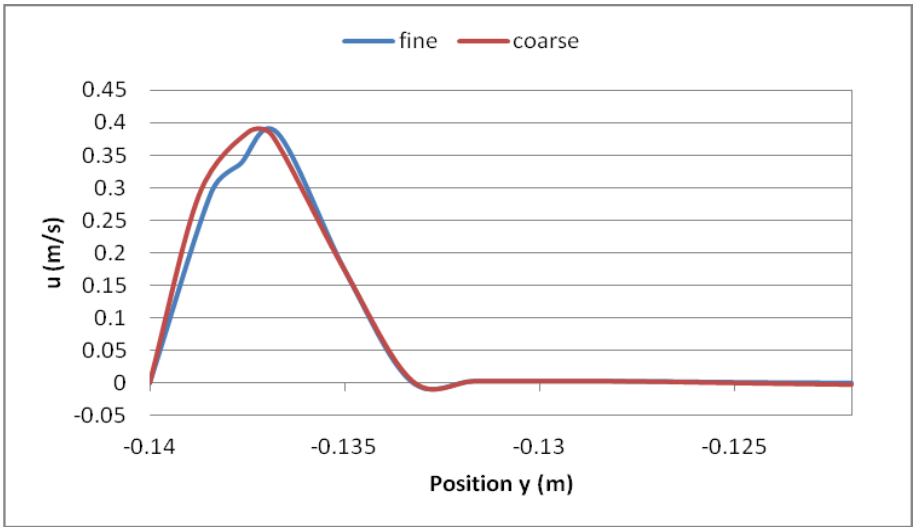

Figure A.1: u-velocity along position y (m) for two different meshes

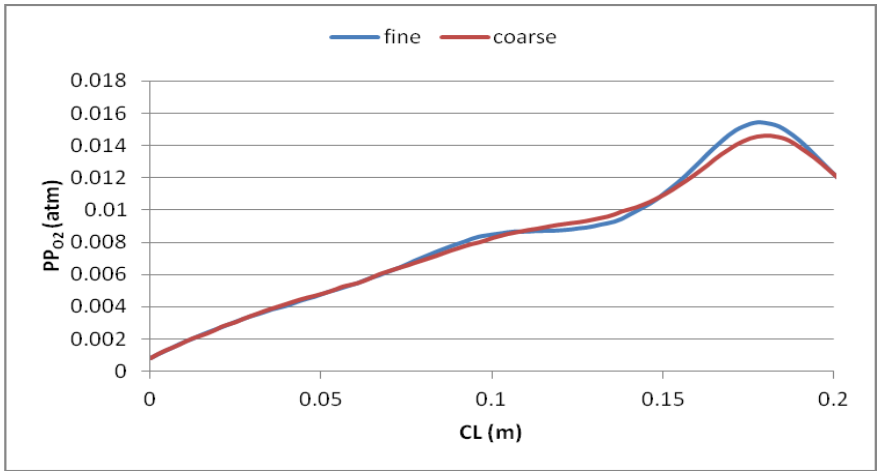

Figure A.2: O_2 partial pressure along curve length for two different meshes

The mass imbalance for both cases are less than 0.1%. The coarser of the mesh is used for all the simulations in this study.

Similar study is done for the 3D mesh. The distribution of aspect ratio and the skewness for the 3D mesh is given below.

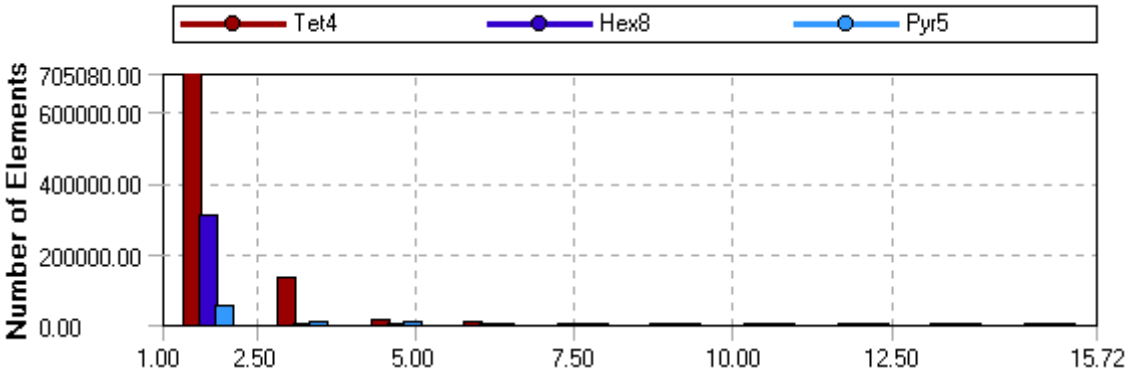

Figure A.3: Aspect ratio distribution for 3D mesh

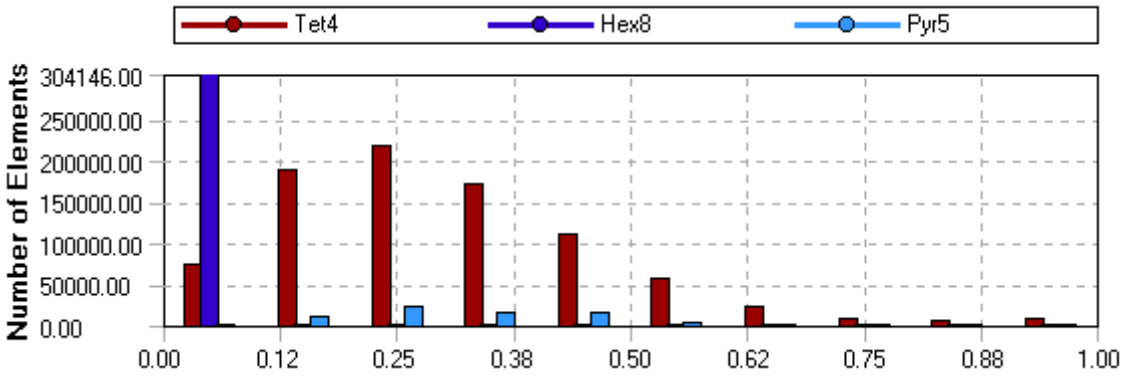

Figure A.4: Skewness ratio distribution for 3D mesh

Appendix B: Temperature dependent properties

Dynamic viscosity (kg/m-s)

In the current model, piecewise-polynomial has been used to define dynamic viscosity as a function of temperature. For N_2, viscosity data are available for temperatures up to 1970 K. For all other species, the polynomial is valid till 1500 K. At higher temperatures, the value of 1500 K is taken.

$\mu(T) = A + BT + CT^2 + DT^3$ ($\mu \times 10^7$ in *kg/m-s,* T in *K*) [25]

Species	A	B	C	D
CO	18.0493	6.3753E-01	-3.5748E-04	1.0287E-07
CO_2	11.8109	4.9838E-01	-1.0851E-04	0.0000E+00
N_2	4.4656	6.3814E-01	-2.6596E-04	5.4113E-08
O_2	-4.9433	8.0673E-01	-4.0416E-04	1.0111E-07

Table B.1: Coefficients of dynamic viscosity co-relation with temperature

Thermal conductivity (W/m-K)

Similar to dynamic viscosity, the thermal conductivity of all the species has been defined as piecewise-polynomial of third order. Thermal conductivity coefficients of O_2 are valid till 2000 K. For all other species, the temperature upper range for the validity of the polynomial is 1500 K. At higher temperatures, the value of 1500 K is taken.

$k(T) = A + BT + CT^2 + DT^3$ (*k* in *W/m-K,* T in *K*) [26]

Species	A	B	C	D
CO	9.9186E-04	9.4020E-05	-4.0761E-08	1.3751E-11
CO_2	-6.0783E-03	7.5351E-05	9.4928E-09	-1.1275E-11
N_2	-2.2678E-04	1.0275E-04	-6.0151E-08	2.2332E-11
O_2	1.5475E-04	9.4153E-05	-2.7529E-08	5.2069E-12

Table B.2: Coefficients of thermal conductivity co-relation with temperature

Heat capacity (J/kg-K)

The heat capacity for each individual species is defined as piecewise-polynomial of fourth order. The piecewise-polynomial has been defined in two ranges of temperature: 300K– 1000K and 1000K – 5000K. The coefficients are obtained from in-built FLUENT database.

$c_p(T) = A + BT + CT^2 + DT^3 + ET^4$ (c_p in *J/kg-K,* T in *K*) [26]

Species	A	B	C	D	E	Range (K)
CO	968.3898	4.4879E-01	-1.1522E-03	1.6569E-06	-7.3464E-10	300 - 1000
	897.9305	4.2823E-01	-1.6714E-04	3.0234E-08	-2.0514E-12	1000 - 5000
CO_2	429.9289	1.8745E00	-1.9665E-03	1.2972E-06	-4.0000E-10	300 - 1000
	841.3765	5.9324E-01	-2.4152E-04	4.5227E-08	-3.1531E-12	1000 - 5000
N_2	979.043	4.1796E-01	-1.1763E-03	1.6744E-06	-7.2563E-10	300 - 1000
	868.6229	4.4163E-01	-1.6872E-04	2.9968E-08	-2.0044E-12	1000 - 5000
O_2	834.8265	2.9296E-01	-1.4956E-04	3.4139E-07	-2.2784E-10	300 - 1000
	960.7523	1.5941E-01	-3.2709E-05	4.6128E-09	-2.9528E-13	1000 - 5000

Table B.3: Coefficients of heat capacity co-relation with temperature for different species

Appendix C: Mixture Properties

Mixture properties of the species mixture is calculated from the properties of the individual species.

Density

The composition-dependent density for a mixture is necessary to solve species transport equations. In the model, the density for a mixture is chosen using the ideal gas law for an incompressible flow,

$$\rho = \frac{p}{RT\sum_i \frac{Y_i}{M_{w,i}}}$$

where, p is the absolute pressure (Pa) and M_i is the molecular weight of the species i (kg/mol), R is the universal gas constant (J/mol-K).

The other mixture properties like dynamic viscosity, thermal conductivity, heat capacity are calculated as mass fraction weighted average of the individual properties as follows.

$$\mu_f = \sum_i Y_i \mu_i$$

$$k_f = \sum_i Y_i k_i$$

$$c_{p,f} = \sum_i Y_i c_{p,i}$$

where, Y_i is the mass fraction of species i.

Appendix D: Calculation of non-stoichiometry

The non-stoichiometry is a function of temperature and O_2 partial pressure.

At chemical equilibrium, the following relation holds,

$$\Delta\overline{H}_{O_2}(\delta) - T * \Delta\overline{S}_{O_2}(\delta) = R * T * \ln\left(\frac{p_{O_2}}{p_{ref}}\right)$$

where, p_{ref} is the reference pressure $p_{ref} \cong 1\ atm$

The data for standard enthalpy and entropy as a function of non-stoichiometry is given in Panlener [19].

The curve fits for $\Delta\overline{H}_{O_2}$, $\Delta\overline{S}_{O_2}$ in SI units are given below.

$$\Delta\overline{H}_{O2} = ch_1(\log_{10}\delta)^2 + ch_2(\log_{10}\delta) + ch_3 \ [\text{J/mol - O}_2] \qquad (0.001 < \delta < 0.0427)$$

$$\Delta\overline{H}_{O2} = CH_1(\delta)^6 + CH_2(\delta)^5 + CH_3(\delta)^4 + CH_4(\delta)^3 + CH_5(\delta)^2 + CH_6(\delta) + CH_7$$

$$(0.006 < \delta < 0.26)$$

$$\Delta\overline{S}_{O2} = cs_1(\log_{10}\delta)^2 + cs_2(\log_{10}\delta) + cs_3 \ [\text{J/mol - O}_2 - \text{K}] \qquad (0.001 < \delta < 0.027)$$

$$\Delta\overline{S}_{O2} = CS_1(\delta)^6 + CS_2(\delta)^5 + CS_3(\delta)^4 + CS_4(\delta)^3 + CS_5(\delta)^2 + CS_6(\delta) + CS_7$$

$$(0.005 < \delta < 0.26)$$

The coefficients are given in table D.1.

ch_1	4.36343	cs_1	1.64180E+01
ch_2	2.52757E+01	cs_2	2.01125E+02
ch_3	-6.05169E+01	cs_3	-1.70707E+02

Table D.1 : Coefficients of the standard enthalpy and entropy for lower non-stoichiometry range

CH_1	-1.85603E+10	CS_1	-2.00056E+07
CH_2	1.53556E+10	CS_2	1.78760E+07
CH_3	-4.71416E+09	CS_3	-6.27177E+06
CH_4	6.77803E+08	CS_4	1.10624E+06
CH_5	-5.54153E+07	CS_5	-1.08180E+05
CH_6	3.88120E+06	CS_6	6.77051E+03
CH_7	-9.72395E+05	CS_7	-5.67226E+02

Table D.2 : Coefficients of the standard enthalpy and entropy for higher non-stoichiometry range

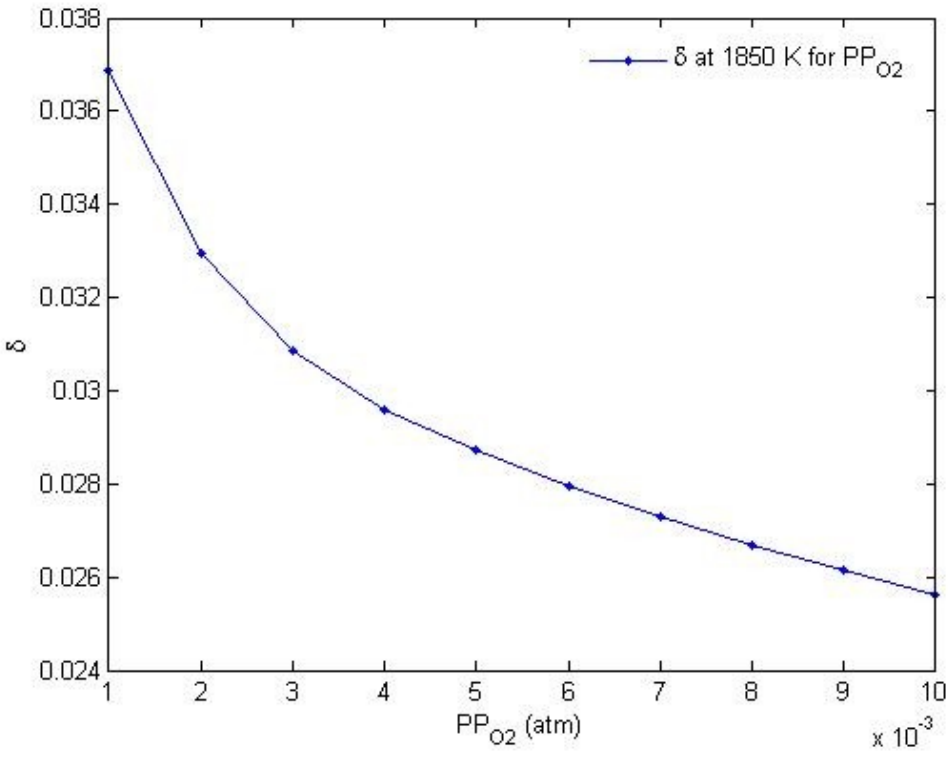

Figure D.1: Variation of non-stoichiometry with O_2 partial pressure at 1850 K